



# ESM TODAY 2014

*11<sup>th</sup> Graduate Research Symposium*

Engineering Science and Mechanics

Abstract Book

## **Keynote Speaker**

Dr. Stephen J. Fonash, Bayard D. Kunkle Professor, Engineering Science and Mechanics

## **Total list of Participants ( posters and presentations)**

Aaron Lesky	Maryam Neshastehriz
Abdon Pena Francesh	Mathew Joseph Pyrz
Adem Ozcelik	Mehdi Hasan
Ahmad Ahsan	Mengqian Lu
Anuriddh Vashisth	Navendu Patil
Cooper Elsworth	Nitesh Nama
Feng Guo	Po-Hsun Huang
Hui Yang	Stephen Swiontek
Huihun Jung	Yao Zhang
Huilong Hui	

## **List of Judges**

Dr. Suliman Samia	Dr. Judith Todd
Dr. Akhlesh Lakhtakia	Dr. Koray Sekeroglu
Dr. Clifford Lissenden	Dr. Michael Lanagan
Dr. Corina Drapaca	Dr. Reginald Hamilton
Dr. Ivica Smid	Dr. Scott Miller
Dr. Jonathan Pitt	

# PRESENTATIONS

# WAVE ENERGY AS A DAMAGE SENSITIVE FEATURE

A. Lesky<sup>1</sup> and C.J. Lissenden<sup>2</sup>

<sup>1</sup>Graduate Program In Acoustics

<sup>2</sup>Engineering Science & Mechanics Dept.  
Penn State, University Park, PA, 16803

Structural health monitoring (SHM) commonly employs ultrasonic guided waves for detecting and locating defects in various structures. Guided waves provide utility in SHM applications because they can be used to inspect structures nondestructively. Therefore, guided waves can be used over and over again to inspect structures repeatedly and to track the progression of damage. Lamb waves, the focus of this research, are a family of ultrasonic guided waves that exist in plates and shell structures and are governed by the Rayleigh-Lamb dispersion relations [1], see eq. (1).

$$\frac{\tan(\beta b)}{\tan(\alpha b)} + \left( \frac{4\alpha\beta\xi^2}{(\xi^2 - \beta^2)^2} \right)^{\pm 1} = 0 \quad (1)$$

$$\alpha^2 = \frac{\omega^2}{c_1^2} - \xi^2 \quad (2)$$

$$\beta^2 = \frac{\omega^2}{c_2^2} - \xi^2 \quad (3)$$

where  $c_1$  is the dilatational wave speed,  $c_2$  is the shear wave speed,  $\omega$  is frequency (rad/s), and  $\xi$  is the wave number, and  $b$  is half the plate thickness. Solving eq. (1) for real wave numbers at all desired frequencies yields the propagating Lamb waves in the plate. Each propagating Lamb wave has a different displacement profile. One can use the dispersion curve to select a propagating Lamb wave mode and compute the displacement profile. Mode selection is important when considering if a particular mode will be sensitive to a certain kind of material defect. The displacement profiles for each propagating frequency/wavenumber are given by eqs. (4) and (5) referenced to a Cartesian coordinate system on a plate given in Fig 1, which is adapted from Graff [1].

$$u_x = i\{\xi(A \sin(\alpha y) + B \cos(\alpha y)) \dots + \beta(C \cos(\beta y) - D \sin(\beta y))\}e^{i(\xi x - \omega t)} \quad (4)$$

$$u_y = \{\alpha(A \cos(\alpha y) - B \sin(\alpha y)) \dots + \xi(C \sin(\beta y) + D \cos(\beta y))\}e^{i(\xi x - \omega t)} \quad (5)$$

It should be noted that the  $i$  in eq. (4) is interpreted as a phase shift between the two coordinate directions. The constants A, B, C, and D are to be determined from

boundary conditions, if known, or are arbitrary for the sake of plotting. Also  $u_x$  is commonly called the in-plane displacement and  $u_y$  is the out-of-plane displacement.

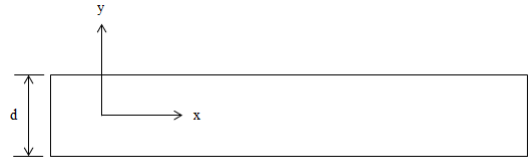


Figure 1. Coordinate system which  $u_x$  and  $u_y$  are defined. Note  $d = 2b$ .

Pressure vessels are commonly used in industries where failures can have large economic, health, and/or environmental effects. Particularly as industry infrastructure ages, monitoring the health of pressure vessels and large diameter pipes is imperative. Structures like this pose certain challenges for guided wave SHM. For example, inspection must be done while the structure is in use. This means that both sides of the pipe/vessel will be in contact with a fluid. Depending on the fluid, this could be catastrophic for guided wave propagation. The vessel could also experience different operating conditions during service, which could impact the guided waves. Material properties are typically functions of temperature and satisfaction of eq. (1) implicitly depends on material properties. Lastly, pressure vessels and pipes are typically round. This makes mounting conventional ultrasonic transducers difficult. To overcome these issues, flexible strip transducers [2] were designed that can be bonded to curved vessels/pipes and a proper mode selected. The strip transducers actuate plane waves within the structure. Plane waves are advantageous because the amplitude is a weak function of space in comparison to the common PZT disk transducer whose amplitude is a strong function of space. The defect in this study is an artificial surface-breaking fatigue crack. To detect a surface crack, a wave displacement profile that has maximum in-plane displacement near the plate surfaces was selected. Such a mode exists when excited in a plate with a phase

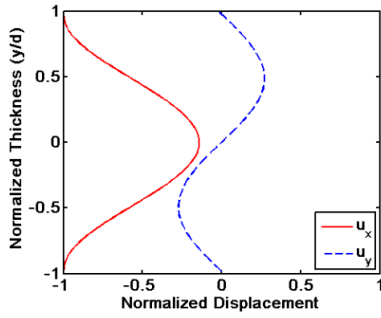


Figure 2. S1 mode displacement profile

velocity equal to the dilatational wave velocity,  $c_1$  [3]. Maximizing  $u_x$  while minimizing  $u_y$  on the plate surface will give good sensitivity to a surface crack while minimizing fluid-induced damping. This mode is known as the S1 mode and Fig 2 shows its displacement profile.

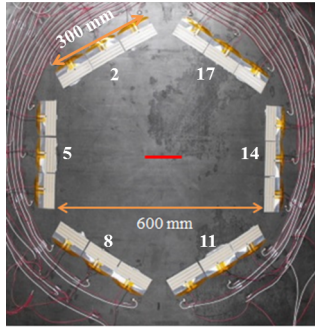


Figure 3. Transducer array mounted on structure. Red line indicates defect orientation and location.

A prototype pressure vessel was built to test if Lamb waves activated by the strip transducers were sensitive to surface breaking fatigue cracks. The structure was made of a 6.35 mm thick, A36 steel plate curved to a 1 m radius. The transducers were arranged in a hexagonal array of width 600 mm with three transducers per side, see Fig 3, on the convex side of the plate. Doing so allowed a plane wave 300 mm wide to be activated in the plate while the signal could be received by the remaining transducers individually to improve sensitivity to the local displacement field. This was done for both baseline and damage configurations and for four different environmental conditions: Dry (dry plate at approx. 20°C), Wet (plate filled with water at approx 20°C), Dry Hot (dry plate at approx. 37°C), and Wet Hot (plate filled with water at approx. 37°C). The baseline condition was the healthy, undamaged plate while the damage condition was the plate with a  $\frac{1}{4}$  thickness depth notch defect. Two different length notches were used (13 mm and 19 mm) to simulate a growing crack. The goal of testing

over four different conditions was to evaluate if the chosen S1 mode was impervious to the fluid loading and that it could be excited over a range of ambient temperatures.

The received data were analyzed in the frequency domain by evaluating the energy in the wave signal. The wave energy was expected to decrease for paths across the array when a defect was present while wave energy was expected to increase in the received reflections induced by the defect. The signal energy was normalized by the energy in the baseline signal for each respective transducer pair.

$$\text{Normalized Energy} = \frac{\int_b^a |X(f)|^2 df \{D\}}{\int_b^a |X(f)|^2 df \{B\}} \quad (6)$$

Where the limits of integration are  $a = 599.06$  kHz and  $b = 600.78$  kHz. The quantity  $|X(f)|^2$  is the energy spectral density of the received time domain signal and D and B refer to damage and baseline signals, respectively. The transmission path energy results decrease with increasing notch length while the received reflection results appear to be buried in the data acquisition system noise floor. Typical results for strip transmission paths are shown in Fig 4, where the legend corresponds to transmitter-receiver numbers shown in Fig 3.

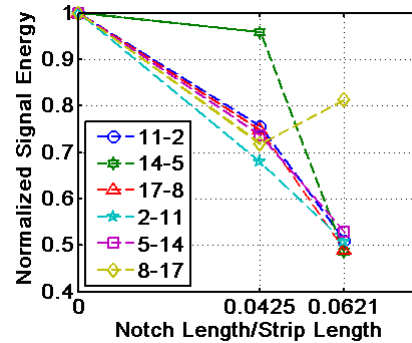


Figure 4. Wave energy decreasing as defect length increases.

## References

- [1] Graff, K., *Wave Motion in Elastic Solids*. Mineola, NY: Dover Publications, 1991.
- [2] S. Li and C. J. Lissenden, "Piezoelectric Fiber Composite Strip Transducer Design Considerations for Generating Lamb Waves," *J. Intell. Mat. Sys. Struct.* 22, 1345-1357 (2011).
- [3] A. Pilarski, J. J. Ditri, J. L. Rose, *J. Acoust. Soc. Am.* 93(4), Pt. 1 (1993).

# AN ACOUSTOFLUIDIC MICROMIXER BASED ON STEADY AND UNSTEADY BUBBLE CAVITATION

*A. Ozcelik, D. Ahmed, N. Nama, A. A. Nawaz, and T. J. Huang*

Engineering Science and Mechanics Department, Penn State, PA-16802, USA

Fast and effective mixing of liquids in microfluidic systems is an important task for numerous applications including chemical synthesis[1], biochemical reactions[2], and clinical diagnosis[3]. Microfluidic platforms offer many advantages for these applications such as small sample/reagent consumption, rapid and high-precision analysis, and low-cost devices. However, achieving effective mixing of viscous samples in microfluidics is challenging due to the extremely low Reynolds number[4].

In the literature, various microfluidic mixers have been developed including passive approaches, such as chaotic advection[5], as well as active approaches, such as hydrodynamic[6], and acoustic-based[7] mixing. Nonetheless, few of these methods have demonstrated the ability to mix high-viscosity fluids,[8], [9] and their performance is often less than optimum. Therefore, it is necessary to develop a new class of microfluidic mixers that can achieve effective, fast mixing with simple devices and experimental setups.

In this work, we present an acoustofluidic method that takes advantage of the wavy structures in polydimethylsiloxane (PDMS) microchannels made from silicon molds fabricated from the deep reactive ion etching (DRIE) process.

Figure 1. demonstrates the operating mechanism of the acoustofluidic mixing device. The PDMS microchannel is made from a silicon mold that is patterned by photoresist followed by DRIE. As a result of the DRIE process, the sidewall of the silicon mold develops wavy structures. These wavy structures of the silicon mold are subsequently transferred to the PDMS channel by the replica-molding process. The rough surface of the PDMS sidewalls develops voids when a liquid is injected into the PDMS channel. These voids form stabilized cavitation nuclei when an acoustic field is applied in the liquid.[10] Acoustic waves consist of compression and expansion cycles. During the expansion cycle, the diffusion boundary layer of the bubbles becomes thinner, and the surface area of the bubble gets larger. As a result, gas is transferred into the bubbles from the surrounding fluidic media. Depending on the flow rates and the viscosity of the fluid, we have observed both steady and unsteady cavitation in the devices. With low flow rates, bubbles frequently emerge and disappear from the channel sidewall, suggesting unsteady cavitation. During this process, bubbles grow in expansion cycles until they become unstable and eventually collapse in the next compression cycle. The left panel of Fig. 2a shows the modes of a single-bubble collapse near a boundary. As the bubble collapses, jetting and counter-

rotating vortices occur. These fast-rotating vortices break the laminar flow, enabling homogenous mixing instantaneously. At higher flow rates ( $\geq 30 \mu\text{L}/\text{min}$ ), steady cavitation is predominantly observed. Microstreaming phenomenon, which is the pressure and velocity fluctuations in the surrounding fluid medium, occurs (Fig. 2.c-d), and break laminar flow interface.

We used micro-channels with width, depth, and length of  $240 \mu\text{m}$ ,  $155 \mu\text{m}$ , and  $1.2 \text{ cm}$ , respectively. Mixing performance was tested using water and fluorescein dye for low viscosity experiments and PEG solutions for high viscosity experiments. In all of our experiments, the frequency and voltage applied to the acoustic transducer were fixed at  $38.9 \text{ kHz}$  and  $130 \text{ V}$  (peak to peak), respectively. Mixing efficiency (M) was calculated according to the reference [9].

Figure 3a. shows laminar flow of water and fluorescein dye. When the transducer was turned on, bubbles were initiated from the sidewalls and instantly mix the two fluids (fig. 3b). Homogenous mixing was visualized using intensity profile along the vertical line. Figure 3c. shows that when liquids were not mixed fluorescence intensity was around 160 arbitrary units (a.u.), and when mixing took place, it reduces to about 80 a.u. indicating homogenous mixing.

The capability of the technique was further studied using high viscosity PEG solutions ( $18.3 - 95.9 \text{ mPa.s}$ ). In these experiments, one of the inlets was injected with  $34.2 \text{ mPa.s}$  for all the experiments. The second inlet was injected with various different viscosities. Figure 4. shows the results of mixing efficiencies and optical images for selected viscosities. For  $77.3 \text{ mPa.s}$  PEG solution flowing from inlet 2 and  $34.2 \text{ mPa.s}$  flowing from inlet one, mixing efficiency was determined as 0.92 which indicated excellent mixing. The resulted mixture had a viscosity of  $48.8 \text{ mPa.s}$  which is 54.9 times higher than the viscosity of water ( $0.89 \text{ mPa.s}$ ). The Reynolds number (Re) for the mixed fluids was calculated to be  $1.14 \times 10^{-2}$ .

In summary, we demonstrated, for the first time, an acoustic mixer based on acoustic bubble cavitations in microfluidic channels. Acoustofluidic mixer was tested with high viscosity PEG solutions, and successfully mixed  $48.8 \text{ mPa.s}$  overall viscosity PEG solutions in less than 100 msec. Our mixer has a very simple design which is easy to fabricate and operate. It is applicable to many lab-on-a-chip applications including nanoparticle synthesis, microscopic sonochemical reactions, and biochemical reactors.

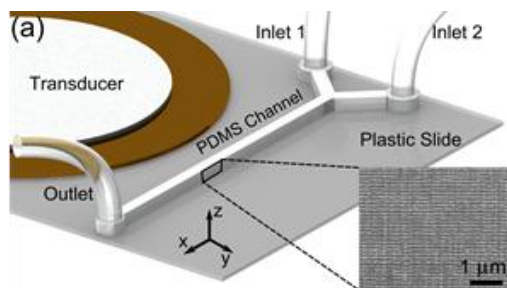


**Fig. 1** (a) Diagram of the microfluidic channel with the SEM image of the silicon master mold. The wavy structures are transferred onto the PDMS channel sidewall.

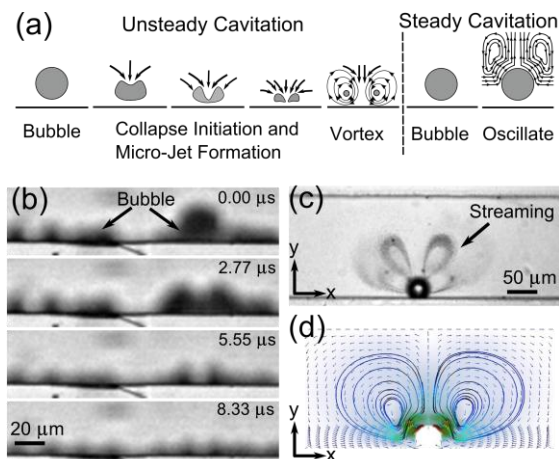


**Fig. 2** (a) Unsteady and Steady cavitation (b) Optical images of a bubble's unsteady cavitation. (c) Optical images of a bubble's steady cavitation (d) Simulated streamlines from theory.

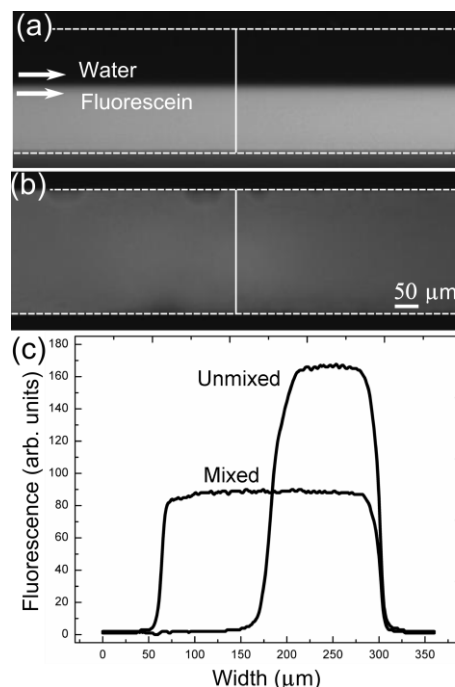


**Fig. 3** (a) Laminar flow of DI water and fluorescein dye in the absence of acoustic waves. (b) Homogenized mixing in the presence of acoustic waves. (c) Fluorescence plot across the channel width (vertical lines in (a) and (b)) before and after mixing

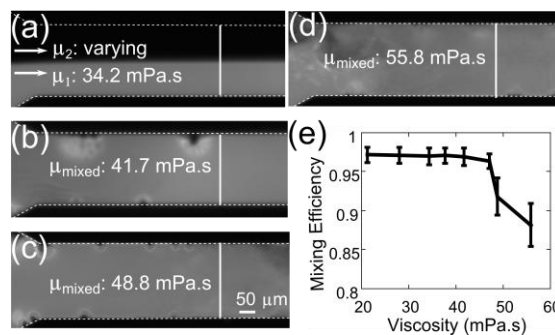


**Fig. 4** (a) Laminar flow of the unmixed PEG solutions where the inlet 1 was kept at a constant viscosity of 34.2 mPa.s. (b) Mixed solutions with  $\mu_{\text{mixed}}$ : 41.7 mPa.s, (c) 48.8 mPa.s, and (d) 55.8 mPa.s. (e) Plot of the mixing efficiency versus dynamic viscosity.

- [1] Y. Song, J. Hormes, and C. S. S. R. Kumar, "Microfluidic synthesis of nanomaterials.," *Small*, vol. 4, pp. 698–711, 2008.
- [2] L. Pollack, M. W. Tate, N. C. Darnton, J. B. Knight, S. M. Gruner, W. a Eaton, and R. H. Austin, "Compactness of the denatured state of a fast-folding protein measured by submillisecond small-angle x-ray scattering.," *Proc. Natl. Acad. Sci. U. S. A.*, vol. 96, pp. 10115–7, 1999.
- [3] L.-Y. Hung, Y.-H. Chuang, H.-T. Kuo, C.-H. Wang, K.-F. Hsu, C.-Y. Chou, and G.-B. Lee, "An integrated microfluidic platform for rapid tumor cell isolation, counting and molecular diagnosis.," *Biomed. Microdevices*, vol. 15, pp. 339–52, 2013.
- [4] X. Mao and T. J. Huang, "Microfluidic diagnostics for the developing world.," *Lab Chip*, vol. 12, pp. 1412–6, 2012.
- [5] F. Guo, M. I. Lapsley, A. A. Nawaz, Y. Zhao, S. S. Lin, Y. Chen, S. Yang, X. Zhao, and T. J. Huang, "A droplet-based, optofluidic device for high-throughput, quantitative bioanalysis.," *Anal. Chem.*, vol. 84, pp. 10745–9, 2012.
- [6] T. Thorsen, S. J. Maerkl, and S. R. Quake, "Microfluidic large-scale integration.," *Science*, vol. 298, pp. 580–4, 2002.

- [7] D. Ahmed, X. Mao, J. Shi, B. K. Juluri, and T. J. Huang, "A millisecond micromixer via single-bubble-based acoustic streaming.," *Lab Chip*, vol. 9, pp. 2738–41, 2009.
- [8] S. Wang, X. Huang, and C. Yang, "Mixing enhancement for high viscous fluids in a microfluidic chamber.," *Lab Chip*, vol. 11, pp. 2081–7, 2011.
- [9] Y. Li, Y. Xu, X. Feng, and B. Liu, "A rapid microfluidic mixer for high-viscosity fluids to track ultrafast early folding kinetics of G-quadruplex under molecular crowding conditions.," *Anal. Chem.*, vol. 84, pp. 9025–32, 2012.
- [10] H. B. Marschall, K. a Mørch, a P. Keller, and M. Kjeldsen, "Cavitation inception by almost spherical solid particles in water.," *Phys. Fluids*, vol. 15, p. 545, 2003.

# **SYNTHESIS OF ULTRA-SMOOTH TINI THIN FILMS BY BIASED TARGET ION BEAM DEPOSITION**

*Huilong Hou, Reginald F. Hamilton*

Department of Engineering Science and Mechanics,  
The Pennsylvania State University, University Park, PA 16802, United States

Ultra-smooth TiNi thin films are synthesized by biased target ion beam deposition (BTIBD) system. BTIBD is a novel approach for shape memory alloy thin film synthesis compared to the more commonly used magnetron sputtering technique. In this work, BTIBD is employed to deposit electron transparent thin films with less than 300 nanometer thicknesses. Deposition parameters are controlled in order to study Ni-rich, equiatomic, and Ti-rich compositions. Surface island structures are predominant in transmission electron

microscopy images of magnetron sputtered films[1-3], but are indistinct for BTIBD; ultra-smoothness is confirmed by atomic force microscopy for each composition, as in figure 1. BTIBD films exhibit surface Z heights that are one order of magnitude smaller than those from traditional magnetron sputtering. Smooth thin films synthesized by BTIBD are essential to the development and implementation of small-scale SMAs; including emerging magnetic shape memory alloy thin films.

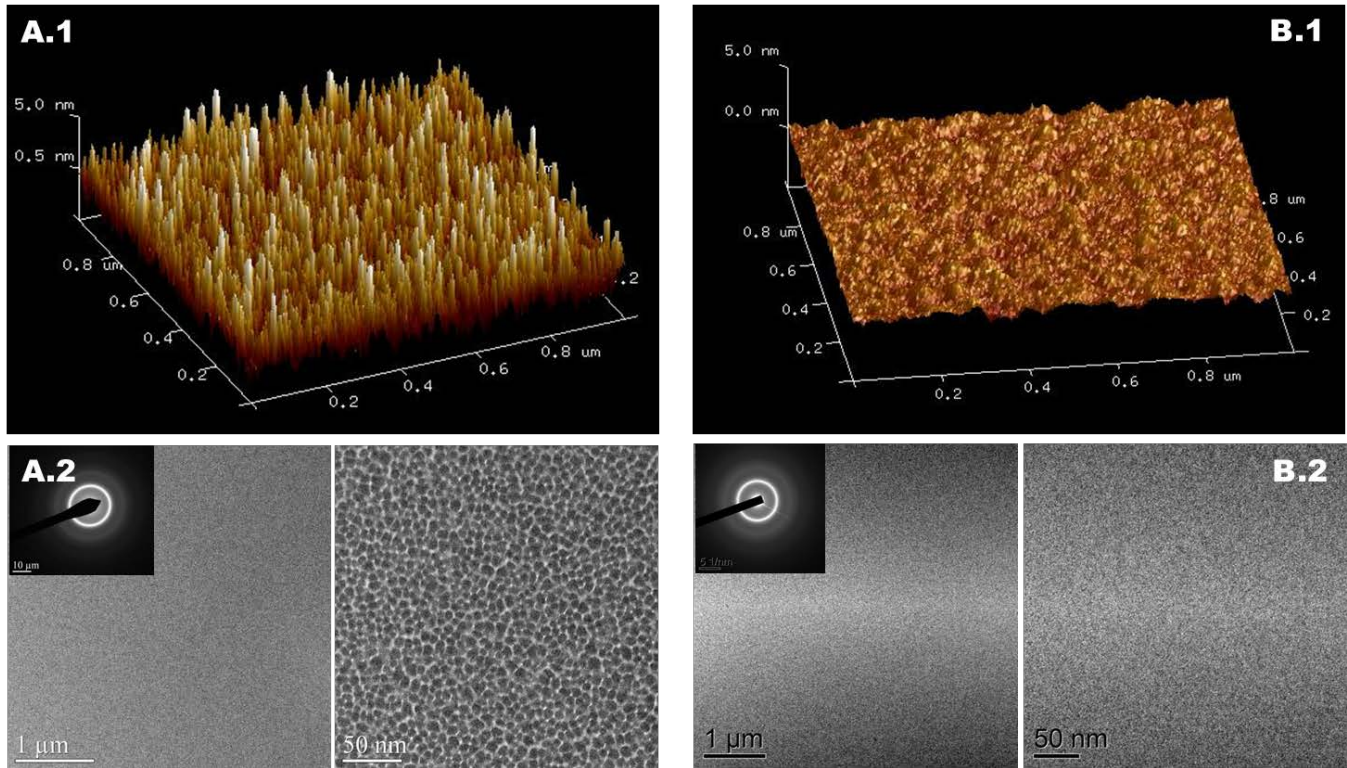


Figure 1: A.1) TiNi thin film from conventional Magnetron Sputtering has extensive island structure on the surface, verified by AFM; A.2) low mag TEM images shows the seemingly smooth and amorphous thin film while at high magnification projection island structure as white boundaries appears vastly.

B.1) TiNi Thin film from 4WAVE Ion Beam Assisted Biased-Target Deposition System is truly smooth on the surface, B.2) The smooth and amorphous feather are confirmed present at all scale, from low to high magnification.

## REFERENCES

- [1] Fu, Y., et al., *TiNi-based thin films in MEMS applications: a review*. Sensors and Actuators A: Physical, 2004. **112**(2-3): p. 395-408.
- [2] L. B. Freund and S. Suresh, *Thin Film Materials: Stress, Defect Formation and Surface Evolution*. 2003.
- [3] Nanda Kumar, A.K., et al., *Investigations on the mechanical behaviour of rough surfaces of TiNi thin films by nano indentation studies*. Surface and Coatings Technology, 2006. **201**(6): p. 3253-3259.

# SHAPE-CONTROLLABLE SYNTHESIS OF HYBRID STRUCTURES BY 3D HYDRODYNAMIC FOCUSING METHOD

*Mengqian Lu, Shikuan Yang, Ahmad Ahsan Nawaz, Tony Jun Huang*

Department of Engineering Science and Mechanics, The Pennsylvania State University  
Biofunctionalized NEMS Laboratory, the Huang Research Group, PA-16802, USA

Micro-/nano- structures (MNS) have shown potential applications in electronics, materials science and chemical, physical and biomedical fields.[1] In micro/nano scale, the size or shape change can affect the materials properties, such as optical, chemical, electrical properties.[2] Therefore, it is very important to fabricate MNS with uniform size and shape.

Conventional method, which simply mix reagents by vortex mixing, is difficult to control the size and shape distribution of the product. During reaction, the addition of reagents, rate of stirring, local temperature and concentration fluctuations can affect the forming process of the product. Conventional method cannot make good control of these parameters, ending up to broad size and shape distribution of products.[3]

In microfluidic systems, the mixing of reagent is caused by diffusion only, because of the laminar flow in the micro scale channels. Therefore, microfluidic hydrodynamic focusing (HF) system has been used to precisely control the convective-diffusive mixing of the reagents. In the absence of turbulence, co-flowing streams carrying the reagents form a very well defined interface. Reaction and assembly take place directly at the interface as well as in the diffusion cone of the reactants. Compared to the conventional “bulk mixing” methods, microfluidic device can achieve reproducible, well-controlled mechanical and chemical conditions, leading to superior quality of the formation of MNS.[4]

Two-dimensional (2D) HF provides horizontally uniform environment (flow rate, pressure, shear stress, *ect.*) in the reaction region, but variety parameters in the vertical dimension, which still limit the performance of 2D HF system in synthesis application. Additionally, in 2D HF system, the

reaction region contacts the top and bottom walls of the microfluidic channels. The aggregation of the product on the channel wall results in clogging of the channels, which substantially reduces the robustness and stability during synthesis process, and finally causes the failure of the device.[5]

Three-dimensional (3D) HF method can provide uniform environment both horizontally and vertically and confined the reagent streams at the center of the channel. Multi-step photolithography and assembly protocols have been developed for fabricating the 3D HF devices. However, these methods require either tedious assembly of individual components or multiple alignments and exposures during mold fabrication. These limitations inevitably increase the cost and complexity of the device and ultimately hinder their applicability. Our group has developed a simple single-layer planar microfluidic device based on a novel fluid manipulation technique named “microfluidic drifting”. [6] This method is effective, robust and does not require any extensive fabrication technique other than standard soft lithography.

In this paper, we synthesized TTF-Au hybrid structures with different shape and size by using the “micro drifting” based 3D HF devices. By tuning the flow conditions, different structures, such as wire, rod, particles, flower-shape, multi-layer and triangle can be achieved. The products fabricated by 3D HF showed narrower size distribution compared to the one fabricated by “bulk” mixing. It is also found that, in microfluidic channel, even though the ratio between reagents as constant, by changing the flow rate, different structures can be fabricated.

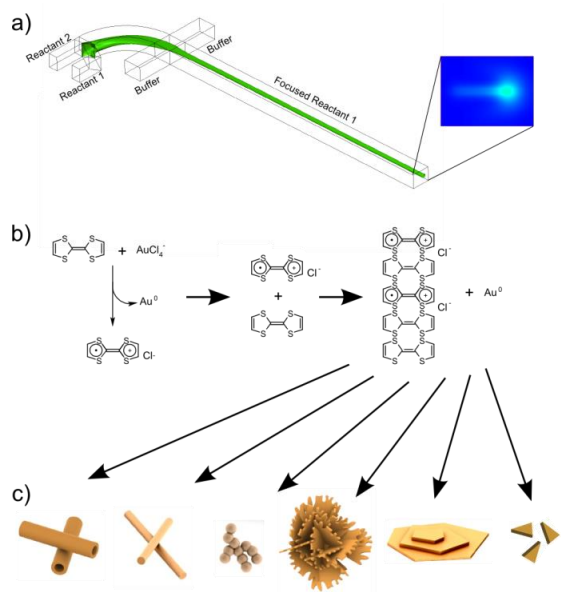


Figure 1: (a) A schematic of the microfluidic device and the simulation result of the focused reagent iso-surface. (b) Chemical reaction used to synthesis the TTF-Au hybrid structure. (c) Schematic of different structured obtained..

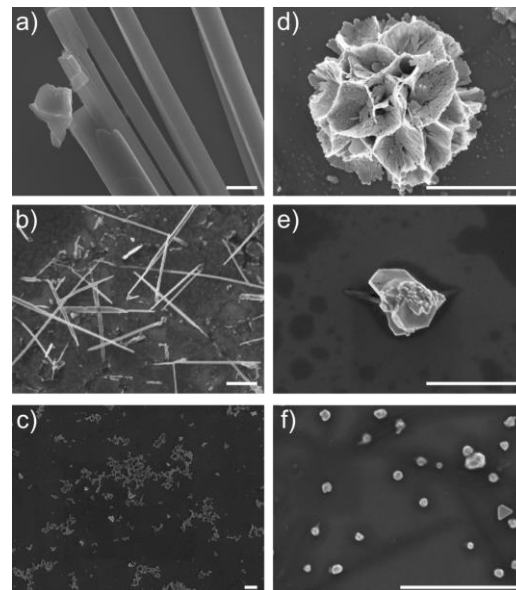


Figure 2: The SEM images of the particles fabricated by 3D focusing method. The scale bar size is 1  $\mu\text{m}$ .

## REFERENCES:

- [1] A. Ciesielski, C.-A. Palma, M. Bonini, and P. Samori, "Towards supramolecular engineering of functional nanomaterials: pre-programming multi-component 2D self-assembly at solid-liquid interfaces.," *Advanced materials (Deerfield Beach, Fla.)*, vol. 22, no. 32, pp. 3506-20, Aug. 2010.
- [2] K. F. Jensen, "Microreaction engineering — is small better?," *Chemical Engineering Science*, vol. 56, no. 2, pp. 293-303, Jan. 2001.
- [3] J. I. Park, A. Saffari, S. Kumar, A. Günther, and E. Kumacheva, "Microfluidic Synthesis of Polymer and Inorganic Particulate Materials," *Annual Review of Materials Research*, vol. 40, no. 1, pp. 415-443, Jun. 2010.
- [4] A. Rozanski et al., "Shear-induced crystallization of isotactic polypropylene based nanocomposites with montmorillonite," *European Polymer Journal*, vol. 45, no. 1, pp. 88-101, Jan. 2009.
- [5] V. Génot et al., "Synthesis of organic nanoparticles in a 3D flow focusing microreactor," *Chemical Engineering Journal*, vol. 161, no. 1-2, pp. 234-239, Jul. 2010.
- [6] M. Rhee, P. M. Valencia, M. I. Rodriguez, R. S. Langer, O. C. Farokhzad, and R. Karnik, "3D Hydrodynamic Focussing for confined precipitation of nanoparticles within microfluidic channels," *Sensors And Actuators*, no. October, pp. 992-994, 2010.

## Polyplex Synthesis by "Microfluidic Drifting" based Three-Dimensional Hydrodynamic Focusing Method

Mengqian Lu<sup>(a)</sup>, Yi-Ping Ho<sup>(b), (c)</sup>, Christopher L. Grigsby<sup>(b)</sup>, Ahsan Ahmad Nawaz<sup>(a)</sup>, Kam W. Leong<sup>(b)</sup>, Tony Jun Huang<sup>(a)</sup>

<sup>(a)</sup>The Pennsylvania State University, USA

<sup>(b)</sup>Duke University, USA

<sup>(c)</sup> Interdisciplinary Nanoscience Center (iNANO), Denmark

We synthesized polymer-DNA nanocomplexes (polyplexes) using a "microfluidic drifting" based three-dimensional (3D) hydrodynamic focusing in a single-layered, microfluidic device [1,2]. This synthesis method requires no additional chemical treatment steps or any post processing. Compared with the conventional bulk mixing method [3,4], the polyplexes prepared by our "microfluidic drifting" 3D focusing method showed smaller size, slower aggregation rate and higher transfection efficiency. This "microfluidic drifting" 3D focusing method provides a simple, fast, and repeatable method to synthesize high-quality polyplexes, which can be used in nucleic acid therapeutics to reduce the cost and complexity.

The experimental setups are shown in Fig. 1. The DNA solution was focused after injection through inlet A. The polymer (turbofect) solution was injected from inlets B, C and D. The polyplexes were collected at the outlet directly without further purification or separation. For comparison, we also prepared polyplexes by vigorous pipetting the mixture of 1 ml of turbofect solution and 0.5 ml DNA solution (i.e., bulk mixing method). The polyplex size was directly measured using the Zetasizer NanoS system. The biological performance of the polyplexes was studied by transfection of the human embryonic kidney (HEK293T) cells. Flow cytometry was used evaluation of the transfection efficiency and apoptosis assay after Annexin-V (AV) and Propidium Iodide (PI) staining.

The 3D focusing method prepared polyplexes shows smaller size compared to those prepared by standard pipetting method, as shown in Fig. 2(a). Fig. 2(b) shows the aggregation kinetics. The polyplexes prepared by bulk mixing method showed significant aggregation, mainly due to the imbalanced surface charge. However, 3D focusing method can produce polyplexes with obviously slower aggregation rate, most likely due to the more uniform surface properties, eliminating to some extent the aggregation or flocculation that typically occurs in bulk. Fig. 3 showed the HEK293T cells transfected by turbofect polyplexes. The morphology of cells are similar in both cases, but there are obviously more GFP positive cells in the case of 3D focusing method. Fig. 4(e) and (f) illustrated the biological performance of the polyplexes. Polyplexes prepared by 3D focusing method showed higher transfection efficiency compared to the ones prepared by the bulk mixing method, while the apoptosis assay suggested similar cytotoxicity in both cases. Therefore, without any additional treatment or chemical stabilizers, 3D focusing method can generate polyplexes with smaller size, diminished aggregation, and higher transfection efficiency.

In conclusion, we have demonstrated polyplexes synthesis using a 3D hydrodynamic focusing method in a single-layered device. The polyplexes prepared by this 3D focusing method show smaller size, a slower aggregation rate and higher transfection efficiency compared to the ones prepared by the bulk mixing method. Such characteristics are considered particularly beneficial for large-scale pharmaceutical applications. The improved reproducibility and efficacy derived from this 3D focusing synthesis may contribute to the future development of translational nucleic acid therapeutics.

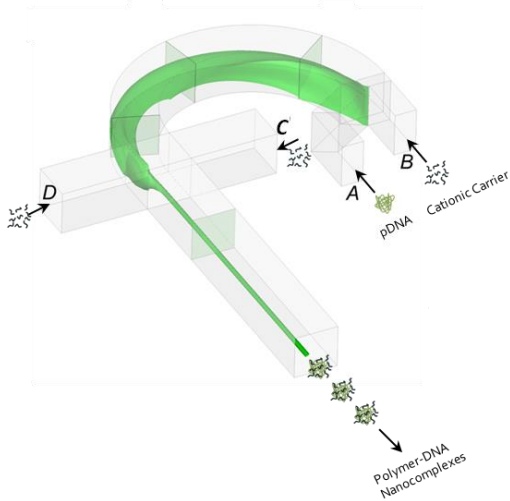


Figure 1: Schematics of the device for polyplex synthesis.

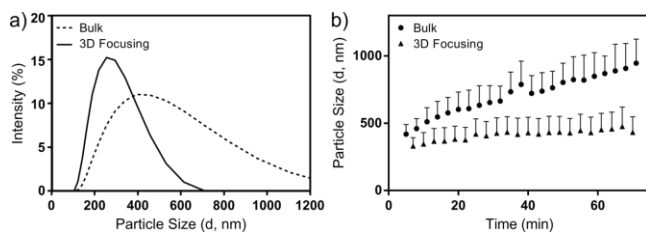


Figure 2. Comparison of polyplexes prepared by bulk mixing method and 3D focusing method. (a) Intensity-based size distribution obtained under the reaction condition of  $2\mu\text{L}$  Turbofect reagent per  $\mu\text{g}$  of pDNA; (b) aggregation kinetics.

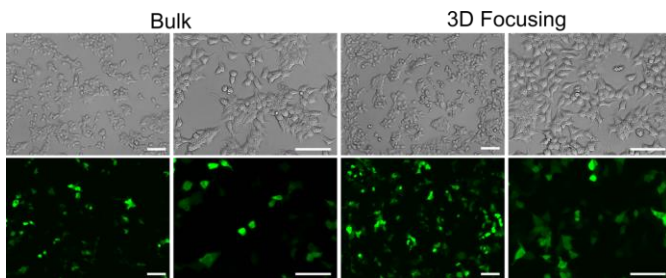


Figure 3. Microscopic observation. After 24 h post-transfection, the HEK293T cells transfected by turbofect polyplexes were examined by microscopy and assayed using flow cytometry. The morphology of cells are similar in both cases. There are obviously more GFP positive cells in the case of 3D focusing method.

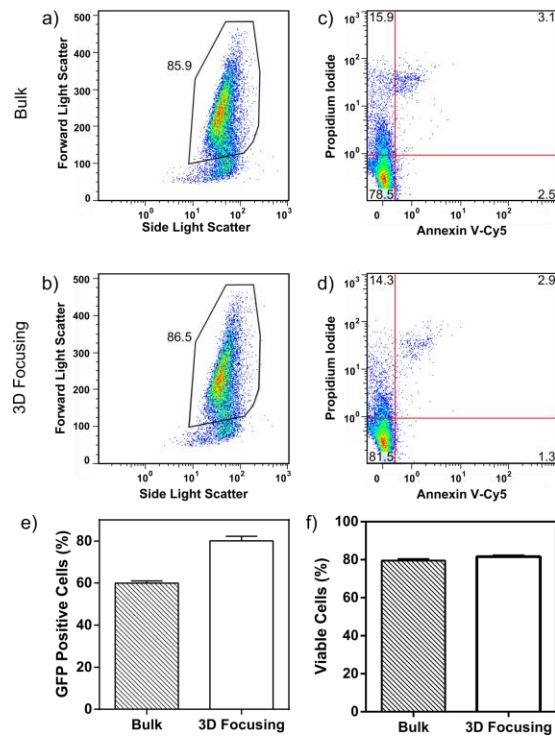


Figure 4. Quantification of transfection efficiency and toxicity.

## REFERENCES

- "Microfluidic drifting'-implementing three-dimensional hydrodynamic focusing with a single-layer planar microfluidic device," X. Mao, J. R. Waldeisen, T. J. Huang, *Lab Chip* **7**, 1260 (2007).
- "Single-layer planar on-chip flow cytometer using microfluidic drifting based three-dimensional (3D) hydrodynamic focusing," X. Mao, S-CS. Lin, T. J. Huang, *Lab Chip* **9**, 1583 (2009).
- "Mechanistic studies on aggregation of polyethylenimine-DNA complexes and its prevention," V. K. Sharma, M. Thomas, A. M. Klibanov, *Biotech. Bioeng.* **80**, 614 (2005)
- "Physicochemical characterization and purification of cationic lipopolyplexes," Y. Xu, S. W. Hui, P. Frederik, F. C. Szoka, *Biophys. J.* **77**, 341 (1999)

# INFORMATION-THEORETIC APPROACH TO ESTIMATING DYNAMICAL COMPLEXITY OF THE NOISY DUFFING OSCILLATOR

Navendu S. Patil and Joseph P. Cusumano

Engineering Science and Mechanics Department, Penn State, PA 16802, USA

For most complex physical systems, first-principles models are not readily available, and noisy experimental time series measurements must be used to learn about their dynamics. It is of particular interest to provide objective quantification of the dynamical complexity of a system along with its intrinsic as well as extrinsic stochasticity, since these are key to the prediction of its behavior. Here, we use minimal Hidden Markov models (HMMs) built from time series data of a system collected at its *steady state* to calculate measures of dynamical complexity and randomness. These HMMs belong to a popular class of state space models and treat the observed time series as a random function of sequence of Markovian states which are predictively optimal. We use Grassberger-Crutchfield-Young complexity, or simply, *statistical complexity* [1], denoted by  $C_\mu$ , which quantifies the amount of dynamically relevant “information storage” required for its optimal prediction. Our HMMs are minimal in the sense that they have lowest  $C_\mu$  among all candidate HMMs which are predictively optimal. We quantify the degree of unpredictability using the entropy rate  $h_\mu$ , which is the average uncertainty remaining about the future per unit time, of a discrete stochastic process, given the entire past of the process. However, such models, built using causal-state splitting reconstruction (CSSR) [2], need sequences of *discrete* observables generated from a typically continuous phase space. Thus, before constructing such HMMs it is important to obtain a “faithful” (i.e. dynamically equivalent) coarse-grained, symbolic description of the dynamical system using its time series measurements alone. Generating partitions provide such a description, by establishing a one-to-one correspondence between a dynamical trajectory in the continuous phase space and a symbol sequence which discretizes that trajectory. However, they are not easy to find from time series data alone, and fail to be defined in the presence of process noise.

In this work, we refine an existing algorithm [3] based on the concept of *symbolic shadowing* to numerically estimate generating partitions for the two-well, driven, Duffing oscillator, given by a second-order nonlinear ordinary differential equation:

$$\ddot{x} + \delta\dot{x} - x + x^3 = f\cos(\omega t), \quad (1)$$

where the overdot denotes the derivative with respect to time, and we fix the forcing amplitude and frequency to  $f = 0.4$  and  $\omega = 1$ , respectively. The damping parameter  $\delta$  was allowed to vary between 0.2 and 0.55. For a given partition, each observed string of length  $l$  is represented by  $m$  backward symbols and  $n+1$  forward symbols with respect to its center:  $S_{-m}S_{-m+1}\cdots S_{-1}\cdot S_0S_1\cdots S_n$ , so that  $l = m + n + 1$ , where the symbols  $S_i$  take values from a finite

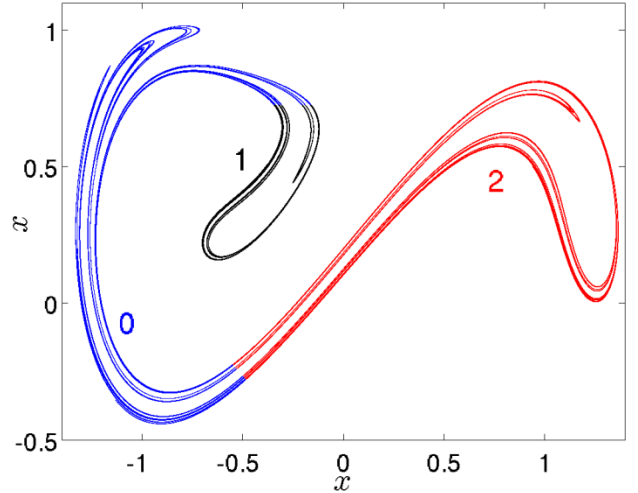


Figure 1: Generating partition consisting of 3 cells for a strange attractor of the two-well, driven Duffing oscillator (Eq. 1) with damping parameter  $\delta = 0.4$ . The phase space,  $(x, \dot{x}) \in \mathbb{R}^2$ , shows iterates of the Poincaré map, each of which is obtained by numerical integration of Eq. 1 for half the forcing period (i.e. from 0 to  $\pi$ ) followed by inversion of coordinates:  $x \rightarrow -x$  and  $\dot{x} \rightarrow -\dot{x}$ . Using this partition, sequence of points on the attractor can be converted into a symbol sequence with a 3-symbol alphabet  $\{0,1,2\}$  without loss of any dynamically relevant information.

alphabet. Thus each string corresponds to a set of points, known as a *cylinder*, in the continuous phase space belonging to a particular cell (with  $S_0$  matched to its label) and with its pre-images and images visiting cells labeled by backward ( $S_{-m}S_{-m+1}\cdots S_{-1}$ ) and forward ( $S_1\cdots S_n$ ) substrings respectively. Symbolic shadowing identifies each cylinder with a single point known as its *representative*, establishing a one-to-one correspondence with its string, and iteratively updates cylinders and their representatives to obtain improved partitions as string lengths become sufficiently large. These improved partitions are expected to yield representatives that approximate points on the attractor (Fig. 1) in the continuous phase space with increased accuracy. However, in the original algorithm [3],  $m$  and  $n$  are fixed to  $\lfloor l/2 \rfloor$  and  $\lfloor (l-1)/2 \rfloor$  respectively, for given  $l$ . Since the local expansion and contraction of nearby trajectories in continuous phase space are typically not equal, we expect that forward and backward symbols may not be equally effective in finding good representatives. Thus we choose a value of  $m = m_{opt}$  for given  $l$  (with,  $n_{opt} = l - m_{opt} - 1$ ) that *optimizes* the locations of representatives by minimizing the average Euclidean

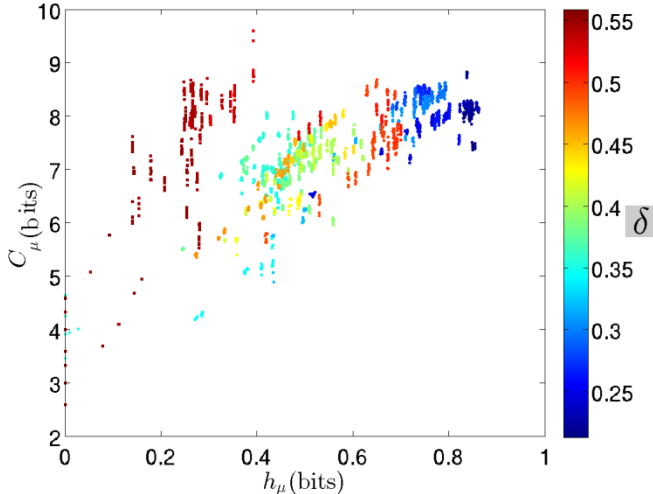


Figure 2: Complexity-entropy diagram for the Duffing oscillator. Each point on the diagram corresponds to a particular damping parameter  $\delta$ . The entropy rate,  $h_\mu$  quantifies the quality of optimal prediction and the statistical complexity  $C_\mu$  quantifies memory required to achieve optimal prediction. As can be seen for  $\delta > 0.5$ , although entropy rates are quite low ( $h_\mu \approx 0.3$  bits), the values of  $C_\mu$  ( $\approx 8$  bits), are comparable to those for  $\delta < 0.3$  for which  $h_\mu \approx 0.8$  bits.

distance between them and points in the continuous phase space. Using this modification we are able to obtain a previously known generating partition [4] (see, Fig. 1) starting from a large ensemble of 3-symbol random colorings of the phase space. We then employ a simple continuation approach, starting from the optimized partition, to study the system for a range of damping parameter values. In this manner, we are able to obtain good partitions with minimal manual intervention from time series data, at hundreds of damping values at which system behaves chaotically. This facilitates application of the CSSR algorithm to build HMMs required to characterize the complexity of a system. For this, we use the statistical complexity,  $C_\mu$ , which is a measure of the amount of information, or “memory” needed to make an optimal prediction:  $C_\mu$  is zero for independent random processes (e.g., sequence of unbiased coin flips) and is only  $\log_2 n$  for deterministic period- $n$  process. On the other hand, the entropy rate,  $h_\mu$ , of a discrete stochastic process takes the maximum possible value of  $\log_2 k$  for a statistically independent random sequence over a  $k$ -symbol alphabet, and equals zero for deterministic sequences. In other words, for discrete state processes which are either independent random, or deterministic, optimal prediction can be done with ease (because statistical complexity  $C_\mu$  is low), but the quality of such predictions are poor for independent random processes (because the entropy rate  $h_\mu$  is high), while discrete deterministic sequences are perfectly predictable. In contrast, discrete stochastic processes obtained from faithful encoding of deterministic chaotic systems, which are of interest here, have high values of  $C_\mu$  and intermediate values

of  $h_\mu$ , indicating that such processes are not only difficult to predict but their best prediction may be quite poor. In this way,  $C_\mu$  and  $h_\mu$  provide complementary information allowing us to characterize the system generating observed data, and possibly distinguish a broad spectrum of discrete stochastic processes with regard to their predictive capacity.

For the validation of the modeling procedure, we compare estimates of  $h_\mu$  obtained from our minimal HMMs against the sum of positive Lyapunov exponents, which are expected to agree based on Pesin’s identity [5]. Lyapunov exponents quantify the average rate of divergence of nearby trajectories in phase space, [6] and can be estimated without the use of generating partitions. If the partitions are non-generating, in the sense that longer symbol sequences do not localize points in phase space, then it is expected that the estimated entropy rates will be significantly lower than the sum of positive Lyapunov exponents.

As shown in Fig. 2, we find that the Duffing oscillator has low to medium ( $h_\mu \approx 0.86$  bits at  $\delta \approx 0.2$ ) unpredictability relative to the maximally unpredictable independent random process (which, for a 3-symbol alphabet is  $h_\mu = \log_2 3 = 1.585$  bits). As  $\delta$  increases, the strange attractor becomes thinner in the phase space and its fractal dimension reduces. In fact for  $\delta > 0.5$ , although entropy rates are quite low ( $h_\mu \approx 0.3$  bits), the values of  $C_\mu$  are comparable to those for  $\delta < 0.3$ . This indicates that significant “resources” (in the form of memory to store the information from the past) may still be required in achieving optimal prediction even if the system is highly deterministic. Using this approach, we are also able to examine the effect of added stochastic fluctuations on the complexity and predictability of the Duffing oscillator, even though generating partitions cannot be rigorously defined.

## REFERENCES

- [1] J. Crutchfield, K. Young, “Inferring Statistical Complexity”, *Phys. Rev. Lett.*, vol. 63(2), pp. 105-108, 1989.
- [2] C. Shalizi, K. Shalizi, “Blind Construction of Optimal Nonlinear Recursive Predictors for Discrete Sequences.”, in *Uncertainty in Artificial Intelligence: Proceedings of the Twentieth Conference (UAI 2004)*, Arlington, Virginia, pp. 504-511, 2004.
- [3] Y. Hirata, K. Judd, D. Kilminster, “Estimating a generating partition from observed time series: Symbolic shadowing”, *Phys. Rev. E*, vol. 70, 016215, 2004
- [4] F. Giovannini, A. Politi, “Homoclinic tangencies, generating partitions and curvature of invariant manifolds”, *J. Phys. A: Math. Gen.*, vol. 63(2), pp. 1837-1887, 1991.
- [5] A. Fraser, *Hidden Markov Models and Dynamical Systems*, SIAM Press, Philadelphia, 2008.
- [6] R. Hegger, H. Kantz, T. Schreiber, “Practical implementation of nonlinear time series methods: The TISEAN package”, *Chaos*, vol. 9(2), pp. 413-435, 1999

# TUNABLE MICROFLUIDIC GRADIENT GENERATOR VIA ACOUSTICALLY OSCILLATED SHARP EDGES

Po-Hsun Huang,<sup>a</sup> Chung Yu Chan,<sup>a</sup> Yuliang Xie,<sup>b</sup> Nitesh Nama,<sup>a</sup> Yuchao Chen,<sup>a</sup>  
Lin Wang,<sup>c</sup> and Tony Jun Huang<sup>a,b</sup>

<sup>a</sup>Department of Engineering Science and Mechanics, The Pennsylvania State University,  
University Park, Pennsylvania 16802, USA

<sup>b</sup>Department of Chemical Engineering, The Pennsylvania State University,  
University Park, Pennsylvania 16802, USA

<sup>c</sup>Ascent Bio-Nano Technologies Inc., State College, Pennsylvania 16802, USA

We present the spatially and temporally controlled generation of chemical gradients inside a microfluidic channel using the acoustic streaming phenomenon induced by the oscillation of sharp-edges. By controlling the driving voltage of piezoelectric transducer, we have demonstrated that the chemical gradient profiles can be easily altered (spatially controlled). Furthermore, by controlling the actuation time of the piezoelectric transducer, pulsatile chemical gradients can be generated (temporally controlled). With these two characteristics combined, a spatiotemporally tunable gradient generator are developed, which has great importance in mimicking microenvironment for a wide variety of biological process.

Fig. 1 schematically shows the design of our microfluidic gradient generator: a single-layer PDMS microchannel with multiple sharp-edges was fabricated and bonded onto a glass slide, and a piezoelectric transducer was then attached adjacent to it. We used fluorescein and PBS solutions to characterize the different chemical gradients generated. Briefly, upon the actuation of piezoelectric transducer, the sharp edges are acoustically oscillated to generate acoustic streaming effects around the tip of each sharp-edge, and to mix the fluids. Due to the step-like arrangement of sharp-edges, the fluids are mixed in a step-wise fashion. With different arrangements of sharp edges, we can generate chemical gradients with different shapes (such as linear and parabolic shown in Fig. 1).

When the piezoelectric transducer was OFF, a side-by-side laminar flow was observed due to the nature of low Reynolds number in microfluidic channel [Fig. 2(a)]. Once the piezoelectric transducer was actuated, the acoustic streaming induced mixing in a step-wise fashion was observed, thereby generating concentration gradients of fluorescein [Figs. 2(b)-(d)]. To verify the gradients generated, the cross-sectional fluorescence intensity profiles at downstream position (dashed line) were plotted [Fig. 2(e)]; as expected, the linear gradients were obtained. In addition, gradients can be tuned as we change the driving voltage of the piezoelectric transducer.

Fig. 3 shows the concentration gradients that we generated using the design in Fig. 1(b), which is expected to generate parabolic gradients. Different concentration gradients were experimentally observed when different driving voltages of the piezoelectric transducer were applied [Figs. 3(b)-(d)]. The parabolic gradients were experimentally obtained, as it was expected to be [Fig. 3(e)]. Furthermore, the gradient profiles were changed as the driving voltages changed, again suggesting that the gradient profiles can be spatially controlled by adjusting the driving voltage.

In summary, spatially and temporally stable gradients with tunable concentration profiles can be generated with our sharp-edge based gradient generator. In contrast to most existing microfluidic gradient generators, in which the gradients are formed solely based on the diffusion of fluids, our device generates the gradients in a controllable manner. Using our device, it is possible to generate gradients with more complex profiles by either changing the driving voltages or the arrangement of sharp-edges. In addition, temporally changing gradients can be generated by easily controlling the driving voltage and the actuation time of the piezoelectric transducer. Our device can be useful in many chemical and biological studies and applications, such as investigating cell chemotaxis, differentiation, and migration in dynamic chemical environment.

**FIGURES:**

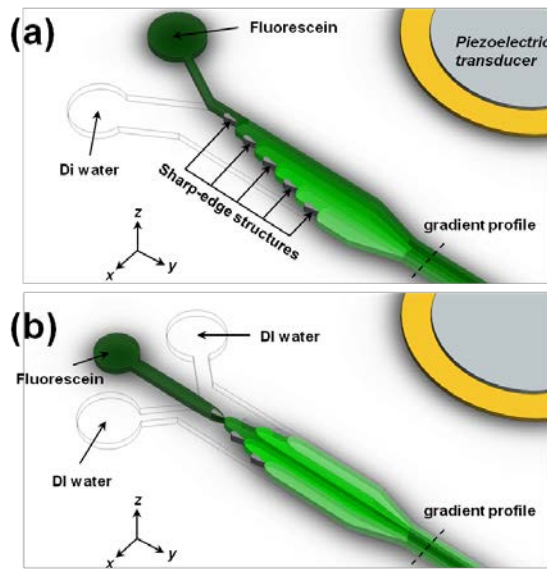


Figure 1: Schematic showing the design of sharp-edges based microfluidic gradient generator: (a) linear gradient, and (b) parabolic gradient.

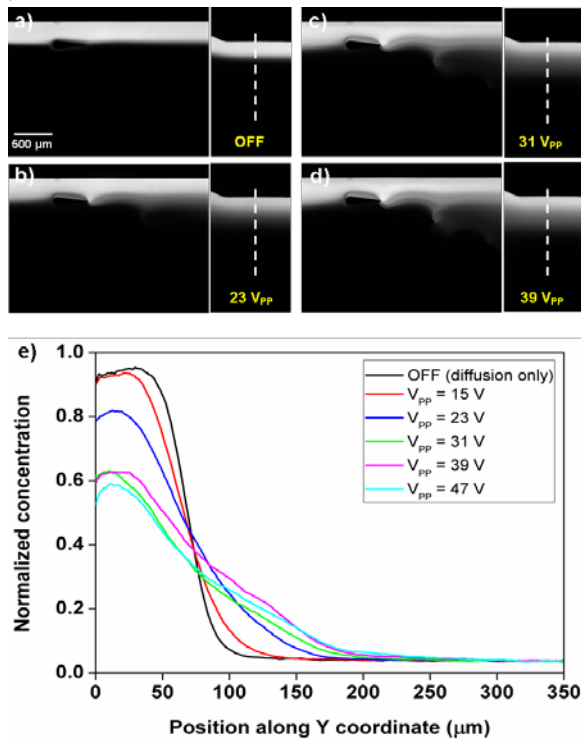


Figure 2: Characterization of generated gradients under different driving voltages: (a) the piezoelectric transducer is OFF, (b)  $V = 23$  VPP, (c)  $V = 31$  VPP, (d)  $V = 39$  VPP, and (e) Corresponding intensity profiles at downstream positions (dashed line). [The image on the right side in each figure was taken at downstream position (dashed line in Fig. 1)]

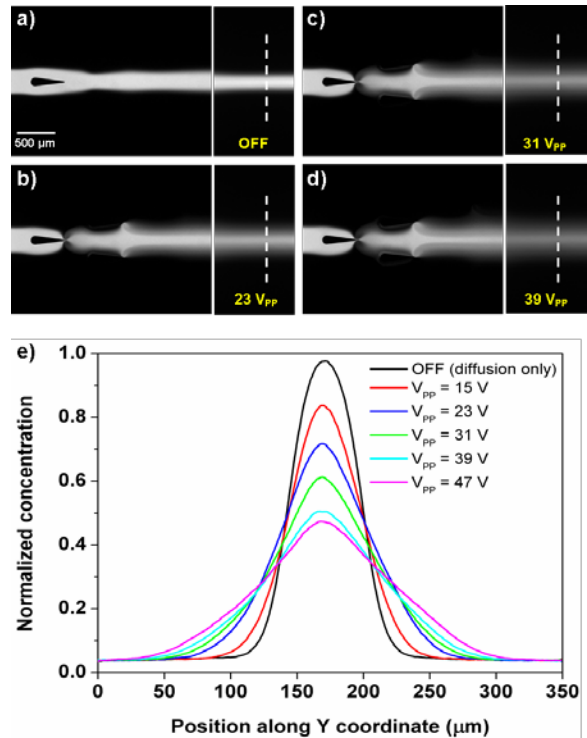


Figure 3: Characterization of generated gradients under different driving voltages. (a) the piezoelectric transducer is OFF, (b)  $V = 23$  VPP, (c)  $V = 31$  VPP, (d)  $V = 39$  VPP, and (e) Corresponding intensity profiles at downstream positions (dashed line).

**REFERENCES:**

1. P. Herson, M. N. McClean, L. Mahadevan, and S. Ramanathan, Proc. Natl. Acad. Sci. U.S.A. 105, 7165 (2008).
2. D. Ahmed, C. y. Chan, S.-C. S. Lin, H. S. Muddana, N. Nama, S. J. Benkovic, and T. J. Huang, Lab Chip 13, 328 (2013).
3. Z. Yang, S. Matsumoto, H. Goto, M. Matsumoto, and R. Maeda, Sens. Actuator A-Phys. 93, 266 (2001).

# MATERIALS FABRICATION FROM SQUID RING TEETH PROTEINS

*Abdon Pena-Francesch<sup>1</sup>, Bulent Akgun<sup>2</sup>, Melik C. Demirel<sup>1,3\*</sup>*

<sup>1</sup> Materials Research Institute, and Department of Engineering Science and Mechanics, Pennsylvania State University, University Park, PA 16802, USA

<sup>2</sup> Center for Neutron Research, National Institute of Standards and Technology, Gaithersburg, MD 20899, USA and Department of Materials Science and Engineering, University of Maryland, College Park, MD 20742, USA

<sup>3</sup> Huck Institutes of Life Sciences, Pennsylvania State University, University Park, PA 16802, USA

There is an ongoing and unmet need to develop novel materials that can be produced easily from renewable resources, and which will offer a broad array of useful applications. Engineered eco-friendly, protein-based materials include various bioelastomers (*e.g.*, silk<sup>[1]</sup>), biomaterials (*e.g.*, protein scaffolds<sup>[2]</sup>) and modular biopolymers (*e.g.*, poly-peptides<sup>[3]</sup>) that provide similar or enhanced properties compared to synthetic alternatives. Squid ring teeth (SRT) is a thermoplastic protein-based material extracted from the tentacles of squid suction cups. This protein exhibits an unusual and reversible solid to melt phase transition, enabling it to be thermally shaped into 3D geometries such as fibers, colloids, and thin films. Due to this reversible transition, the SRT protein melt presents an underwater adhesive strength of 1.5 MPa, which is at least two orders of magnitude stronger than conventional synthetic adhesives and ten times the strength of other biological adhesives. Here, we show that SRT proteins have excellent mechanical and chemical properties in wet and dry conditions that exceed most natural and synthetic polymers, in addition to their unique capability of being thermally remodeled into multiple functional forms.

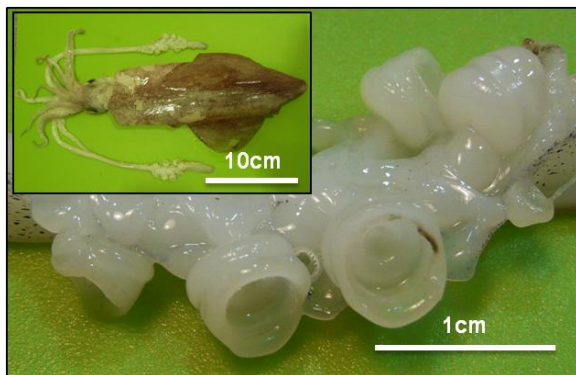


Figure 1 – European squid (*Loligo vulgaris*) and its suction cups in the tentacles, containing Squid Ring Teeth (SRT) <sup>[4]</sup>

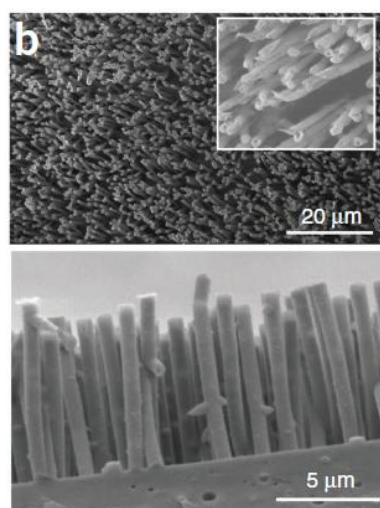


Figure 2 – Nanotubes of 800nm diameter fabricated from bulk SRT by nanowetting <sup>[5]</sup>

## REFERENCES

- [1] D. N. Rockwood, R. C. Preda, T. Yücel, X. Wang, M. L. Lovett, D. L. Kaplan, *Nature protocols* 2011, 6, 1612.
- [2] R. Langer, D. A. Tirrell, *Nature* 2004, 428, 487.
- [3] R. L. DiMarco, S. C. Heilshorn, *Advanced Materials* 2012, 24, 3923.
- [4] A. Pena-Francesch, B. Akgun, W. Zhu, H. Gao, M. C. Demirel, *Advanced Functional Materials* 2014, (submitted).
- [5] P. A. Guerette, S. Hoon, Y. Seow, M. Raida, A. Masic, F. Tian, M. C. Demirel, A. Pena-Francesch, S. Amini, G. Tay, A. Miserez, *Nature Biotechnology* 2013, 31, 908.

## IMMUNOLOGICAL ANALYSES OF WHOLE BLOOD VIA HIGH PRECISION “MICROFLUIDIC DRIFTING” BASED FLOW CYTOMETRY

*Ahmad Ahsan Nawaz, Ruth Helmus Nissly, Peng Li, Joseph Rufo, Yuchao Chen, Feng Guo, Sixing Li, Arooj Qureshi, Yanhui Zhao, Adem Ozcelik, and Tony Jun Huang.*

Engineering Science and Mechanics Department, Penn State, PA-16802, USA

Health care programs have been undergoing a transformation by decentralization of clinical labs since the inception of point-of-care (POC) diagnostics. Monitoring personal health via easy-to-operate, low cost and yet reliable diagnostics can play a vital role in improvement of global health care programs especially in resource poor settings. For example, the home blood glucose testing device has helped millions acquire accurate and fast information about the blood insulin needed to maintain healthy daily activities. However, most other hematological and immunological tests must be performed at clinical labs that are centralized due to expensive equipment and skilled operators required for their use. Furthermore, two often neglected complications of hematological and immunological tests are the conditions of transport and time required to deliver the sample to the laboratory, which can significantly alter the credibility of the results. Even in otherwise straightforward medical circumstances, wrong and inaccurate results can be fatal. Hence, development of reliable POC diagnostics is essential for fast and efficient results.

For immunological and hematological based diagnostics, flow cytometry is an established and reliable tool. One popular application is CD4+ cell counting from whole blood of human immunodeficiency virus (HIV)-infected patients, which is extremely important for determining the appropriate prescription of antiretroviral therapy to combat this infectious disease. Screening tumor biopsies, immunophenotyping and DNA content analysis are additional applications where flow cytometry is used in cancer diagnostics.

Despite the fact that flow cytometry is a well-accepted tool, its potential and utility is limited to large centralized institutions due to its many specialized requirements. A bulky footprint, high equipment cost, and requirement for highly skilled personnel for operation and maintenance significantly diminish the conventional flow cytometer's utility as a POC device. Production of large amounts of biohazardous material is often a byproduct of conventional flow cytometry, putting operators and the environment at risk of infection or contamination. In resource-poor settings, unstable electricity and limited availability of clean water pose other hindrances that demand a portable cytometer that uses low battery power, consumes little liquid and produces minimal waste.

Here, we report a novel microfluidic flow cytometry device that uses the 180° channel design and uses just one inlet for sheath fluid, has one inlet for sample injection, and can measure three parameters simultaneously with an on-chip integrated optical fiber based illumination and detection system. We performed an in-depth comparison of a novel 3-parameter (forward scatter (FSC), side scatter (SSC) and fluorescent (FL) emission) integrated microfluidic drifting based flow cytometer with a conventional machine (Beckman Coulter FC500). Our presented device utilizes 550  $\mu\text{l}/\text{min}$  of sheath fluid via one inlet and 15  $\mu\text{l}/\text{min}$  of sample fluid via a second inlet. We calibrated our device for FSC, SSC and FL detection using the commercial standard 10  $\mu\text{m}$  Flow-Check calibration beads. Subjection to a stringent 8-peak rainbow calibration bead test demonstrated the ability of our flow cytometer to differentiate fluorescent signals of eight intensities, an important test for reliable immunological based cytology studies. Next, cell count comparison with a hemocytometer was performed. Finally, we performed immunological analysis on human blood from a healthy donor and compared the results to a commercial flow cytometer for CD4+ lymphocyte cell count. Our results showed good agreement with the results from a commercial flow cytometer and within acceptable range, suggesting that this device may be useful as a POC diagnostic microfluidic flow cytometer.

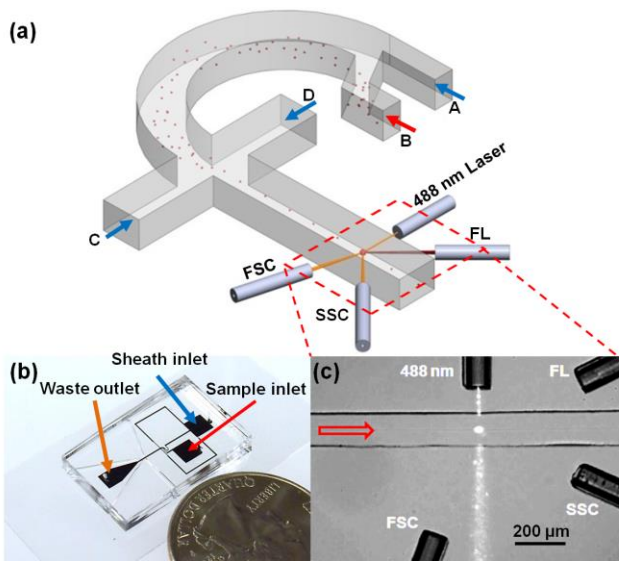


Figure 1: Microfluidic drifting based flow cytometry device. (a) Schematic of the device indicating the 180° curved region that results in cells/particle focusing and the detection region of the device depicted with input fiber for 488 nm laser and three (forward, side and fluorescence) detection fibers. A C and D are sheath fluid entry points while B represents the sample inlet. The cells/particles focus in the middle vertical plane as they move around the curved channel. The vertically focused cells/particles are then squeezed into a single stream of particles. (b) Small footprint of the device in comparison to US quarter. The device includes a single inlet for the sheath fluid and a single inlet for sample fluid. (c) Bright field microscope image of the cells/particle interrogation region (rectangular region in (a)). Shown is an instant when laser light illuminates a fluorescent 10 μm polystyrene bead as it passes through.

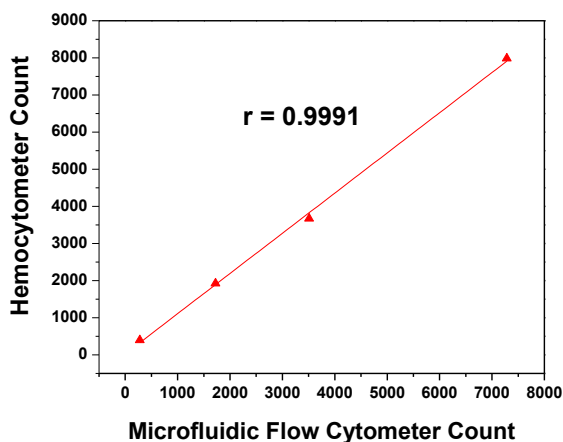


Figure 2 PS bead counts at different dilutions using the microfluidic flow cytometer compared with a hemocytometer. Correlation of  $r = 0.9991$  indicates good congruency between the count values from hemocytometer and microfluidic flow cytometer.

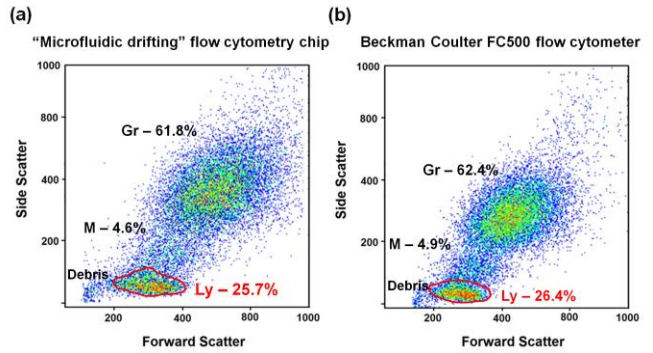


Figure 3: Comparison of forward scatter vs. side scatter plot of lysed whole blood from the microfluidic flow cytometer (a) vs. a commercial Beckman Coulter FC500 flow cytometer (b). Each dot indicates a single cell. Percentages of different subpopulations such as Granulocytes (Gr), Monocytes (M), Lymphocytes (Ly, red outlined region indicative of general location of these cells), were obtained via the autogating function of FlowJo software.

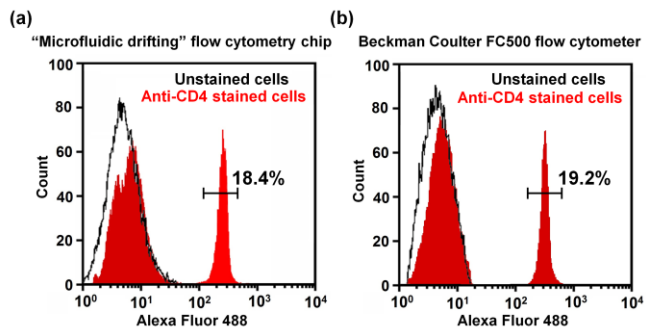


Figure 4: Comparison of Alexa Fluor 488-labeled anti-CD4 stained whole blood on the microfluidic flow cytometer (a) and a commercial Beckman Coulter FC500 flow cytometer (b). The black curve represents an unstained control sample of the blood and the colored curves represent the stained sample. Before fluorescence analysis, cells were gated on lymphocytes, as shown in Figure 6, to exclude monocytes, which also express CD4.

## REFERENCES:

- [1] Gottwald, E., B. Lahni, G. Lüdke, T. Preckel, and C. Buhlmann. Intracellular HSP72 detection in HL60 cells using a flow cytometry system based on microfluidic analysis. *Biotechniques* 35:358–62, 364, 366–7, 2003.
- [2] Jayat, C., and M. H. Ratinaud. Cell cycle analysis by flow cytometry: principles and applications. *Biol. Cell* 78:15–25, 1993.
- [3] Morris, K. Mobile phones connecting efforts to tackle infectious disease. *Lancet Infect. Dis.* 9:274, 2009.
- [4] Laerum, Ole Didrik and Bjerknes, R. *Flow Cytometry in Hematology*. Academic Press, 1992.

## **RED BLOOD CELL AND PLATELET COUNT OF NEWBORNS VIA MICROFLUIDIC DRIFTING FLOW CYTOMETRY**

*Ahmad Ahsan Nawaz, Ruth Helmus Nissly, Peng Li, Joseph Rufo, Yuchao Chen, Arooj Qureshi, Yanhui Zhao, Adem Ozcelik, and Tony Jun Huang.*

Engineering Science and Mechanics Department, Penn State, PA-16802, USA

Newborn babies are at higher risk of many infectious diseases than adults. Jaundice, sepsis, sickle cell disease are some of such conditions, which if unchecked can become life-threatening. A complete blood count, the most important and most common test that evaluates the condition of three main blood cell types i.e. red blood cells, white blood cells and platelets. For neonates this test must be conducted within 12 hours of birth for immediate evaluation of the health. However, the amount of blood that a newborn has depends on their weight. At birth a baby has approximately 76.6 ml of blood which increases to 83.3 ml in twenty-four hours. Complete blood count of neonates, hence cannot be done in a regular way by drawing 10 ml of blood (as in adults who have approximately 5-7 liters of blood) which is > 10% of complete blood volume and could be life threatening.

Flow cytometers and hematology analyzers are the gold standards for complete blood count. Although, significant efforts are being extended, these units still require blood amount (1 ml to 5 ml) which is not suitable for newborns. Tests, however have to be delayed thus also delaying the treatment in case of any deficiency in the newborn.

Here we have demonstrated a microfluidic drifting based flow cytometry device that utilizes just 5  $\mu$ l of blood for counting of red blood cells and platelets. Our microfluidic drifting based flow cytometer measures four parameters (forward scatter, side scatter, 525 nm emission signals, 575 nm emission signals) simultaneously via on-chip integrated optical fiber detection system. For red blood cells the forward scatter optical fiber at 3° to the incident laser light (488nm) measures the size of the cells while side scatter detects the refractive index of the cells.

For this purpose, fresh venous blood was taken from a healthy donor. Within 17 hours of drawing, we fixed the whole blood within 1 ml of 4% paraformaldehyde in PBS (Santa Cruz Biotechnology, Inc.) and incubated at room temperature for 10 min. Next, 5  $\mu$ l of CD41 monoclonal anti-human antibody was added to the blood which attaches to the platelets. This was followed by addition of 5  $\mu$ l of another PAC-1 antibody which is expressed by activated platelets only.

Here, Fig 1 indicates the red blood cells are focused via a microfluidic drifting flow cytometry in the middle of the main channel. The laser light illuminates the cells. The light scattered from the cells are detected via forward scatter. The emission signals from the antibodies are detected by the 525 nm and 575 nm detector fibers.

Preliminary results of red blood cell counting in terms of forward scatter vs side scatter of the whole blood are shown in Fig. 2

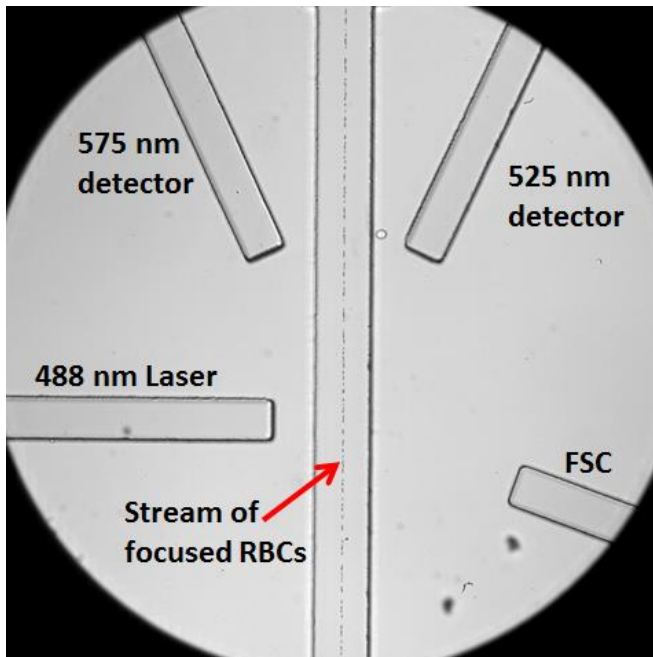


Figure 1: Red blood cells focused in the middle of channel. The 488 nm blue laser is illuminated onto the red blood cells. The scatter signal is detected by FSC detection fiber, the fluorescent emission signals are detected by 525 nm and 575 nm detection fibers.

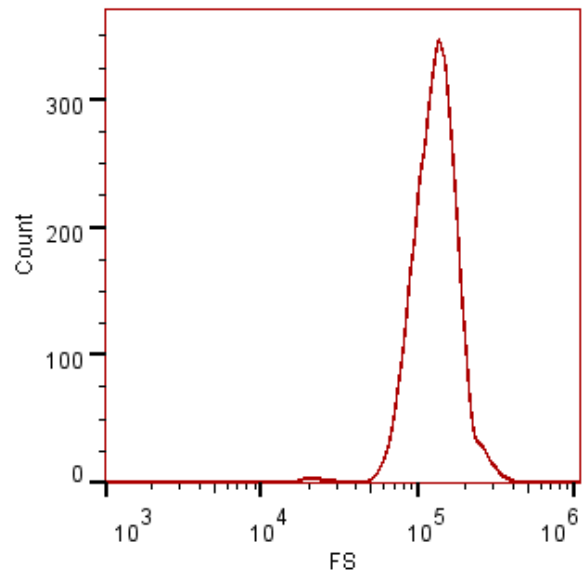


Figure 3: The histogram indicates the red blood cells as a single population.

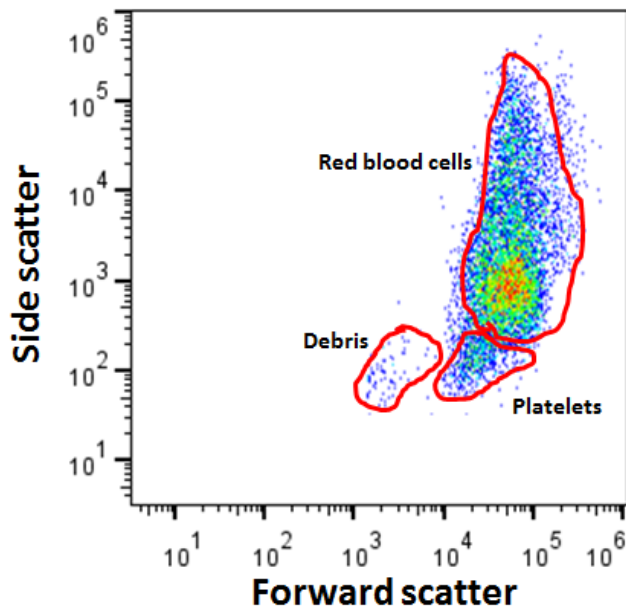


Figure 2 Forward scatter vs side scatter plot of human whole blood. Each dot is generated as a result of a cell passing the laser interrogation region. The plot indicated the red blood cells and platelets.

#### REFERENCES:

- [1] Hasan R, Inoue S, Banerjee A. Higher white blood cell counts and band forms in newborns delivered vaginally compared with those delivered by cesarean section. *Am J Clin Pathol.* 1993;100(2):116–118
- [2] Adair CE, Kowalsky L, Quon H, et al. Risk factors for early-onset group B streptococcal disease in neonates: a population-based case-control study. *CMAJ.* 2003;169(3): 198–203

# Shape and Stiffness-Changing Structures based on Fluidic Flexible Matrix Composites (F<sup>2</sup>MCs)

*Aniruddh Vashisth and Charles E. Bakis*

Department of Engineering Science and Mechanics, The Pennsylvania State University,  
University Park - 16802, PA, USA

Inspired by the fibrillar networks in plant cell walls, a highly mechanical advantageous actuator system is made from composite tube consisting of a flexible matrix and multiple layers of oriented high performance fibers. These fiber reinforced elastomers are known as Flexible matrix composites (FMCs). A significant change in stiffness and shape could be obtained by using a valve control for pressuring FMC tubes with a nearly incompressible fluid. A fluid with a high bulk modulus resists volume change that would normally occur with an open valve. So, by closing the valve, the tube becomes much stiffer than in the open valve case. By varying the fiber angle and matrix material of these tubes a wide range of stiffness ratios can be obtained. Therefore, by varying the internal pressure, the tube behaves like an actuator. Such composites are termed as fluidic flexible matrix composites (F<sup>2</sup>MCs). These materials

are stiff in one direction yet compliant in others. The F<sup>2</sup>MC tubes (2 mm diameter) in this investigation have three layers, with neat polyurethane for the inner and outer layers and stainless steel reinforced polyurethane for the middle layer. Multiple small F<sup>2</sup>MC tubes are embedded in potting matrix, to make laminated skins and analyze them. Multi-layered laminates with F<sup>2</sup>MC tubes embedded multi-directionally could display actuation and variable stiffness by pressurizing different layers. Such composites could be used as structural elements for morphing and variable stiffness structures. Over the long term, this line of research is aimed at the development of thin skins for structures that can change shape and stiffness differently as a function of direction. Future application would include synthetic arms for robots, morphing wings for aircrafts etc.

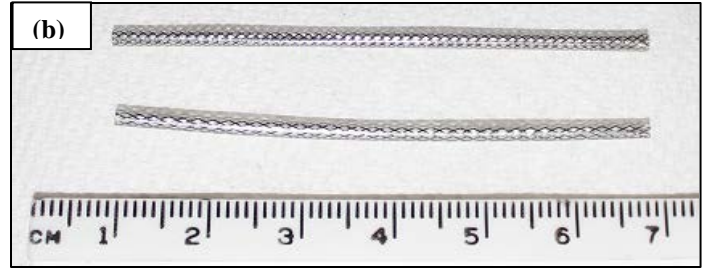
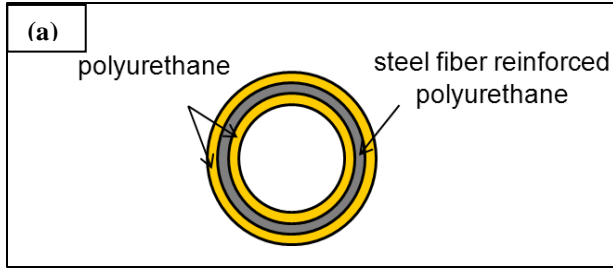


Figure1. (a) Three layered polyurethane  $F^2MC$  tube (b) Photographs of steel reinforced, braided FMC tubes along with cm scale

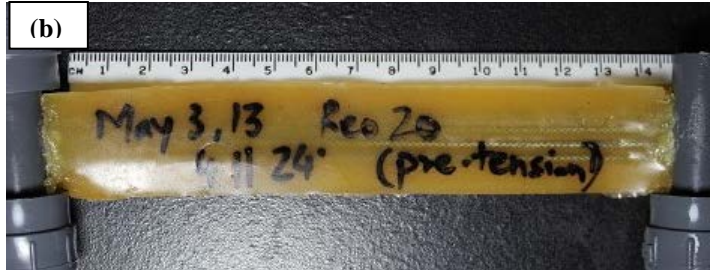
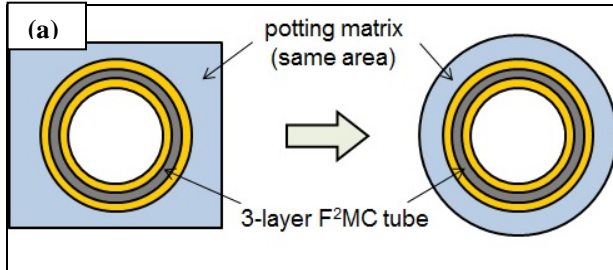


Figure2. (a) We assume that the  $F^2MC$  tubes are arranged side-by-side in a rectangular array and then potted in the resin, resulting in a cross section of a unit cell as shown in Figure a. (b) Photograph of cured laminate along with cm scale

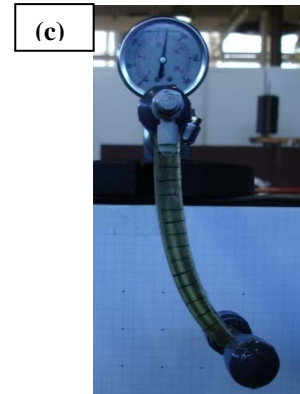
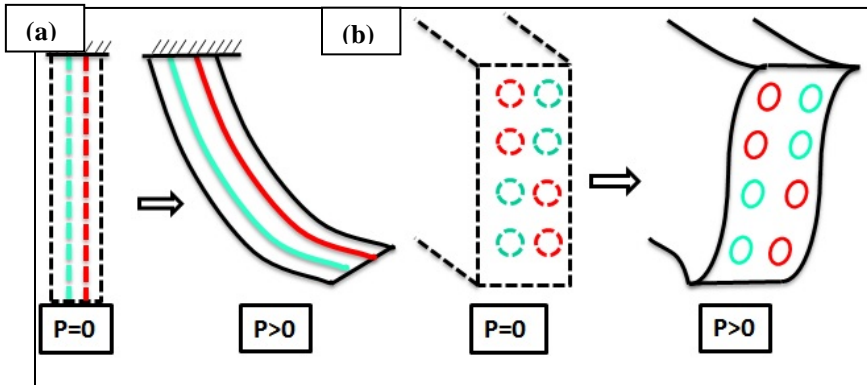


Figure3. (a) Warping and (b) twisting actuation of multi-layered laminate upon pressurization. Red and blue lines show  $F^2MC$  tubes with different fiber orientation. (c) Photograph of warping in laminate at 170 psi fluid pressure.

**Reference:**

Vashisth, A., Zhu, B., Wimmer, B. M., Bakis, C. E., and Rahn, C. D., "Evaluation of Millimeter-Size Fluidic Flexible Matrix Composite Tubes" *Proc. ASME Conf. on Smart Materials, Adaptive Structures and Intelligent Systems, SMASIS2013*, Snowbird, Utah.

# VALIDATION AND VERIFICATION OF AN OVERSET FLUID-STRUCTURE INTERACTION SOLVER

*C. W. Elsworth, J. S. Pitt, S. T. Miller*

Engineering Science and Mechanics Department, Penn State, PA-16802, USA

For many years, classical mechanics sub-disciplines have been studied independently, but recent advancements in computational power and parallelism have brought about the emergence of research into coupled systems. A coupled system, in general, consists of two or more physically or computationally dissimilar domains, which are constrained to each other such that they interact dynamically [1]. These domains are often very different, requiring a solution that combines the traditionally independent mechanics sub-disciplines. One such coupled system of significant interest is Fluid-Structure Interaction (FSI), which sits at the intersection of solid mechanics and fluid mechanics [2].

Fluid-Structure Interaction consists of a solid immersed in, and/or containing a fluid, with coupling arising from the interplay between the fluid and solid domains. The deformation of the solid is a direct product of applied fluid stresses, while the deformation of the solid modifies the boundary conditions of the fluid domain. Computationally, this requires two-way coupling between the equations governing the fluid and the equations of motion describing the solid. Examples of FSI are prevalent in the natural world, therefore it is important to be able to understand the fundamental mechanisms behind these interactions as well as modeling them accurately. One of the most famous examples of FSI is the catastrophic failure of the Tacoma Narrows Bridge, where the self-induced oscillations matched the resonant frequency of the bridge, leading to its collapse [3].

While instances of FSI are prevalent, their computational modeling presents a variety of complications. Notably, concerns with the meshing of the domain and maintaining mesh quality during a simulation limit the types of problems that can be currently solved. For this reason, research into alternative methods is necessary to tackle more complex problems. Overset methods provide the ability to describe a complex computational domain through the decomposition of the domain into multiple independent meshes. The meshes are linked through interpolation between the overlapping regions of the meshes, and results in a complete representation of the domain. These methods allow for the prominent features of the domain to be meshed separately, simplifying meshing. In addition, they have also been demonstrated to be useful in the description of complex domains, and allow for the maintenance of mesh quality during dynamic simulations. These factors suggest that overset methods have the ability to address some of the complications experienced in realistic FSI simulations.

This talk will investigate a novel solver, which applies overset methods for the solution of computational FSI problems. The overset FSI solver implements Suggar++/DiRTlib overset methods into a partitioned FSI code. Partitioned FSI algorithms implement separate solvers for the coupled domains and iterate between them to ensure tight coupling. Figure 1 illustrates the process of a partitioned algorithm using fixed-point iterations and Aitkin under-relaxation. The ARL/PSU FSI solver is based on an OpenFOAM fluid solver and in-house structural solver, coupled by an interface class, providing a fully-coupled FSI solution [4]. The combination of two previously implemented solvers for overset and FSI processing provides a new approach to computational FSI modeling.

An overview of the partitioned solver's governing equations is presented, providing a foundation for the solution methods implemented in the overset FSI solver. Solver components are characterized and the overset FSI solver workflow is presented. Numerical validation data is provided through comparison to the Turek and Hron benchmark test case, as seen in Figure 2. Overset FSI solver benefits will be investigated, with respect to mesh generation and quality. These results will confirm that the overset FSI solver is able to address the mesh motion concerns of large deformation FSI simulations, while producing accurate results, and therefore add significantly to current computational FSI research, as demonstrated in Figure 3.

Rigorous code verification of this overset-grid enabled FSI algorithm is also presented and discussed. A collection of best practices for verifying partitioned FSI codes are also presented. Specifically, the method of manufactured solutions (see, e.g., [5]) is used to determine the order of accuracy of the code, including convergence rates and error magnitudes. The partitioned FSI algorithm introduces separate discretization schemes for the solid, fluid, and mesh motion components, requiring special care in the definition of a comprehensive verification exercise. Additionally, the sources of discretization error from each component of the solver must be combined into a single metric to determine global convergence rates.

Our strategy is to first verify each solver component independently, then reduce the verification exercise to one in which a global parameter is adjusted. This global parameter must be defined in order to capture the relative sources of error across the domain and motivates an optimal mesh refinement ratio between the fluid and solid domains. The error between exact and computed solutions can therefore be

calculated over the entire fluid-structure domain, as well as the individual fluid and solid components. For example, the mesh size of the fluid domain can be chosen as the primary parameter of error characterization, and the subsequent adjustment of solid mesh and time step size produces a solution that is globally of the same order of accuracy.

Special attention is given where overset grids are present, as the interpolation involved can significantly impact solution quality. Presented results include error magnitudes, convergence rates, and methodologies for a coherent approach to employing the method of manufactured solutions to partitioned FSI codes.

## REFERENCES

- [1] C. A. Felippa, K. Park, and C. Farhat. Partitioned Analysis of Coupled Mechanical Systems. *Computer Methods in Applied Mechanics and Engineering*, 190(24-25):3247–3270, 2001.
- [2] X. Wang. *Fundamentals of Fluid-Solid Interactions*, volume 8 of *Monograph Series on Nonlinear Science and Complexity*. Elsevier, 2008.
- [3] R. Loehner, J. R. Cebal, C. Yang, J. D. B. and Eric L. Mestreau, and O. Soto. Extending the Range and Applicability of the Loose Coupling Approach for FSI Simulations. In H.-J. Bungartz and M. Schafer, editors, *Fluid-Structure Interaction: Modelling, Simulation, Optimisation*. Springer-Verlag New York, LLC, 2006.
- [4] S. Miller, R.L. Campbell, C.W. Elsworth, J.S. Pitt, D.A. Boger. An Overset Grid Method for Fluid-Structure Interaction. *International Journal for Numerical Methods in Fluids*. Submitted October 28, 2013.
- [5] P. J. Roache. *Verification and Validation in Computational Science and Engineering*. Hermosa Publishers. Albuquerque, NM, 1998.

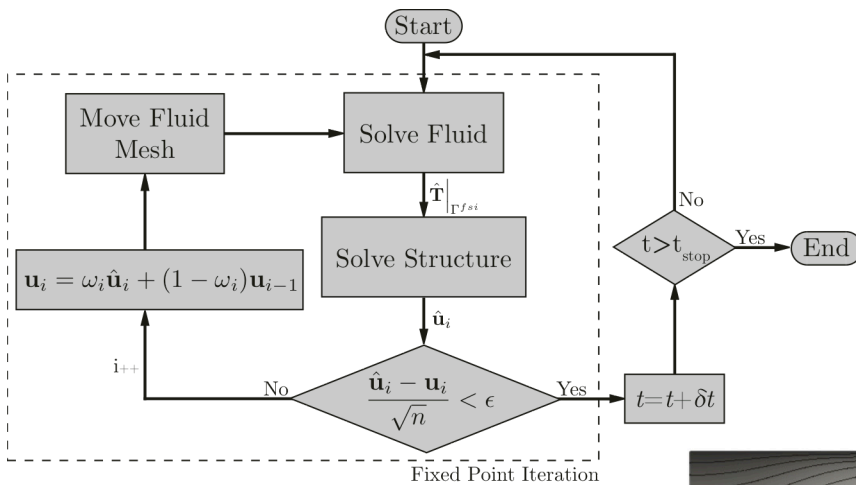


Figure 1: Detailed flowchart of partitioned FSI algorithm.

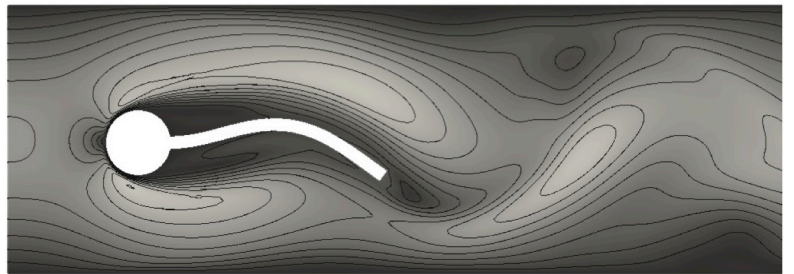


Figure 2: Simulation of the Turek-Hron benchmark case. Shaded by pressure.

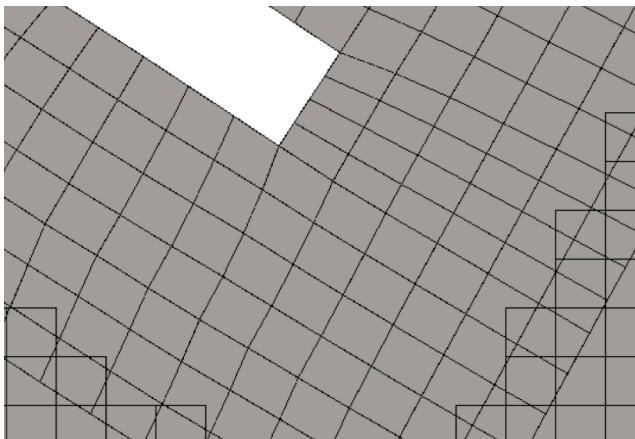


Figure 3: Detail of body-fitted mesh quality at the interface.

# SPATIAL CONTROL OF CELL INTERACTION WITH SURFACE ACOUSTIC WAVES

*F. Guo, P. Li and T. J. Huang*

Engineering Science and Mechanics Department, Penn State, PA-16802, USA

Cell-cell interaction or communication allows the coordination of cell functions, which critically regulates complicated physiological and pathological processes as embryogenesis, development of degenerative and autoimmune diseases.[1] The cells can talk with each other via directly cell-cell contact or signaling molecules in the real in vivo condition. Those complicated biological events highly rely on the spatial configuration of cells and regulation of chemical environment. The conventional cell culture approaches such as cell culture plate or petri dish suffer from the random cell distribution and uncontrollable chemical environment. [2] Better spatial and temporal control of cell assembly will facilitate the discovery of information which is often omitted in conventional in vitro studies. However, current methods of controlling cell assembly are lack of biocompatibility, flexibility, precision or throughput. Here we present a versatile tool, a tunable acoustic well, to control the spatial arrangement of cells for intercellular communication study based on surface acoustic wave technology. We demonstrated the system is able to control intercellular distance precisely, assemble cells with tunable geometry. For each critical functions of the acoustic well, we demonstrated the functional gap junction based intercellular communication by visualizing the transfer of fluorescent dyes.

In this study, we utilized the superposition of two orthogonal SSAWs, instead of previously reported inference patterns, to form dot-array configuration of pressure nodes. By depositing orthogonal digital transducers (IDTs) pairs on lithium niobate (LiNbO<sub>3</sub>) piezoelectric substrate. The generation of two overlapping orthogonal SSAWs relies on the excitation of difference resonance frequencies for different IDT pairs.[3] Figure 1 shows the schematic and actual setup of the device, respectively. Each pair of IDTs is independently connected to a radiofrequency (RF) signal to generate SAWs to apply different frequencies. Once the input signals are applied, square shape pressure nodes dot-arrays will form on substrate. Those SSAWs leak and establish a differential acoustic potential field to the adjacent fluid medium; this three dimensional field above each two dimensional square pressure node will work as “an acoustic well”.

To precise control the distance between two cells, the movement of cells must be stopped as soon as the withdrawal of the acoustic field. We applied a continuous RF signal to IDT along vertical direction and a modulated RF signal to the IDTs along horizontal direction to push cells towards each

other as 20  $\mu\text{m}$ , 10  $\mu\text{m}$ , 5  $\mu\text{m}$ , or 0  $\mu\text{m}$  (Figure. 2a). The modulated signal was set to a pulse signal with 500 ms duration and 2 s intervals. The whole process was recorded and analyzed as shown in Figure. 2b. The movement curve of step-like shape matched with the period of the modulated input signal. The movement of cells is fully controlled in suspension by regulating the input signals. We examined this method with gap junction based intercellular communication, which requires direct contact between cells or diffusion of soluble factors dependent upon the distance between the cells sending and receiving the signals. Fig. 2c showed that Calcein AM fluorescence dye can be transferred to the contacted cell after one hour, indicating the formation of functional GJIC. No fluorescence transfer can be observed after the same period of time, if two cells are separated with a very small distance (Figure. 2d, 3  $\mu\text{m}$ ).

Other than control of intercellular distance, this acoustic well approach is also suitable to trap and assemble multiple cells to form cell clusters with different geometric configurations. By employing an acoustic well with different acoustic amplitudes, the cells assemblies with linear-shape, single layer or spherical shape can be formed accordingly (Figure. 3). Those cells or cell clusters can be levitated by the acoustic radiation force and acoustic streaming induced hydrodynamic force (Figure. 4a).[4] After 30 min of initial incubation, bright field and fluorescent images of suspended cell assemblies were recorded every 5 minutes. Vivid dye coupling from donor cells (stained with Calcein AM) to receiver cells can be observed in all the linear arrays with different cell number. As expected, the larger the cell numbers, the longer it takes to observe evident dye coupling to the terminal cells (Figure. 4b-d). If the cells are patterned to a linear array, their communications are achieved linearly. If cells are patterned to a cluster, their communication format will be changed as well. We tuned the acoustic well to assemble cells into a cluster and multiple cells can receive the signal simultaneously from the donor cell (Figure. 4e).

We demonstrated the acoustic well is capable of performing multiple tasks for intercellular communication studies, including the control of intercellular distance, flexible cell assembly and communication in suspension. This acoustic well approach can be further developed for many cell-cell interaction studies including immune-cancer interaction, tissue engineering and regenerative medicine.

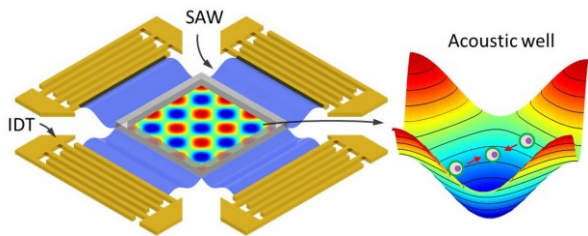


Figure 1: Schematic of “tunable acoustic well”: each pair of IDTs can generate a standing surface acoustic wave (SSAW) in one direction. The overlap of the two SSAWs can result in “well” shape configuration of pressure nodes arrays. Cells can be pushed into the middle of square pressure node.

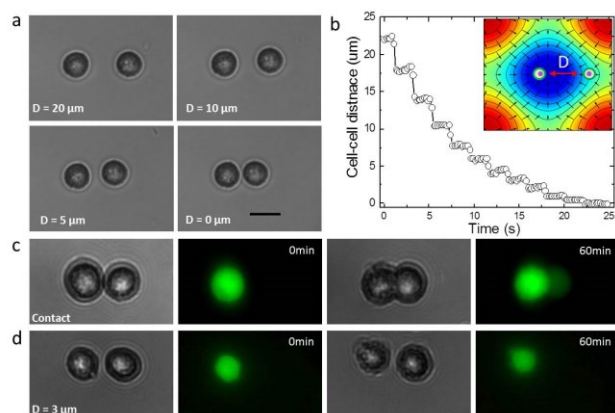


Figure 2: (a) Two HEK 293 T cells are positioned with varied intercellular distances, 20, 10, 5, 0 μm, respectively. (b) The dependence of cell-cell distance on the input signals. (c) Two contacted HEK 293 T cells. Dye transfer can be observed after 60 min. (d) Two HEK 293 T cells were positioned with a distance of 3 μm. Dye transfer between them cannot be observed after 60 min of culture.

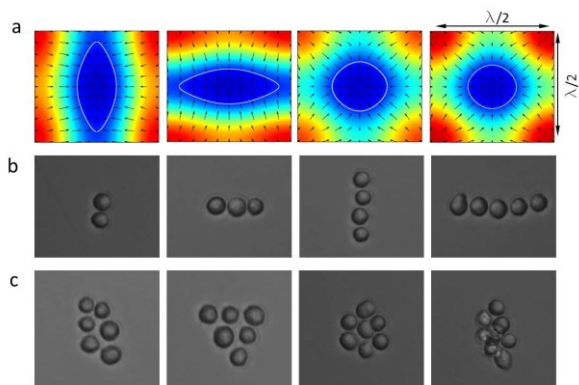


Figure 3: (a) Simulation results of acoustic potential distribution in an acoustic well with different acoustic amplitudes. (b) Linear shape of HeLa cell assemblies when applying linear shape of acoustic wells. (c) Single layer and spherical shape of cell assemblies when applying spherical shape of acoustic wells.

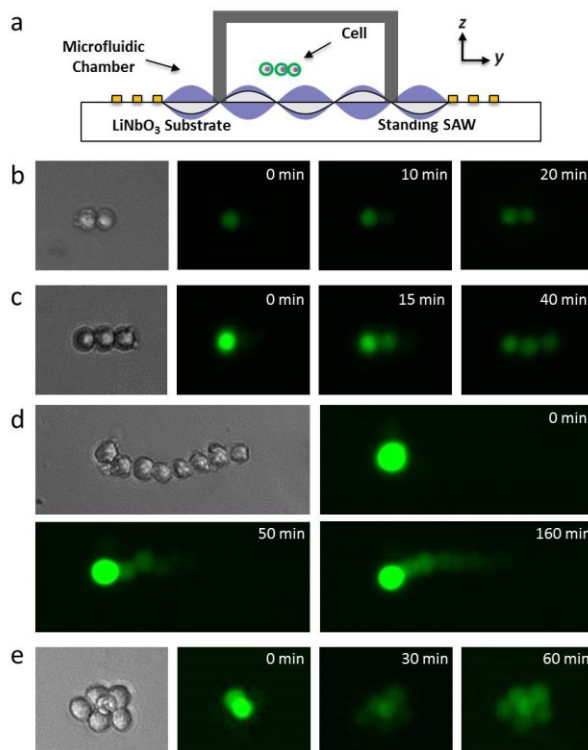


Figure 4: (a) Schematic of experimental setup. (b)-(e) Bright field image and time-lapse fluorescence images of two cells system trapped by an acoustic pressure node. Left cell was preloaded with Calcein-AM dye and dye transfer between different suspension cells assemblies can be observed over time.

## REFERENCES

- [1] C. H. Streuli, N. Bailey, and M. J. Bissell, “Control of mammary epithelial differentiation: basement membrane induces tissue-specific gene expression in the absence of cell-cell interaction and morphological polarity.,” *The Journal of cell biology*, vol. 115, pp. 1383-95, 1991.
- [2] F. Guo et al., “Probing cell-cell communication with microfluidic devices.,” *Lab on a chip*, vol. 13, pp. 3152-62, 2013.
- [3] X. Ding et al., “Surface acoustic wave microfluidics.,” *Lab on a chip*, vol. 13, pp. 3626-49, 2013.
- [4] J. Shi et al., “Three-dimensional continuous particle focusing in a microfluidic channel via standing surface acoustic waves (SSAW).,” *Lab on a chip*, vol. 11, pp. 2319-24, 2011.

# LITHIATION MECHANICS OF HIGH-CAPACITY ANODE MATERIALS

*Hui Yang and Sulin Zhang*

Department of Engineering Science and Mechanics  
The Pennsylvania State University  
University Park, PA 16802

## ABSTRACT

We present a chemo-mechanical model to investigate the lithiation-induced phase transformation, morphological evolution, stress generation and fracture in high-capacity anode materials such as silicon and germanium. The model couples lithium (Li) diffusion with elasto-plastic deformation in a three-dimensional (3D) setting. Several key features observed from recent transmission electron microscopy (TEM) studies are incorporated into the model, including the sharp interface between the lithiated shell and unlithiated core, crystallographic orientation-dependent reaction rate, and large-strain plasticity. Our simulation results demonstrate that the model faithfully predicts the anisotropic swelling of lithiated crystalline silicon nanowires (*c*-SiNWs) observed from previous experimental studies. Stress analysis reveals that lithiation anisotropy in *c*-SiNWs can lead to surface fracture at the angular sites where two adjacent {110} facets

intersect, consistent with previous experimental observations. However, as germanium and amorphous silicon nanostructures show weak lithiation anisotropy, they can remain robust without any visible cracking during the lithiation process. Moreover, large volume change due to the insertion of lithium can generate large compressive stress at the reaction front, leading to the considerable lithiation retardation. The mechanistic understanding of the morphological evolution and stress generation sheds light on the design of failure-resistant nanostructured electrodes. Our model also offers a framework for the study of the chemo-mechanical degradation in high-capacity electrode materials.

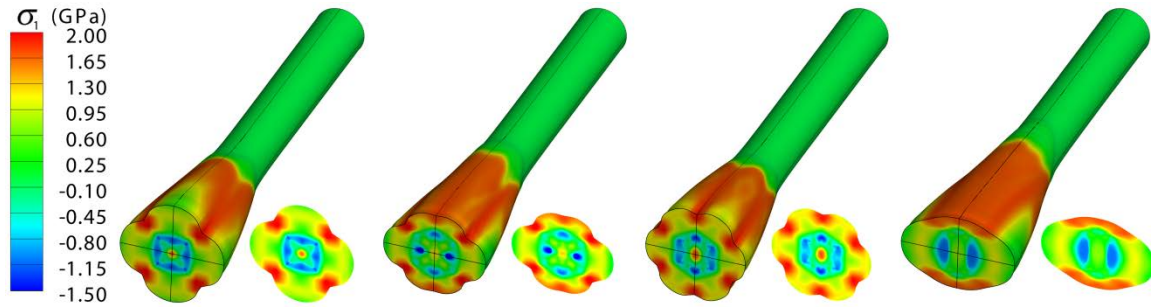


Figure 1: Chemomechanical modeling of the morphological evolutions and stress distributions in crystalline silicon nanowires upon lithiation. From left to right, the axial orientations of the SiNWs are  $\langle 100 \rangle$ ,  $\langle 110 \rangle$ ,  $\langle 111 \rangle$ , and  $\langle 112 \rangle$ . Color contours in the image indicate the maximal principal stress.

## References

- [1] H. Yang, F. Fan, W. Liang, T. Zhu, S. Zhang, "A Chemo-Mechanical Model of Lithiation in Silicon", *J. Mech. Phys. Solids*, 2014, Accepted.
- [2] H. Yang, S. Huang, X. Huang, F. Fan, W. Liang, X. H. Liu, L.-Q. Chen, J. Y. Huang, J. Li, T. Zhu, S. Zhang, "Orientation-Dependent Interfacial Mobility Governs the Anisotropic Swelling in Lithiated Silicon Nanowires", *Nano Lett.*, vol. 12, pp. 1953-1958, 2012.
- [3] W. Liang, H. Yang, F. Fan, Y. Liu, X. H. Liu, J. Y. Huang, T. Zhu, S. Zhang, "Tough Germanium Nanoparticles under Electrochemical Cycling", *ACS Nano*, vol. 7, pp. 3427-3433, 2013.
- [4] S. W. Lee, M. T. McDowell, J. W. Choi, Y. Cui, "Anomalous Shape Changes of Silicon Nanopillars by Electrochemical Lithiation", *Nano Lett.*, vol. 11, pp. 3034-3039, 2011.
- [5] X. H. Liu, J. W. Wang, S. Huang, F. Fan, X. Huang, Y. Liu, S. Krylyuk, J. Yoo, S. A. Dayeh, A. V. Davydov, S. X. Mao, S. T. Picraux, S. Zhang, J. Li, T. Zhu, J. Y. Huang, "In situ atomic-scale imaging of electrochemical lithiation in silicon", *Nat. Nanotechnol.*, vol. 7, pp. 749-756, 2012.

# A FRACTIONAL ORDER MODEL FOR LOCAL ELECTRIC FIELDS IN BIOLOGICAL TISSUES

*M. M. Hasan and C. Drapaca*

Engineering Science and Mechanics Department, Penn State University, PA 16802, USA

In recent years, electro-chemotherapy and gene electro-transfer have emerged as promising cancer therapies that use locally applied electric fields to facilitate the transport of either chemotherapeutic drugs into tumor cells or genes into target cells using the cell membrane electroporation. It is well known that the local electric field in the tissue depends on the applied voltage on the electrodes, the geometry and position of the electrodes, and on the heterogeneity and geometry of the biological tissue [1, 2]. So far, the local electric field distribution in tissues was found by solving the classic Laplace equation. However, tissues and tumors have evolving microstructures which affect the distribution of the applied electric field.

Recent experimental and theoretical results have shown that many processes in physics and engineering sciences are in fact governed more accurately by fractional order differential equations instead of traditional integer-order differential equations. Inspired by these findings, in our exploratory study we propose a fractional calculus based approach to model the electric field distribution in tissues. Our approach is based on the assumption that fractional derivatives can model the heterogeneity and multi-scale nature of dynamic materials such as living biological tissues better due to the presence of integration in the definition of the fractional derivatives. The resulting fractional differential equation of Laplace type is solved analytically. Our preliminary results on the local electric field distribution might help to find electrode configurations that will help designing cancer therapies with optimal outcome.

In this paper, we use a six needle array electrode to find the electric field distribution in tissues. The needle configuration is given in figure 1. We assume that the needles are long, with uniform thickness and fully inserted into the tissues. Therefore, the potential can be considered a two dimensional away from the tips of the needles. Assuming a constant conductivity of the tissue, the potential  $\phi(\mathbf{r})$  in the entire region outside the needle can be obtained by solving the Laplace equation:

$$\nabla^2 \phi(\mathbf{r}) = 0 \quad (1)$$

where  $\mathbf{r} = x\hat{i} + y\hat{j}$  and  $\nabla = \frac{\partial}{\partial r^2}$  is the Laplacian. Using the method of Green's functions the solution of equation (1) is:

$$\phi(\mathbf{r}) = \frac{1}{2\pi} \ln\left(\frac{a}{r}\right) \quad (2)$$

where  $\phi(\mathbf{r})$  vanishes when  $\mathbf{r} = a$ . Using now a fractional order Laplacian operator, equation (1) can be written as:

$$\nabla^{2\alpha} \phi(\vec{r}) = 0 \quad (3)$$

where  $\nabla^{2\alpha} = D_r^{2\alpha}$  is the fractional order Laplacian of Riesz derivatives and order is  $\alpha$  ( $0 < \alpha \leq 1$ ). To determine the solution of equation (3), we need to know the Green function  $G_{2\alpha}(\mathbf{r})$  that satisfies:

$$\nabla^{2\alpha} G_{2\alpha}(\mathbf{r}) = -\delta^2(\mathbf{r}) \quad (4)$$

The solution of equation (4) (and hence equation (3) as well) is [3]:

$$\phi(\mathbf{r}) = \frac{\Gamma(1-\alpha)}{2^{2\alpha}\pi\Gamma(\alpha)} \frac{1}{|r-a|^{(2-2\alpha)}} \quad (5)$$

where  $a$  is the position of the needle and  $\Gamma$  is the gamma function.

We can obtain now the solution for the six needle array electrode by keeping the applied potential  $+V_0$  on needles 3 and 4,  $-V_0$  on needles 5 and 6, and zero potential on needles 1 and 2. Therefore, the total potential is the sum of potential generated by each needle:

$$\phi(\mathbf{r}) = \sum_{n=1}^6 \phi_n(\mathbf{r}) \quad (6)$$

From the analytical results presented here, we can see that when the fractional order  $\alpha$  approaches 1, the solution (6) converges to the classical analytical solution given in [1]. The formulation developed here provides a convenient way of calculating the distribution of the electric field developed by clinically used electroporation technique.

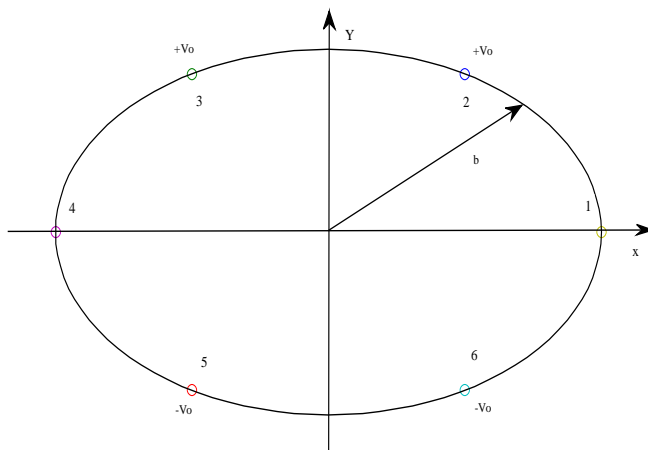


Figure 1: Electrode configuration of an array of six needles on a circle of radius  $b$ .

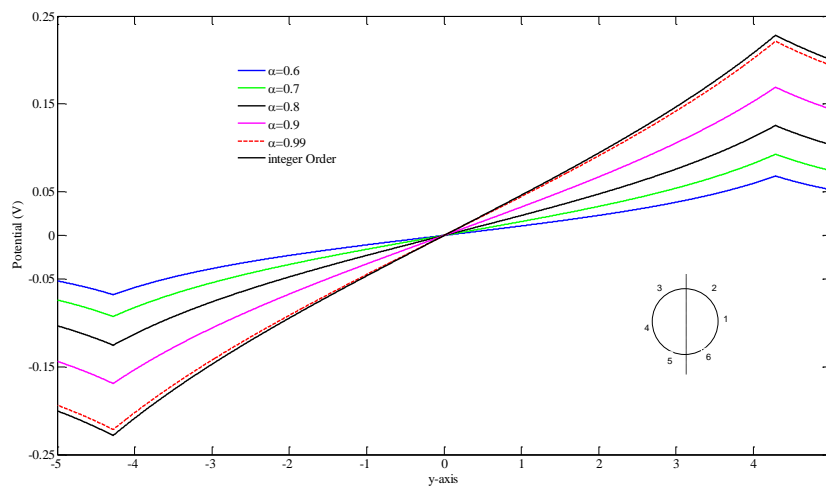


Figure 2: Potential distributions vs. position for different values of the fractional order and in the classic case.

## REFERENCES

- [1] S. B. Dev, D. Dhar, W. Krassowska, "Electric Field of a Six-Needle Array Electrode Used in Drug and DNA Delivery In Vivo: Analytical Versus Numerical Solution", IEEE Transactions on Biomedical Engineering, Vol. 50, No. 11, November 2003
- [2] S. Corovic, M. Pavlin, D. Miklavcic, "Analytical and Numerical Quantification and Comparison of the Local Electric Field in the Tissue for Different Electrode Configurations", BioMedical Engineering OnLine, Vol. 6, No. 1, pp. 37, 2007.
- [3] S. I. Mulish, O. P. Agrawal, "Riesz Fractional Derivatives and Fractional Dimensional Space", Int Theor Phys, Vol. 47, No. 2, pp. 270-275, 2010.

# ACOUSTIC STREAMING AROUND OSCILLATING SHARP EDGES

*Nitesh Nama, Po-Hsun Huang, Tony Jun Huang, Francesco Costanzo*

Department of Engineering Science and Mechanics, The Pennsylvania State University,  
University Park - 16802, PA, USA

Oscillating sharp edges have been employed to achieve rapid and homogeneous mixing in microchannels using acoustic streaming, see fig 1. These mixers utilize acoustically oscillating sharp edges to generate microvortices and perturb the flow field to achieve enhanced mixing. This work extends prior experimental studies to numerically characterize the effect of various parameters on the acoustically induced flow. We present a numerical model using a perturbation approach to study the flow around acoustically-driven, oscillating sharp edges in a microchannel. We model the fluid as compressible and linear viscous using the compressible Navier-Stokes equations. These are intrinsically nonlinear and are characterized by different behaviors over wide ranges of time and length scales. The flow on the large length- and time-scale arises from the acoustic excitation at much smaller time and length scales. Consequently, a direct solution of the compressible Navier-Stokes equation remains computationally challenging even with modern computational tools. The problem is further complicated due to the presence of singularity in the flow field at the sharp edge. To capture the singularity in the flow field, we refine the mesh near the tip of the sharp edge using an adaptive mesh refinement strategy. We employ periodic boundary

conditions to model a periodic cell representative of the full domain, thereby resulting in huge savings in computational costs and time. We investigate the effect of various parameters including the tip angle, oscillation amplitude, and channel dimensions on the flow patterns. The predicted flow profiles are found to reflect the inherent nonlinearity of the acoustic streaming phenomena as the various patterns identified are not linear scalings of one another. The flow field is found to be heavily dependent on the geometrical parameters of the device. The streaming velocity is also observed to show a quadratic dependence on the applied input displacement and a nonlinear increase with the decrease in tip angle. We also show that properties contributing to the overall mixing effectiveness of the device can be in "competition" with each other making the identification of optimal geometric and working configurations nontrivial. For this reason, we believe that our computational effort, in addition to providing better understanding of flow around sharp edges in confined microchannels, is also very useful in design optimization of sharp-edge micro-mixers which have numerous applications in many lab-on-a chip processes like biomedical diagnostics, drug delivery, chemical synthesis, enzyme reactions.

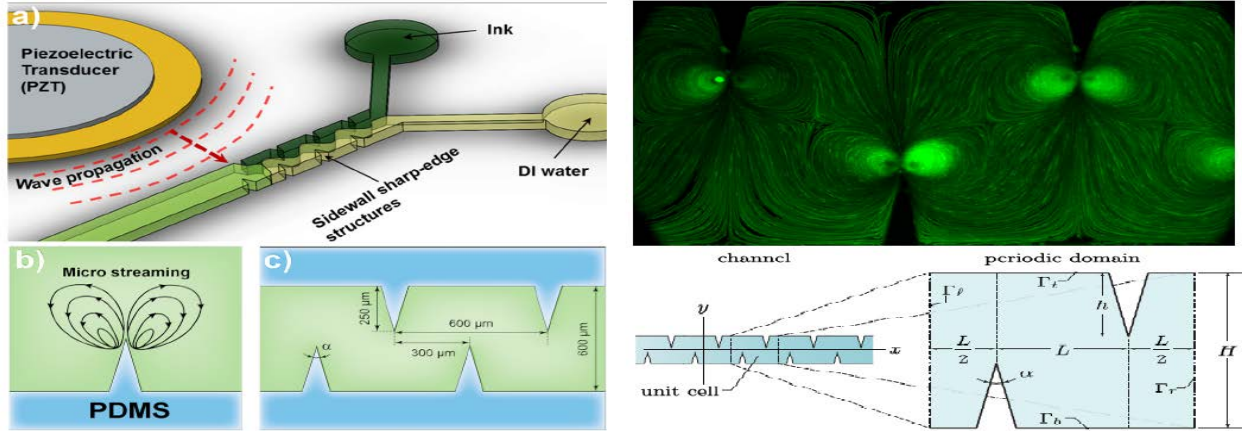


Figure 1: (a) Schematic of the device showing a micro-fluidics channel with sharp-edge structures on its side walls. (b) Typical micro streaming patterns produced in the fluid occupying the channel as a response to piezoelectric excitation. (c) Typical geometric dimensions of the corrugated channel. (d) Experimentally observed trajectories of 1.9 micron diameter fluorescent beads in our acoustically oscillated micro-mixer with sharp edges. (e) A portion of the microfluidics device and an enlarged periodic cell forming the device.

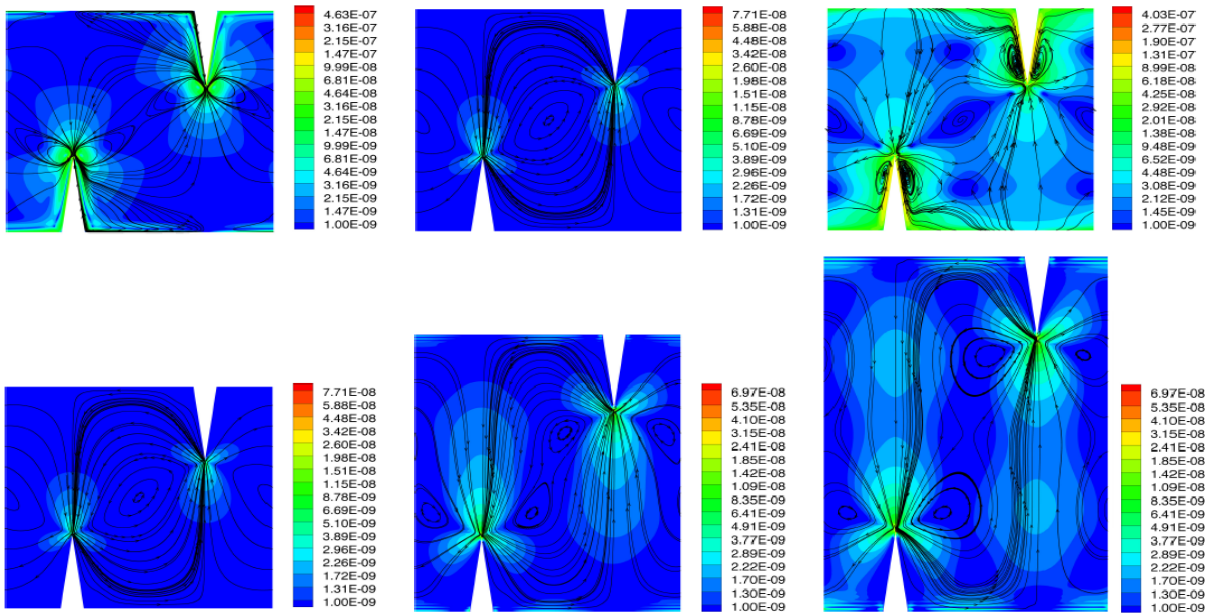


Figure 1: Plot of trajectories of (a) bead velocity (b) fluid velocity (c) mean velocity of mass flow. (d)-(f) Plot of bead trajectories for different channel heights ( $h= 300$  microns,  $400$  microns and  $500$  microns respectively).

## REFERENCES

- [1] H. Bruus, *Lab On a Chip*, 2012, 12, 1014-1021.
- [2] W. Bangerth, R. Hartmann, and G. Kanschat, *deal.II Differential Equations Analysis Library – Technical Reference*, 1998-2006.

# OPTICAL SENSING VIA SURFACE MULTIPLASMONICS

S. E. Swiontek and A. Lakhtakia

Department of Engineering Science and Mechanics, Penn State, PA-16802, USA

Several types of electromagnetic surface waves (ESWs) have been researched both theoretically and experimentally since the early 1900's. These ESWs are guided by the planar interface of two dissimilar materials. The fields of an ESW must satisfy the frequency-domain Maxwell equations in both partnering materials as well as the boundary conditions at the interface. As the material changes about the interface, so do the characteristics of the surface wave [1]. These delicate changes in surface-wave characteristics of the partnering materials makes ESWs suitable for optical detection of hundreds of biological, chemical, and bio-chemical analytes [2].

The surface plasmon-polariton (SPP) wave has dominated research in academic and industrial settings. This surface wave is guided by the interface of a metal and a dielectric material in which both partnering materials are isotropic and homogeneous. SPP waves are most commonly excited using a prism-coupled configuration. Generally, a thin metal film (tens of nanometers) is deposited by a physical vapor deposition (PVD) technique onto the hypotenuse of a 45°-90°-45° prism. That metal then partners air. When a  $p$ -polarized plane wave is incident onto one side of slanted face at an angle  $\theta$  above the critical angle  $\theta_c$  of the prism, most of the light is reflected toward the other slanted face of the prism. The remainder is absorbed. When the reflected light is plotted against  $\theta$ , a sharp drop in reflection indicates the excitation of an SPP wave [2].

However, since only one solution satisfies the boundary conditions for isotropic and homogeneous metal/dielectric partnering materials, only one SPP-wave mode can be excited. Thus, only *one* analyte can be detected at a given time. It has been theorized that more than one SPP-wave mode—with different spatial profile, attenuation rates, and phase speeds—can be guided by the interface of a metal and a dielectric material, provided that the dielectric material is anisotropic and periodically non-homogeneous in the thickness direction. This can lead to *multiple analyte detection* and/or more robust measurements with high sensitivity.

A chiral sculptured thin film (STF) meets those aforementioned requirements. A chiral STF is periodically non-homogeneous thin film comprising nanohelices oriented along the thickness direction. The chiral STF is grown on planar substrates through PVD techniques in a low-pressure vacuum chamber.

The morphology is acquired by tilting the substrate to an oblique angle  $\chi_v$  with respect to a collimated flux of an evaporated material. When a chosen value of  $\chi_v$  is reached, the substrate then rotates about an axis which passes normally through it. Deposition conditions such as the vapor flux angle  $\chi_v$ , pitch  $2\Omega$ , and number of structural periods of the chiral STF can be engineered to suit the needs of the application [3]. Exciting multiple-SPP-wave modes has long since been demonstrated experimentally by employing a chiral STF when implemented in the TKR configuration.

In proof-of-concept sensing experiments, SF-11 glass with a refractive index  $n = 1.778$  served as substrate on which a 30-nm-thick aluminum thin film followed by a two- or three-period-thick chiral STF composed of lanthanum fluoride of a pitch  $2\Omega = 400$  nm were sequentially deposited via resistive-heating PVD. The substrate was then placed on an SF-11 prism of the same optical density. An index-matching liquid was placed between the substrate with the opposite side of the thin-film stack and the prism. The TKR configuration was then affixed to a custom-built machine that measures changes in reflectance of a  $p$ -polarized beam where  $\lambda_0 = 635$  nm as a function of angle  $\theta$  [3].

A cross section of the TKR configuration is schematically shown in Fig. 1. When the pores of the chiral STF were occupied by air, three different SPP-wave modes were launched as shown in Fig 2. Platform A is a three-period-thick chiral STF where in Platform B is a four-period-thick chiral STF. When reflection dips coincide for both platforms, i.e. thickness independent, an SPP wave is launched. SPP-wave modes are indicated by '1', '2', and '3'.

When those pores are replaced by DI water ( $n_{H_2O} = 1.33$ ) the number of SPP-wave modes reduced two. The launching of these two modes is indicated by the reflectance dips labeled 1 and 2 on the solid blue line in Fig. 2. When an aqueous solution of sucrose with increasing molarity infiltrated the pores instead of water, both reflectance dips shifted to higher values of  $\theta$  as shown in Fig. 3. The sensor offers dynamic sensitivities of 90 degrees per refractive-index unit (deg/RIU) or higher, which are comparable to state-of-research values. Therefore, surface multiplasmonics can be employed for optical sensing [3].

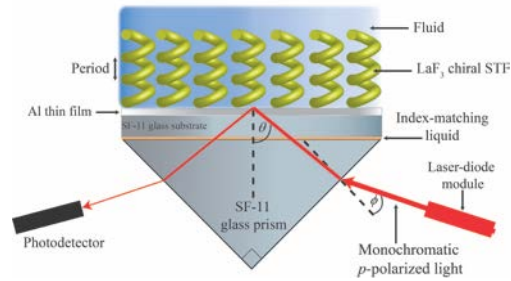


Figure 1: The schematic of the TKR configuration wherein a thin metal film, followed by a chiral STF, is deposited on a substrate. It is then placed on top of one face of a right-angle prism which is of the same optical density of that substrate. An index-matching liquid between the prism and substrate minimizes refractive-index mismatching between those two components. A monochromatic  $p$ -polarized plane wave is incident on one slanted face at angle  $\theta$ . The intensity of the beam incident light diminishes with each refracted step the light takes inside the prism, until it exits from one leg of the prism, as shown.

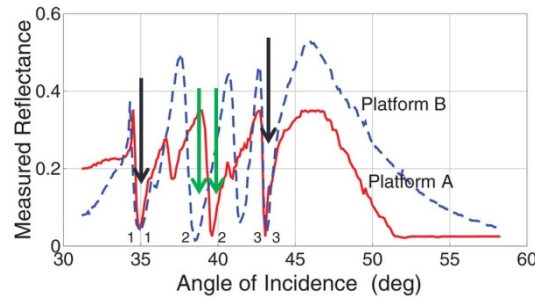


Figure 2: Measured reflectance as a function of angle of incidence  $\theta$  at  $\lambda_o = 635$  nm of a three- and four-period-thick chiral STF implemented in the TKR configuration. Arrows pointing to the three dips in the graph indicate that multiple SPP-wave modes can be launched at a single frequency and interface, thus promising multi-analyte detection.

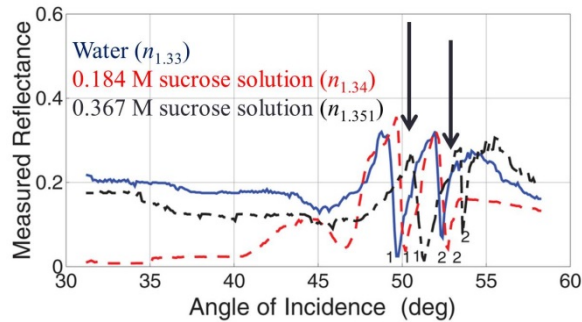


Figure 3: Measured reflectance as a function of angle of incidence  $\theta$  at  $\lambda_o = 635$  nm of a three-period-thick chiral STF implemented in the TKR configuration. Reflectance where water infiltrated the void regions of the chiral STF is shown in blue, 0.184-M solution of sucrose in red dashed, and 0.367-M sucrose solution in black dashed. This graph shows optical sensing of analytes in solution with a multiple-SPP-wave platform. Arrows point to the general locations of the SPP-wave modes.

## REFERENCES

- [1] J. A. Polo Jr., T. G. Mackay, and A. Lakhtakia, *Electromagnetic Surface Waves: A Modern Perspective*, Elsevier, NY, USA, 2013
- [2] I. Abdulhalim, M. Zourob, and A. Lakhtakia, "Surface plasmon resonance for biosensing: a minireview," *Electromagnetics.*, **28**, pp. 214-242, 2008.
- [3] S. E. Swiontek, D. P. Pulsifer, and A. Lakhtakia, "Optical sensing of analytes in aqueous solutions with a multiple surface-plasmon-polariton-wave platform," *Scientific Reports*, **3** 1409, 2013.

# COARSE-GAINED MODELING OF PLASMODIUM FALCIPARUM INFECTED ERYTHROCYTE MEMBRANE: STRUCTURAL MODIFICATIONS LEAD TO LOSS OF DEFORMABILITY

Y. Zhang, C. Huang, M. Golkaram, S. Zhang

Engineering Science and Mechanics Department, Penn State, PA-16802, USA

*Plasmodium falciparum*, the most virulent human malaria parasite, invades human erythrocytes, exports proteins to modify erythrocyte membrane, endows erythrocyte with high stiffness and cytoadherence and then enables erythrocyte to block blood vessels and cause dysfunction of organs[1, 2]. The dramatic loss of erythrocyte deformability plays a critical role in the pathogenesis of *P. falciparum* malaria[3]. Despite progress in experimental studies on erythrocyte remodeling triggered by *P. falciparum* infection, the underlying mechanism of how the structural modifications of erythrocyte membrane lead to the impressive loss of deformability remains elusive. Using a coarse-grained composite erythrocyte membrane model[4, 5], capable in incorporating structural modifications caused by *P. falciparum*, we systematically investigated shear elasticity of the erythrocyte membrane. Our simulation results show that though spectrin network accounts for the shear modulus of healthy erythrocyte, pure alteration of spectrin network would not induce remarkable increase in the shear modulus. It is the knob formation that significantly influences erythrocyte membrane via tightening association between spectrin network and lipid bilayer, strengthening spectrin network and hardening local lipid bilayer. Locally hardened lipid bilayer would not behave like a fluid in healthy erythrocyte but more like a solid to promote the shear modulus. Evolution of knob density and size also plays an important role in enhancing the shear modulus. Shear moduli of *P. falciparum*-infected erythrocyte at different asexual stages yielded from our model are in good agreement with experimental results. Our findings offer insight into the stiffening mechanism of *P. falciparum* infected erythrocyte.

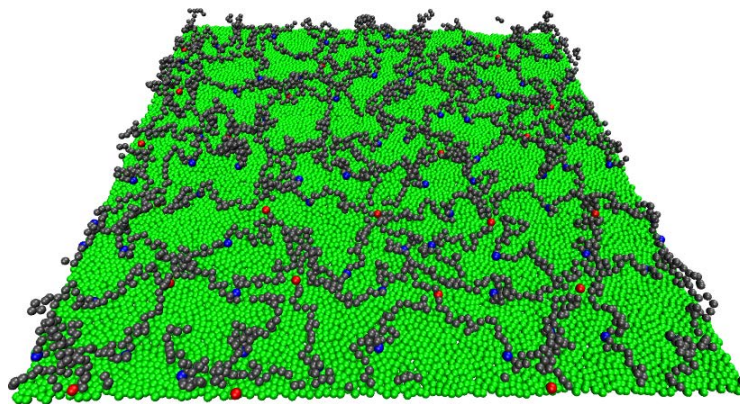


Figure 1. Coarse-grained molecular dynamics model of healthy RBC membrane including lipid bilayer and spectrin network. Green, red, blue and gray particles denote lipid particles, actin oligomers, ankyrins and spectrin beads, respectively.

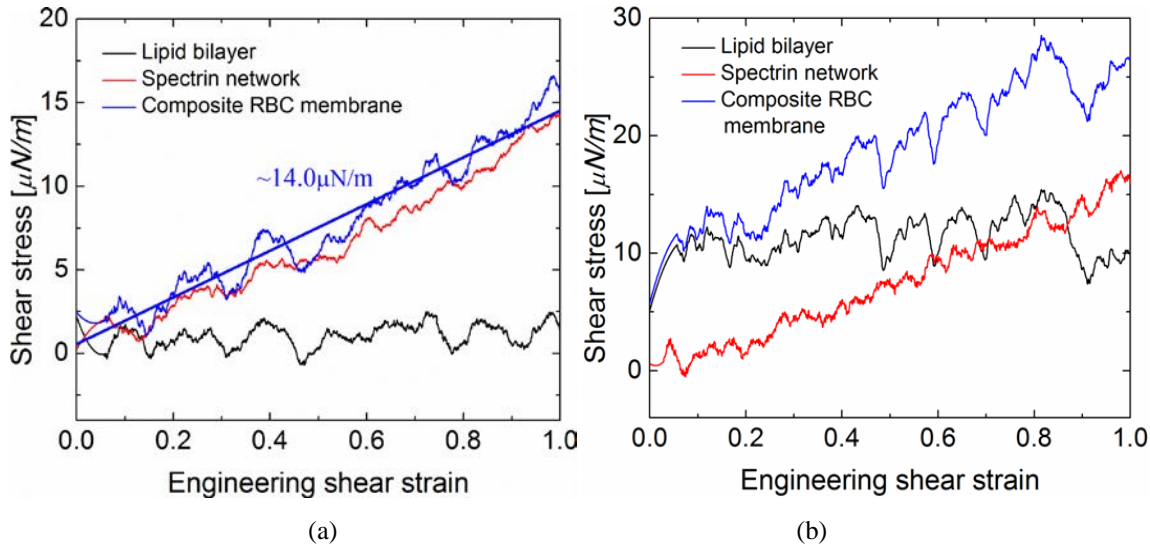


Figure 2. Shear responses of healthy RBC membrane. Shear stress-strain responses of the composite RBC membrane, the lipid bilayer and spectrin network at a low shear rate  $\dot{\gamma} = 5.71 \times 10^{-4} \tau^{-1} s^{-1}$  (a) and at a high shear rate  $\dot{\gamma} = 5.71 \times 10^{-3} \tau^{-1} s^{-1}$  (b).

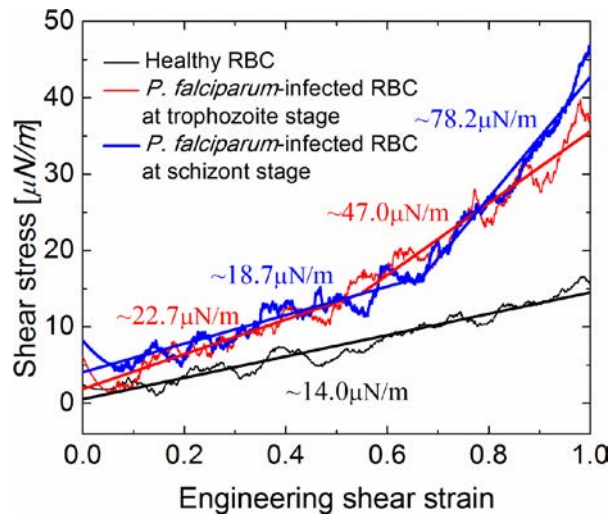


Figure 3. Shear stress-strain responses of healthy RBC membrane and *P. falciparum*-infected RBC membrane at different asexual stages. The strain rate is  $\dot{\gamma} = 5.71 \times 10^{-4} \tau^{-1} s^{-1}$ .

## REFERENCES

- [1]. Maier, A.G., et al., *Malaria parasite proteins that remodel the host erythrocyte*. Nat Rev Micro, 2009. 7(5): p. 341-354.
- [2]. Waller, K.L., et al., *Interactions of Plasmodium falciparum erythrocyte membrane protein 3 with the red blood cell membrane skeleton*. Biochimica et Biophysica Acta (BBA) - Biomembranes, 2007. 1768(9): p. 2145-2156.
- [3]. Glenister, F.K., et al., *Contribution of parasite proteins to altered mechanical properties of malaria-infected red blood cells*. 2002. p. 1060-1063.
- [4]. Yuan, H., et al., *One-particle-thick, solvent-free, coarse-grained model for biological and biomimetic fluid membranes*. Physical Review E. 82(1): p. 011905.
- [5]. Li, J., et al., *Cytoskeletal dynamics of human erythrocyte*, in PNAS. 2007. p. 4937-4942.

# POSTERS

# LITHIATION-INDUCED SELF-WEAKENING IN CARBONACEOUS NANO-ELECTRODES

*Hui Yang, Xu Huang, and Sulin Zhang*

Department of Engineering Science and Mechanics  
The Pennsylvania State University  
University Park, PA 16802

## ABSTRACT

We perform molecular dynamics simulations to elucidate lithiation induced fracture mechanisms of defective carbonaceous anode materials such as graphene and single-walled carbon nanotubes (SWCNTs). Our modeling results reveal that lithium diffusion toward the crack tip is both energetically and kinetically favored owing to the crack-tip stress gradient. The stress-driven lithium diffusion results in lithium aggregation around the crack tip, chemically weakening the crack-tip bond and at the same time causing stress relaxation. The chemical weakening effect is the dominant factor, which manifests a self-weakening mechanism. Moreover, the

variation of defect size and lithium concentration sets two distinct fracture modes of the SWCNTs upon uniaxial stretch: abrupt and retarded fracture. Abrupt fracture either involves spontaneous lithium weakening of the propagating crack tip or is absent of lithium participation, while retarded fracture features a “wait-and-go” crack extension process in which the crack tip periodically arrests and waits to be weakened by diffusing lithium before extension resumes. The atomistic understanding of the degradation mechanism provides guidance for the lifetime extension in the rational design of graphene/CNT-based electrodes.

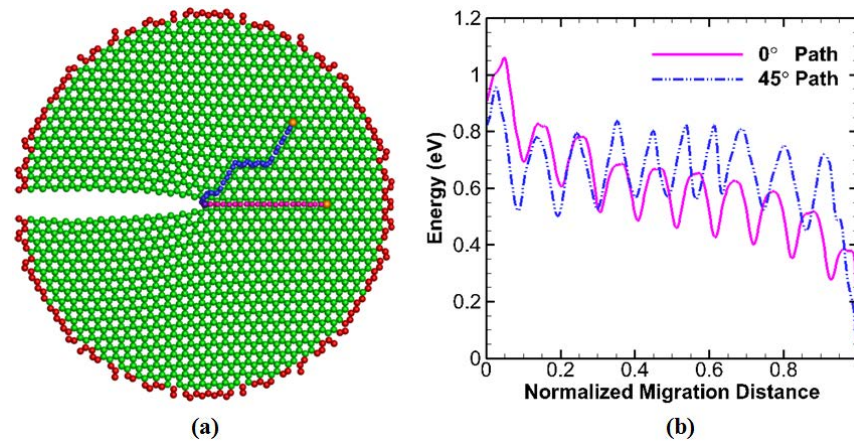


Figure 1. The mobility of the Li adatom. (a): The migration paths (minimum energy paths) for a Li adatom initially placed along (path indicated by a sequence of blue dots) and (path indicated by a sequence of pink dots) migrating toward the crack-tip hollow site; (b) The migration energy landscapes corresponding to the two migration paths.

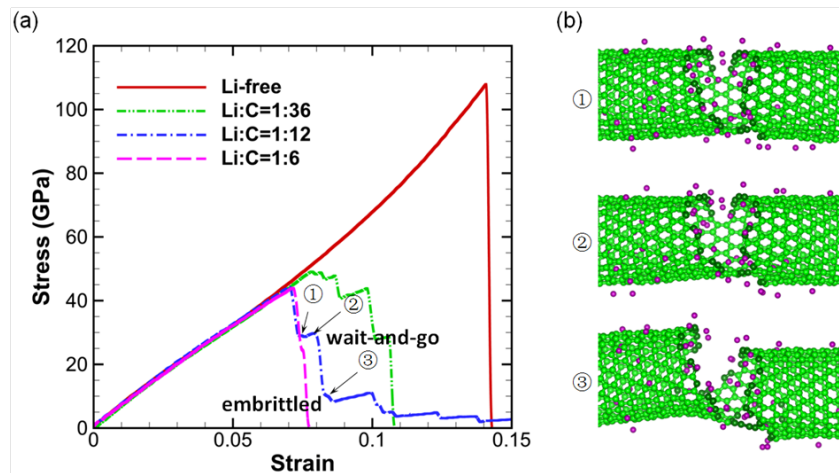


Figure 2. (a) Stress-strain curves of the SWCNTs containing a hole-like defect. (b) Three fractural states of SWCNTs showing a “wait-and-go” fracture behavior of SWCNTs with relatively low Li concentration (for Li:C = 1:12).

## References

- [1] [H. Yang](#), X. Huang, W. Liang, A.C.T. van Duin, M. Raju, S. Zhang, "Self-weakening in lithiated graphene electrodes", Chem. Phys. Lett., vol. 563, pp. 58-62, 2013.
- [2] X. Huang, [H. Yang](#), W. Liang, M. Raju, M. Terrones, V.H. Crespi, A.C.T. van Duin, S. Zhang, "Lithiation induced corrosive fracture in defective carbon nanotubes", Appl. Phys. Lett., vol. 103, pp. 153901-153904, 2013.
- [3] Y. Liu, H. Zheng, X. H. Liu, S. Huang, T. Zhu, J. Wang, A. Kushima, N. S. Hudak, X. Huang, S. Zhang, S. X. Mao, X. Qian, J. Li, J. Y. Huang, "Lithiation-Induced Embrittlement of Multiwalled Carbon Nanotubes", ACS Nano, vol. 5, pp. 7245-7253, 2011.

## GALVANIC FABRICATION OF BI-DIRECTIONAL SURFACES

Huihun Jung<sup>1</sup>, Yusuf Nur<sup>2</sup>, Kaan Kalkan<sup>3</sup>, Melik C. Demirel<sup>1</sup>

<sup>1</sup>Engineering Science and Mechanics Department, Penn State, PA-16802, USA

<sup>2</sup>Department of Chemistry, Mustafa Kemal University, Antakya, Turkey

<sup>3</sup>Functional Nanomaterials Laboratory, Oklahoma State University, Stillwater, OK-74078, USA

**Abstract:** Anisotropic surfaces offer a highly convenient way of controlling liquid transport by guiding droplets for directional wetting in smart microfluidic devices as well as diffuse reflective devices for solar cell applications. Materials anisotropy in these surfaces has been achieved by oriented rearrangement of micro/nanostructures on a surface. The array of techniques used to fabricate anisotropic surfaces can be categorized as rigid structures, stimuli-responsive structures, or adaptive structures. Numerous techniques for manufacturing rigid anisotropic surfaces have been developed, ranging from template and template-free deposition to photolithography to direct printing. Here, we demonstrated the fabrication and patterning of directional surfaces from doped silicon wafer by wet etching. In this talk, we will discuss the use of these surfaces as digital fluidic devices for applications in biomedical, optical and microfluidic fields.

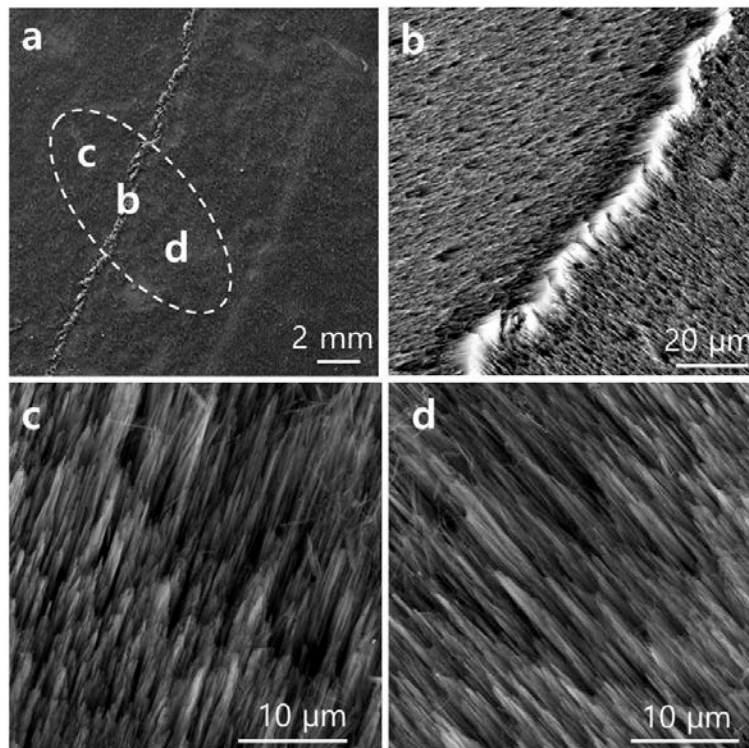


Figure 1. SEM images of bi-directional Silicon Nanowire (SiNW) substrates for a ratchet device. a. Broader SEM image of bi-directional SiNW substrate. b. Borderline of bi-directional SiNW. This white boundary between two different asymmetric SiNW surfaces is due to the formation of bundled nano-pillar. c and d. Zoomed images of bi-directional SiNW. To prevent bundling of SiNWs, we used critical point dryer after silicon nanowire etching.

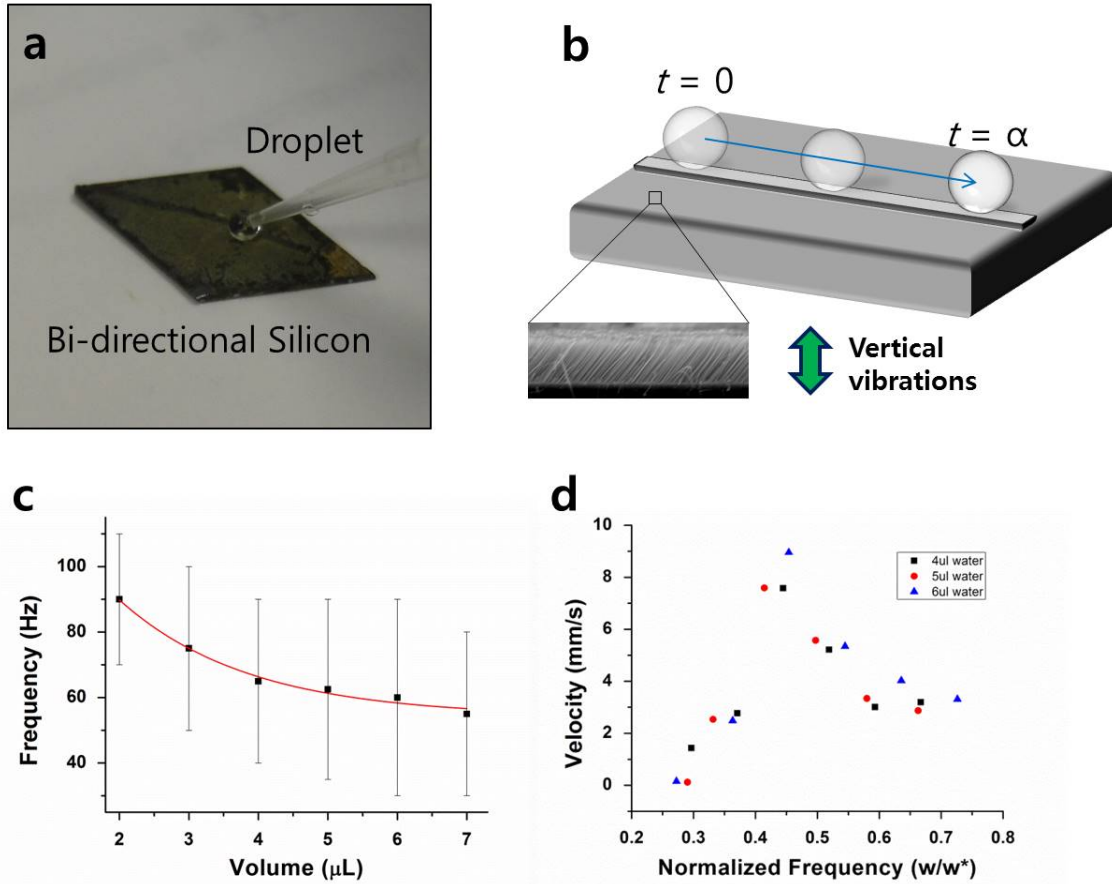


Figure 2 Droplet transportation with bi-directional SiNW surface. *a.* Real image of bi-directional surface. Because this surface has superhydrophobic characteristics, water droplet on the surface forms a spherical shape. *b.* A schematic diagram of a ratchet device. According to directionality of SiNW, the water droplet moves in one direction when we applied vertical vibration to the surface. *c.* Vibration frequency vs. water droplet volume graph. According to water droplet volume, vibration frequency range is different. *d.* velocity vs. normalized frequency data. Although water droplet volume is different, droplet velocity is a function of normalized frequency.

## REFERENCES

- [1] X. Li, P. W. Bohn, "Metal-assisted chemical etching in HF/H<sub>2</sub>O<sub>2</sub> produces porous silicon", *Appl. Phys. Lett.*, vol. 77, pp. 2572-2574, 2000.
- [2] K. Peng, A. Lu, R. Zhang, S. T. Lee, "Motility of Metal Nanoparticles in Silicon and Induced Anisotropic Silicon Etching", *Adv. Funct. Mater.*, vol. 18, pp. 3026-3035, 2008.
- [3] K. Sekeroglu, U. A. Gurkan, U. Demirci, M. C. Demirel, "Transport of a soft cargo on a nanoscale ratchet", *APPLIED PHYSICS LETTERS*, vol. 99, pp. 063703, 2011

## Microstructures of Ball Milled hBN-Ni Cold-Sprayed onto an Aluminum Substrate

Maryam Neshastehriz<sup>1</sup>, Ivi Smid<sup>1</sup>, Al Segall<sup>1</sup>, Tim Eden<sup>2</sup>, John Potter<sup>2</sup>

<sup>1</sup>Department of Engineering Science and Mechanics, Penn State University, University Park, Pennsylvania, 16802, USA

<sup>2</sup>Applied Research Laboratory, Penn State University, University Park, Pennsylvania, 16802, USA

Self-lubricating hBN-Ni particles, comprised of hexagonal-boron-nitride powder encapsulated in cubic nickel, have been developed for cold-spray coatings of lightweight aluminum 6061 components. By reduction of the coefficient of friction and better wear resistance, the component lifetime is extended, and the overall performance is improved. The hBN acts as the lubricant. The Ni encapsulant consists of several nanolayers, which were electroless-plated in aqueous solution in multiple steps, typically depositing 200-300 nm of nickel per step. The composite particles were milled with low and high energy equipment and cold sprayed onto aluminum substrates. The bond strength is related to the potential hardenability of the particles through plastic deformation; the reduction of hardenability is proportional to milling time and energy. De-agglomeration and mechanical alloying of the particles has been performed by low and high energy ball milling. The un-milled and milled particles and coated substrates were characterized through SEM, EDS, BET, optical microscopy, micro hardness and bond strength.

## REFERENCES

- [1] S. Yoon, J. Kim, G. Bae, B. Kim, C. Lee, Formation of coating and tribological behavior of kinetic sprayed Fe-based bulk metallic glass, *Journal of Alloys and Compounds*, 2011, 509, p 347-353
- [2] Y. Xiong, G. Bae, X. Xiong, C. Lee, The effect of successive impacts and cold welds on the deposition onset of cold spray coatings, *Journal of Thermal Spray Technology*, 2010, 19(3), p 575-585
- [3] P. King, G. Bae, S. Zahiri, M. Jahedi, C. Lee, An experimental and finite element study of cold spray copper impact onto two Aluminum substrates, *Journal of Thermal Spray Technology*, 2010, 19(3), p 620-634.
- [4] G. Bae, K. Kang, H. Na, J. Kim, C. Lee, Effect of particle size on the microstructure and properties of kinetic sprayed nickel coatings, *Surface and Coatings technology*, 2010, 204, p 3326-3335
- [5] A. Papyrin, V. Kosarev, S. Klinkov, A. Alkimov, V. Fomin, *Cold Spray Technology*, Elsevier, 2006.
- [6] S. Kumar, G. Bae, C. Lee, Deposition characteristics of copper particles on roughened substrates through kinetic spraying, *Applied Surface Science*, 2009, 255, p 3472-3479
- [7] I. Smid, A. E. Segall, P. Walia, G. Aggarwal, T. J. Eden, and J. K. Potter, Cold-Sprayed Ni-hBN Self-Lubricating Coatings, *Tribology Transactions*, 2012, 55, p 599-605
- [8] G. Bae, Y. Xiong, S. Kumar, K. Kang, C. Lee, General aspects of interface bonding in kinetic sprayed coatings", *Acta Materialia*, 2008, 56, p 48858-4868

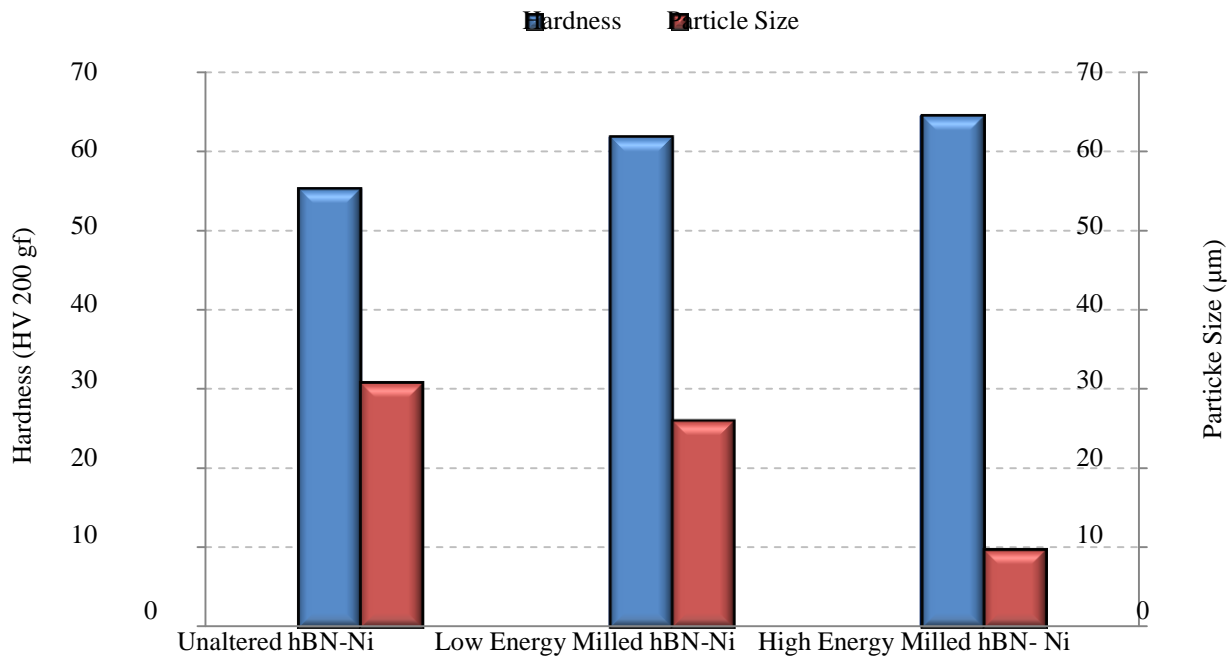


Figure 1: Average hardness and particle size for unaltered and milled hBN-Ni

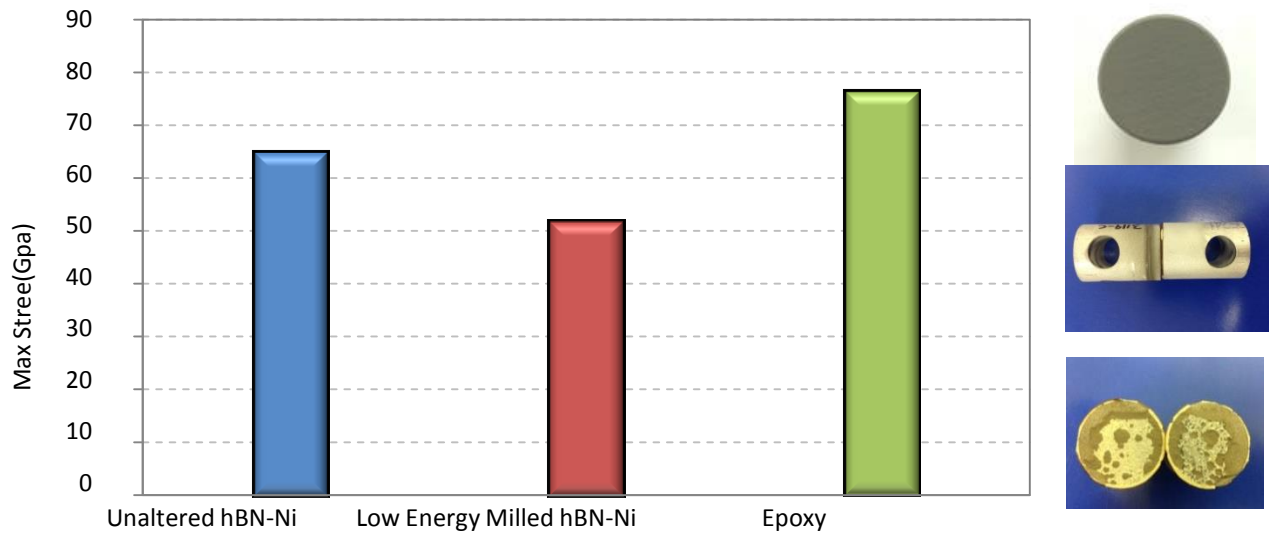


Figure 2: Average bond strength measurements taken for cold spray coatings

# ACOUSTOFLUIDIC MICROMIXER USING ACOUSTICALLY OSCILLATED SHARP-EDGES

Po-Hsun Huang,<sup>a</sup> Yuliang Xie,<sup>b</sup> Daniel Ahmed,<sup>a</sup> Nitesh Nama,<sup>a</sup> Yuchao Chen,<sup>a</sup>  
Chung Yu Chan,<sup>a</sup> Lin Wang,<sup>b</sup> and Tony Jun Huang<sup>a,b</sup>

<sup>a</sup>Department of Engineering Science and Mechanics, The Pennsylvania State University,  
University Park, Pennsylvania 16802, USA

<sup>b</sup>Department of Chemical Engineering, The Pennsylvania State University,  
University Park, Pennsylvania 16802, USA

<sup>c</sup>Ascent Bio-Nano Technologies Inc., State College, Pennsylvania 16802, USA

Rapid and homogeneous mixing is essential to a number of applications, such as chemical kinetic studies and nano-material synthesis [1-9]. In this work we present an acoustofluidic mixer based on the acoustic streaming effects [9] induced by oscillating sharp edges. Our method features advantages such as simple fabrication and operation, compact device, and excellent mixing performance.

Fig. 1 schematically shows the design of acoustofluidic mixer. Briefly, a single-layer PDMS channel with eight sharp edges on its sidewall was fabricated and bonded onto a glass slide, followed by attaching a piezoelectric transducer adjacent to it. Upon the actuation of the piezoelectric transducer, the sharp edges are acoustically oscillated to generate a pair of counter-rotating vortices around the tip of sharp edges, which significantly enhance the mass transport across the channel width by breaking the interface of laminar fluids.

To characterize the fluid flow pattern inside the channel due to the acoustic streaming, a solution containing dragon green fluorescent beads of 1.9  $\mu\text{m}$  in diameter was injected into the channel. In the absence of acoustic activation (the piezoelectric transducer is OFF), a laminar flow pattern of fluorescent beads was observed [Fig. 2(a)], whereas when the piezoelectric transducer is ON, oscillating sharp edges induced a strong acoustic streaming [Fig. 2(b)]. The streaming effects greatly enhanced the mass transport of two fluids by perturbing the bulk flow and breaking the interface of laminar flow, thereby enabling fast and homogeneous mixing.

When the piezoelectric transducer is OFF, a side-by-side laminar flow was observed due to the absence of acoustic waves [Fig. 3(a)]. When the piezoelectric transducer is ON, mixing was observed at different driving frequencies of the piezoelectric transducer [Figs. 3(b)-(d)]. Homogeneous mixing of DI water and fluorescein was achieved when the sharp edges was excited at the frequencies of 4.50 kHz and 4.75 kHz, while incomplete mixing was observed at the frequency of 4.25 kHz. To further verify the mixing performance, the cross-sectional dye concentration profiles [the dashed lines in Figs. 3(a)-(d)] at different frequencies were plotted by

measuring the gray scale value of the experimental images [Fig. 4]. The concentration profiles show that after the acoustic streaming phenomenon occurred, a uniform gray-scale value distribution across the width of channel was observed at the frequency of 4.50 kHz, suggesting that 4.50 kHz is a proper driving frequency for the piezoelectric transducer to develop the strongest acoustic streaming phenomenon. The mixing time was thus calculated to be around 180 ms. We believe that the mixing speed can be further improved with the optimization of the geometries of the sharp edges.

In conclusion, we demonstrate rapid and homogeneous mixing of fluids through the acoustic streaming phenomenon induced by oscillating sharp edges. The proposed mixer has a mixing time of 180 ms, and the advantages it offers are ease of fabrication, ease of operation, stable and fast mixing, making it an excellent candidate in a wide variety of microfluidic applications where fast and homogeneous mixing are required.

**FIGURES:**

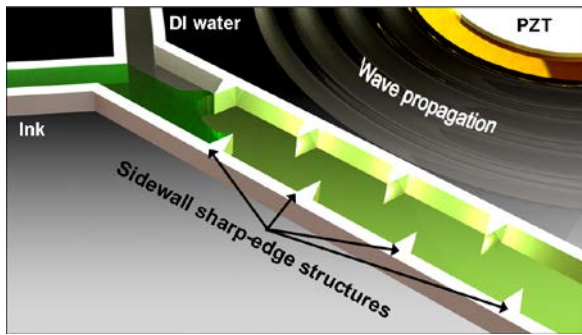


Figure 1: Schematic showing the design and working principle of sharp-edges based microfluidic mixer.

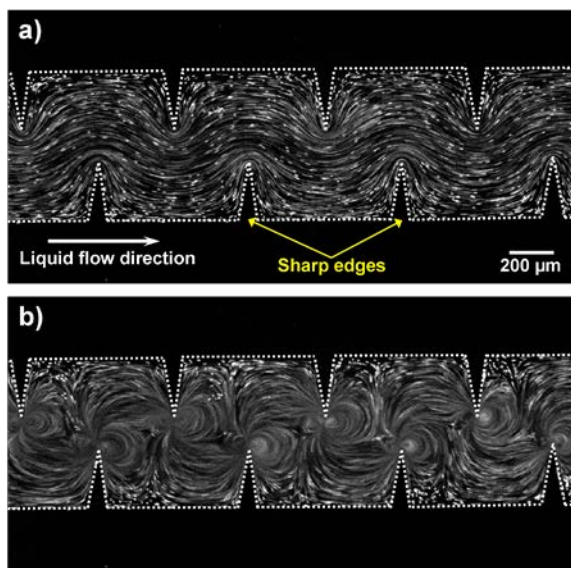


Figure 2: Characterization of the flow pattern with/without acoustic streaming. (a) In the absence of acoustic waves, laminar flow pattern was observed in a solution containing fluorescent beads. (b) In the presence of acoustic waves, acoustic streaming was developed in the liquid around the tips of shape edges.

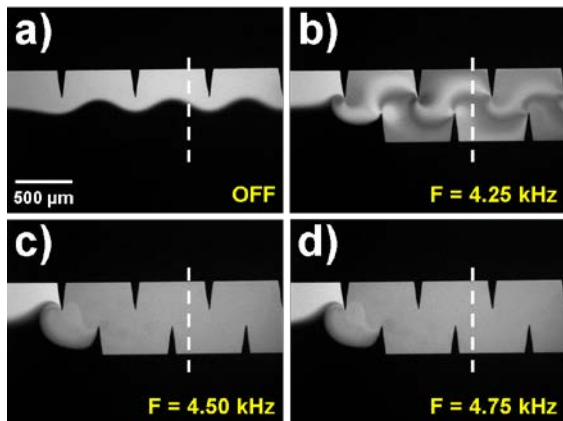


Figure 3: The experimental images showing when (a) PZT is OFF, (b) PZT is driven under a frequency of 4.25 kHz, (c) 4.50 kHz, and (d) 4.75 kHz.

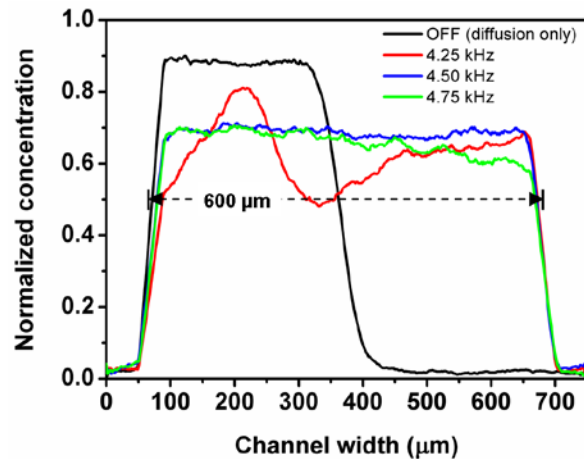


Figure 4: Plots of normalized fluorescent concentration across the width of channel.

**REFERENCES:**

1. L. Pollack, M. W. Tate, N. C. Darnton, J. B. Knight, S. M. Gruner, W. a Eaton, and R. H. Austin, Proc. Natl. Acad. Sci. U. S. A., vol. 96, no. 18, pp. 10115-10117 (1999).
2. J. DeMello and A. DeMello, Lab Chip, vol. 4, pp. 11N-15N (2004).
3. E. M. Miller and A. R. Wheeler, Anal. Bioanal. Chem., vol. 393, pp. 419-426 (2009).
4. X. Mao, B. K. Juluri, M. I. Lapsley, Z. S. Stratton, and T. J. Huang, Microfluid. Nanofluid., vol. 8, pp. 139-144 (2010).
5. H. Y. Park, X. Qiu, E. Rhoades, J. Korlach, L. W. Kwok, W. R. Zipfel, W. W. Webb, and L. Pollack, Anal. Chem., vol. 78, pp. 4465-4473 (2006).
6. X. Mao, S.-C. S. Lin, C. Dong, and T. J. Huang, Lab Chip, vol. 9, pp. 1583-1589. (2009).
7. T. Frommelt, M. Kostur, M. Wenzel-Schäfer, P. Talkner, P. Hänggi, and A. Wixforth, Phys. Rev. Lett., vol. 100, 034502. (2008)
8. D. Ahmed, X. Mao, B. K. Juluri, and T. J. Huang, Microfluid. Nanofluid., vol. 7, pp. 727-731 (2009).
9. P. Marmottant and S. Hilgenfeldt, Nature, vol. 423, pp. 153-156 (2003).

# THIN FILM DEPOSITION AND CHARACTERIZATION OF HIGH ENERGY DENSITY GLASS

Matthew J. Pyrz<sup>1</sup>, Betul Akkopru-Akgun<sup>2</sup>, Susan Trolrier-McKinstry<sup>2</sup> and Michael Lanagan<sup>1,2</sup>

<sup>1</sup> Engineering Science and Mechanics, Pennsylvania State University  
University Park, State College, Pa 16801

<sup>2</sup> Materials Science and Engineering Department, Pennsylvania State University  
University Park, State College, Pa 16801

Coated-glasses are known for having high dielectric breakdown strengths, indicating an innate ability to retain high energy levels without material failure. The primary objective of this research is to produce an encompassing evaluation of MnO-coated glass breakdown and its potential for use in self-healing applications. This investigation utilizes COMSOL Multiphysics finite element software, in conjunction with physical experimental procedures, to obtain a model capable of predicting the breakdown activity for this type of coated glass. A simplified, thermal simulation, shown in Figure 1, has been generated that predicts the temperature profile in a sample containing a centralized heat source to represent a crack in the glass. This model will be extended by incorporating additional physics modules, including electrostatics, electric currents, and joule heating.

Verification of this computational model will be accomplished with DC breakdown experiments. Preliminary work has been conducted with aluminum-coated glass in an effort to elucidate techniques that can be repeatedly applied to obtain precise quantitative descriptions of the breakdown process in MnO-coated glass. This procedure involves an insulating polymer, positioned between polypropylene and the coated-glass, with current input/output electrodes contacting the top and bottom of the system.

By positioning the system components in this fashion, a uniform charge distribution is produced prior to breakdown phenomena. Additionally, the current input/output locations are positioned at a significant distance from the breakdown region as to yield a measurable area. Breakdown areas for the aluminum-coated material were found to be on the order of 150 mm<sup>2</sup> at breakdown strengths of 10000 V.

Data gathered from these physical breakdown processes will be utilized to improve upon the predictive accuracy of the COMSOL model. A simulated breakdown event that can effectively reproduce the experimental results is highly valuable due to its ability to provide information about the material that is essentially immeasurable with traditional experimental procedures, such as the temperature distribution generated in the presence of an applied voltage. Therefore, the coupling of experimental data with a computer-generated model will provide a comprehensive assessment of the breakdown behavior in MnO-coated glass and can be used to identify potential uses as a self-healing material.

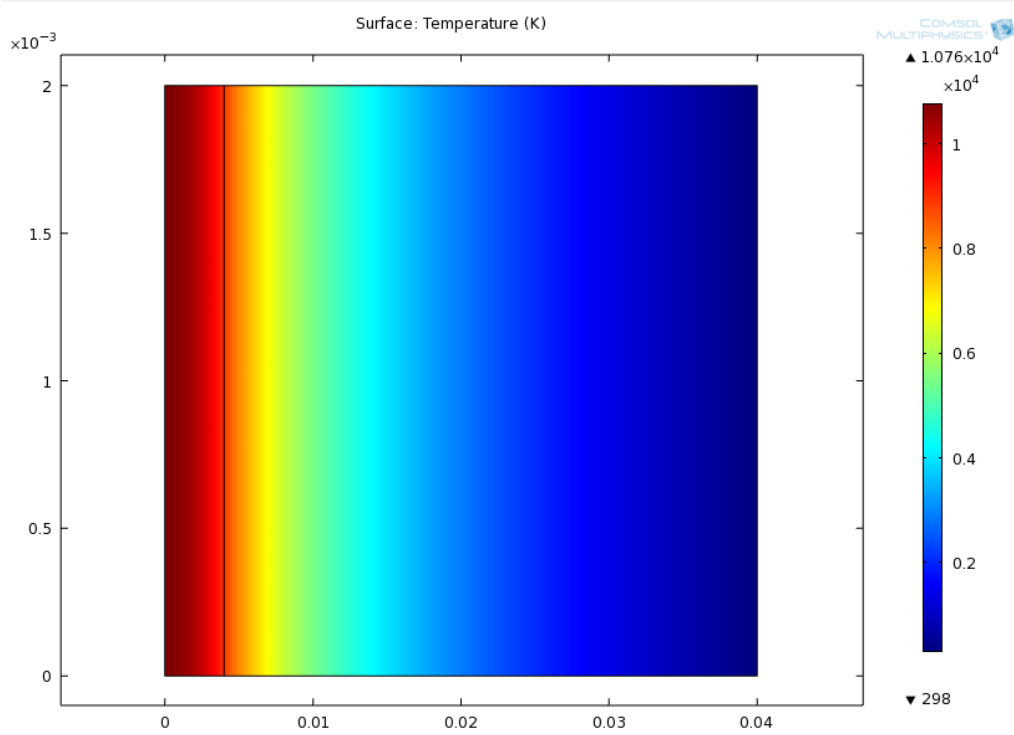


*Figure 1: Temperature distribution in thermal breakdown model.*

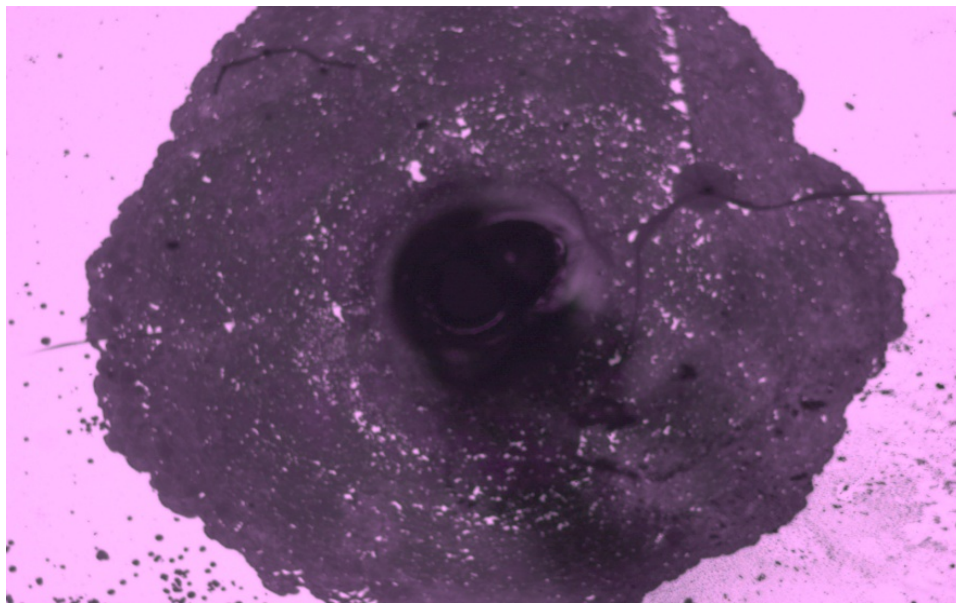


*Figure 2: Breakdown region of glass sample at 5x magnification through an optical microscope.*

# MATERIALS FABRICATION FROM SQUID RING TEETH PROTEINS

*Abdon Pena-Francesch<sup>1</sup>, Bulent Akgun<sup>2</sup>, Melik C. Demirel<sup>1,3\*</sup>*

<sup>1</sup> Materials Research Institute, and Department of Engineering Science and Mechanics, Pennsylvania State University, University Park, PA 16802, USA

<sup>2</sup> Center for Neutron Research, National Institute of Standards and Technology, Gaithersburg, MD 20899, USA and Department of Materials Science and Engineering, University of Maryland, College Park, MD 20742, USA

<sup>3</sup> Huck Institutes of Life Sciences, Pennsylvania State University, University Park, PA 16802, USA

There is an ongoing and unmet need to develop novel materials that can be produced easily from renewable resources, and which will offer a broad array of useful applications. Engineered eco-friendly, protein-based materials include various bioelastomers (*e.g.*, silk<sup>[1]</sup>), biomaterials (*e.g.*, protein scaffolds<sup>[2]</sup>) and modular biopolymers (*e.g.*, poly-peptides<sup>[3]</sup>) that provide similar or enhanced properties compared to synthetic alternatives. Squid ring teeth (SRT) is a thermoplastic protein-based material extracted from the tentacles of squid suction cups. This protein exhibits an unusual and reversible solid to melt phase transition, enabling it to be thermally shaped into 3D geometries such as fibers, colloids, and thin films. Due to this reversible transition, the SRT protein melt presents an underwater adhesive strength of 1.5 MPa, which is at least two orders of magnitude stronger than conventional synthetic adhesives and ten times the strength of other biological adhesives. Here, we show that SRT proteins have excellent mechanical and chemical properties in wet and dry conditions that exceed most natural and synthetic polymers, in addition to their unique capability of being thermally remodeled into multiple functional forms.

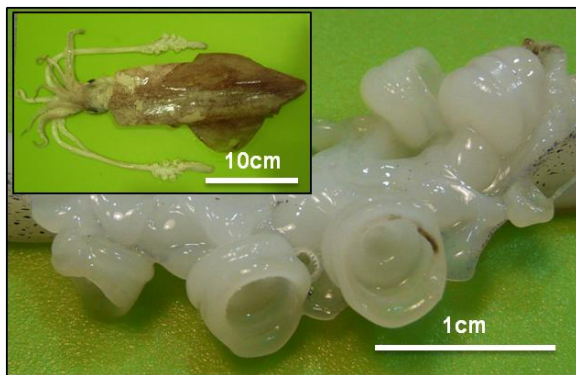


Figure 1 – European squid (*Loligo vulgaris*) and its suction cups in the tentacles, containing Squid Ring Teeth (SRT) <sup>[4]</sup>

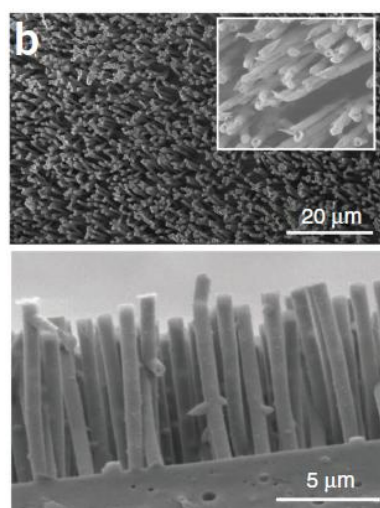


Figure 2 – Nanotubes of 800nm diameter fabricated from bulk SRT by nanowetting <sup>[5]</sup>

## REFERENCES

- [1] D. N. Rockwood, R. C. Preda, T. Yücel, X. Wang, M. L. Lovett, D. L. Kaplan, *Nature protocols* 2011, 6, 1612.
- [2] R. Langer, D. A. Tirrell, *Nature* 2004, 428, 487.
- [3] R. L. DiMarco, S. C. Heilshorn, *Advanced Materials* 2012, 24, 3923.
- [4] A. Pena-Francesch, B. Akgun, W. Zhu, H. Gao, M. C. Demirel, *Advanced Functional Materials* 2014, (submitted).
- [5] P. A. Guerette, S. Hoon, Y. Seow, M. Raida, A. Masic, F. Tian, M. C. Demirel, A. Pena-Francesch, S. Amini, G. Tay, A. Miserez, *Nature Biotechnology* 2013, 31, 908.

## IMMUNOLOGICAL ANALYSES OF WHOLE BLOOD VIA HIGH PRECISION “MICROFLUIDIC DRIFTING” BASED FLOW CYTOMETRY

*Ahmad Ahsan Nawaz, Ruth Helmus Nissly, Peng Li, Joseph Rufo, Yuchao Chen, Feng Guo, Sixing Li, Arooj Qureshi, Yanhui Zhao, Adem Ozcelik, and Tony Jun Huang.*

Engineering Science and Mechanics Department, Penn State, PA-16802, USA

Health care programs have been undergoing a transformation by decentralization of clinical labs since the inception of point-of-care (POC) diagnostics. Monitoring personal health via easy-to-operate, low cost and yet reliable diagnostics can play a vital role in improvement of global health care programs especially in resource poor settings. For example, the home blood glucose testing device has helped millions acquire accurate and fast information about the blood insulin needed to maintain healthy daily activities. However, most other hematological and immunological tests must be performed at clinical labs that are centralized due to expensive equipment and skilled operators required for their use. Furthermore, two often neglected complications of hematological and immunological tests are the conditions of transport and time required to deliver the sample to the laboratory, which can significantly alter the credibility of the results. Even in otherwise straightforward medical circumstances, wrong and inaccurate results can be fatal. Hence, development of reliable POC diagnostics is essential for fast and efficient results.

For immunological and hematological based diagnostics, flow cytometry is an established and reliable tool. One popular application is CD4+ cell counting from whole blood of human immunodeficiency virus (HIV)-infected patients, which is extremely important for determining the appropriate prescription of antiretroviral therapy to combat this infectious disease. Screening tumor biopsies, immunophenotyping and DNA content analysis are additional applications where flow cytometry is used in cancer diagnostics.

Despite the fact that flow cytometry is a well-accepted tool, its potential and utility is limited to large centralized institutions due to its many specialized requirements. A bulky footprint, high equipment cost, and requirement for highly skilled personnel for operation and maintenance significantly diminish the conventional flow cytometer's utility as a POC device. Production of large amounts of biohazardous material is often a byproduct of conventional flow cytometry, putting operators and the environment at risk of infection or contamination. In resource-poor settings, unstable electricity and limited availability of clean water pose other hindrances that demand a portable cytometer that uses low battery power, consumes little liquid and produces minimal waste.

Here, we report a novel microfluidic flow cytometry device that uses the 180° channel design and uses just one inlet for sheath fluid, has one inlet for sample injection, and can measure three parameters simultaneously with an on-chip integrated optical fiber based illumination and detection system. We performed an in-depth comparison of a novel 3-parameter (forward scatter (FSC), side scatter (SSC) and fluorescent (FL) emission) integrated microfluidic drifting based flow cytometer with a conventional machine (Beckman Coulter FC500). Our presented device utilizes 550  $\mu\text{l}/\text{min}$  of sheath fluid via one inlet and 15  $\mu\text{l}/\text{min}$  of sample fluid via a second inlet. We calibrated our device for FSC, SSC and FL detection using the commercial standard 10  $\mu\text{m}$  Flow-Check calibration beads. Subjection to a stringent 8-peak rainbow calibration bead test demonstrated the ability of our flow cytometer to differentiate fluorescent signals of eight intensities, an important test for reliable immunological based cytology studies. Next, cell count comparison with a hemocytometer was performed. Finally, we performed immunological analysis on human blood from a healthy donor and compared the results to a commercial flow cytometer for CD4+ lymphocyte cell count. Our results showed good agreement with the results from a commercial flow cytometer and within acceptable range, suggesting that this device may be useful as a POC diagnostic microfluidic flow cytometer.

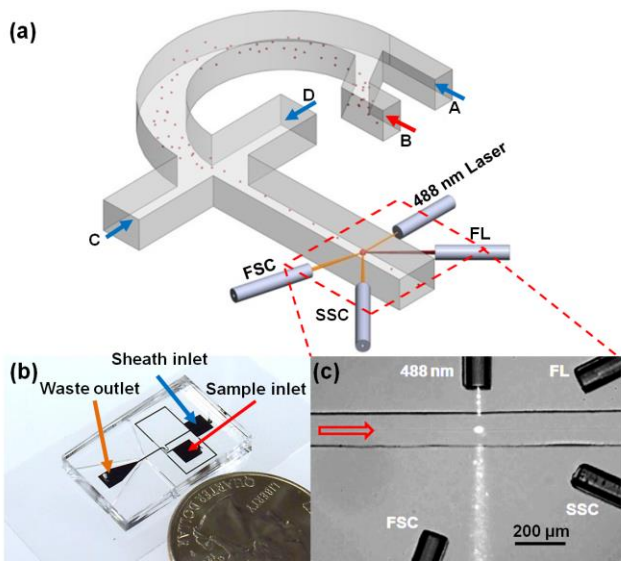


Figure 1: Microfluidic drifting based flow cytometry device. (a) Schematic of the device indicating the 180° curved region that results in cells/particle focusing and the detection region of the device depicted with input fiber for 488 nm laser and three (forward, side and fluorescence) detection fibers. A C and D are sheath fluid entry points while B represents the sample inlet. The cells/particles focus in the middle vertical plane as they move around the curved channel. The vertically focused cells/particles are then squeezed into a single stream of particles. (b) Small footprint of the device in comparison to US quarter. The device includes a single inlet for the sheath fluid and a single inlet for sample fluid. (c) Bright field microscope image of the cells/particle interrogation region (rectangular region in (a)). Shown is an instant when laser light illuminates a fluorescent 10 µm polystyrene bead as it passes through.

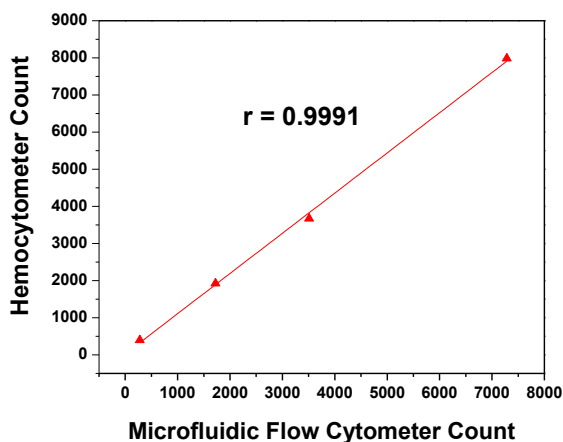


Figure 2 PS bead counts at different dilutions using the microfluidic flow cytometer compared with a hemocytometer. Correlation of  $r = 0.9991$  indicates good congruency between the count values from hemocytometer and microfluidic flow cytometer.

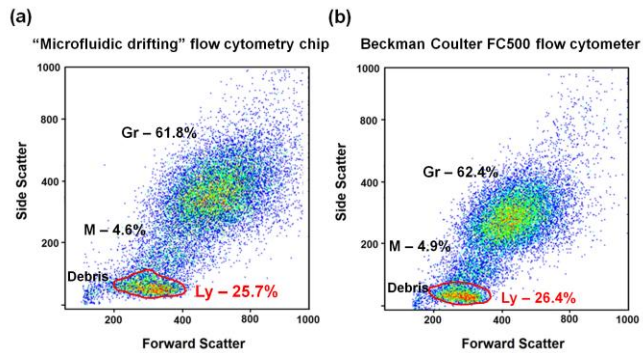


Figure 3: Comparison of forward scatter vs. side scatter plot of lysed whole blood from the microfluidic flow cytometer (a) vs. a commercial Beckman Coulter FC500 flow cytometer (b). Each dot indicates a single cell. Percentages of different subpopulations such as Granulocytes (Gr), Monocytes (M), Lymphocytes (Ly, red outlined region indicative of general location of these cells), were obtained via the autogating function of FlowJo software.

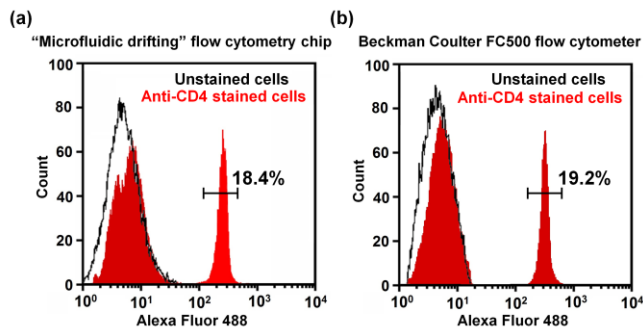


Figure 4: Comparison of Alexa Fluor 488-labeled anti-CD4 stained whole blood on the microfluidic flow cytometer (a) and a commercial Beckman Coulter FC500 flow cytometer (b). The black curve represents an unstained control sample of the blood and the colored curves represent the stained sample. Before fluorescence analysis, cells were gated on lymphocytes, as shown in Figure 6, to exclude monocytes, which also express CD4.

## REFERENCES:

- [1] Gottwald, E., B. Lahni, G. Lüdke, T. Preckel, and C. Buhlmann. Intracellular HSP72 detection in HL60 cells using a flow cytometry system based on microfluidic analysis. *Biotechniques* 35:358–62, 364, 366–7, 2003.
- [2] Jayat, C., and M. H. Ratinaud. Cell cycle analysis by flow cytometry: principles and applications. *Biol. Cell* 78:15–25, 1993.
- [3] Morris, K. Mobile phones connecting efforts to tackle infectious disease. *Lancet Infect. Dis.* 9:274, 2009.
- [4] Laerum, Ole Didrik and Bjerknes, R. *Flow Cytometry in Hematology*. Academic Press, 1992.

## **RED BLOOD CELL AND PLATELET COUNT OF NEWBORNS VIA MICROFLUIDIC DRIFTING FLOW CYTOMETRY**

*Ahmad Ahsan Nawaz, Ruth Helmus Nissly, Peng Li, Joseph Rufo, Yuchao Chen, Arooj Qureshi, Yanhui Zhao, Adem Ozcelik, and Tony Jun Huang.*

Engineering Science and Mechanics Department, Penn State, PA-16802, USA

Newborn babies are at higher risk of many infectious diseases than adults. Jaundice, sepsis, sickle cell disease are some of such conditions, which if unchecked can become life-threatening. A complete blood count, the most important and most common test that evaluates the condition of three main blood cell types i.e. red blood cells, white blood cells and platelets. For neonates this test must be conducted within 12 hours of birth for immediate evaluation of the health. However, the amount of blood that a newborn has depends on their weight. At birth a baby has approximately 76.6 ml of blood which increases to 83.3 ml in twenty-four hours. Complete blood count of neonates, hence cannot be done in a regular way by drawing 10 ml of blood (as in adults who have approximately 5-7 liters of blood) which is > 10% of complete blood volume and could be life threatening.

Flow cytometers and hematology analyzers are the gold standards for complete blood count. Although, significant efforts are being extended, these units still require blood amount (1 ml to 5 ml) which is not suitable for newborns. Tests, however have to be delayed thus also delaying the treatment in case of any deficiency in the newborn.

Here we have demonstrated a microfluidic drifting based flow cytometry device that utilizes just 5  $\mu$ l of blood for counting of red blood cells and platelets. Our microfluidic drifting based flow cytometer measures four parameters (forward scatter, side scatter, 525 nm emission signals, 575 nm emission signals) simultaneously via on-chip integrated optical fiber detection system. For red blood cells the forward scatter optical fiber at 3° to the incident laser light (488nm) measures the size of the cells while side scatter detects the refractive index of the cells.

For this purpose, fresh venous blood was taken from a healthy donor. Within 17 hours of drawing, we fixed the whole blood within 1 ml of 4% paraformaldehyde in PBS (Santa Cruz Biotechnology, Inc.) and incubated at room temperature for 10 min. Next, 5  $\mu$ l of CD41 monoclonal anti-human antibody was added to the blood which attaches to the platelets. This was followed by addition of 5  $\mu$ l of another PAC-1 antibody which is expressed by activated platelets only.

Here, Fig 1 indicates the red blood cells are focused via a microfluidic drifting flow cytometry in the middle of the main channel. The laser light illuminates the cells. The light scattered from the cells are detected via forward scatter. The emission signals from the antibodies are detected by the 525 nm and 575 nm detector fibers.

Preliminary results of red blood cell counting in terms of forward scatter vs side scatter of the whole blood are shown in Fig. 2

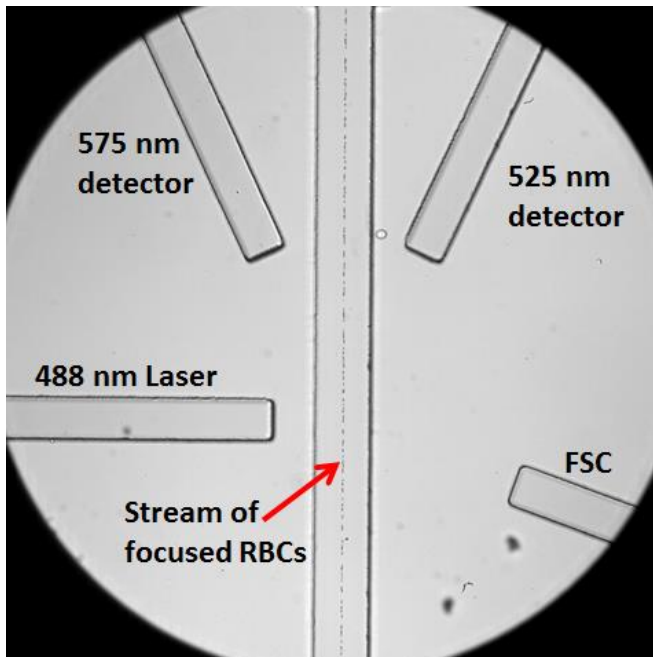


Figure 1: Red blood cells focused in the middle of channel. The 488 nm blue laser is illuminated onto the red blood cells. The scatter signal is detected by FSC detection fiber, the fluorescent emission signals are detected by 525 nm and 575 nm detection fibers.

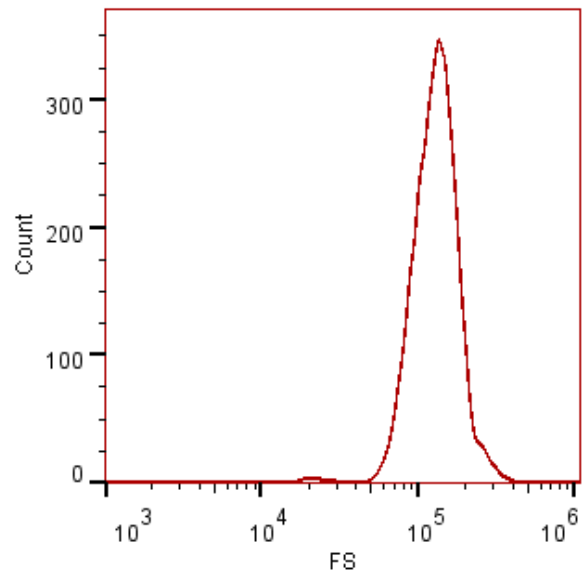


Figure 3: The histogram indicates the red blood cells as a single population.

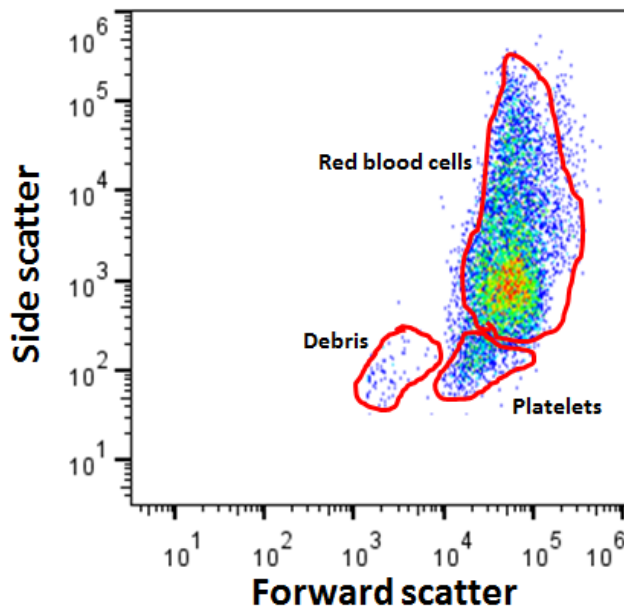


Figure 2 Forward scatter vs side scatter plot of human whole blood. Each dot is generated as a result of a cell passing the laser interrogation region. The plot indicated the red blood cells and platelets.

#### REFERENCES:

- [1] Hasan R, Inoue S, Banerjee A. Higher white blood cell counts and band forms in newborns delivered vaginally compared with those delivered by cesarean section. *Am J Clin Pathol.* 1993;100(2):116–118
- [2] Adair CE, Kowalsky L, Quon H, et al. Risk factors for early-onset group B streptococcal disease in neonates: a population-based case-control study. *CMAJ.* 2003;169(3): 198–203

# Shape and Stiffness-Changing Structures based on Fluidic Flexible Matrix Composites (F<sup>2</sup>MCs)

*Aniruddh Vashisth and Charles E. Bakis*

Department of Engineering Science and Mechanics, The Pennsylvania State University,  
University Park - 16802, PA, USA

Inspired by the fibrillar networks in plant cell walls, a highly mechanical advantageous actuator system is made from composite tube consisting of a flexible matrix and multiple layers of oriented high performance fibers. These fiber reinforced elastomers are known as Flexible matrix composites (FMCs). A significant change in stiffness and shape could be obtained by using a valve control for pressuring FMC tubes with a nearly incompressible fluid. A fluid with a high bulk modulus resists volume change that would normally occur with an open valve. So, by closing the valve, the tube becomes much stiffer than in the open valve case. By varying the fiber angle and matrix material of these tubes a wide range of stiffness ratios can be obtained. Therefore, by varying the internal pressure, the tube behaves like an actuator. Such composites are termed as fluidic flexible matrix composites (F<sup>2</sup>MCs). These materials

are stiff in one direction yet compliant in others. The F<sup>2</sup>MC tubes (2 mm diameter) in this investigation have three layers, with neat polyurethane for the inner and outer layers and stainless steel reinforced polyurethane for the middle layer. Multiple small F<sup>2</sup>MC tubes are embedded in potting matrix, to make laminated skins and analyze them. Multi-layered laminates with F<sup>2</sup>MC tubes embedded multi-directionally could display actuation and variable stiffness by pressurizing different layers. Such composites could be used as structural elements for morphing and variable stiffness structures. Over the long term, this line of research is aimed at the development of thin skins for structures that can change shape and stiffness differently as a function of direction. Future application would include synthetic arms for robots, morphing wings for aircrafts etc.

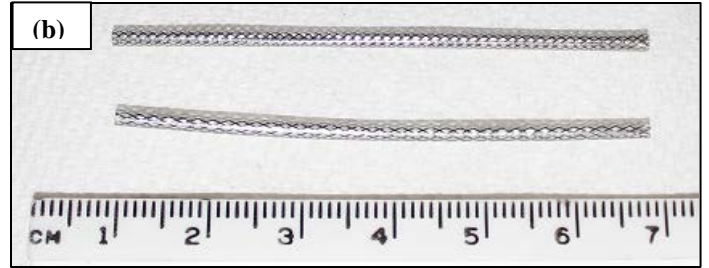
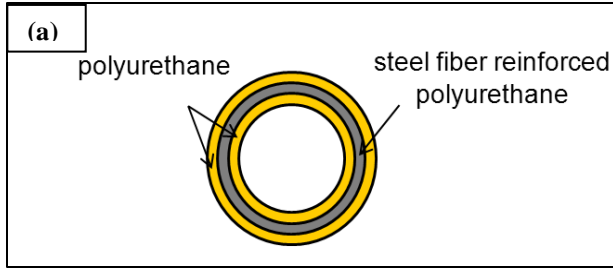


Figure1. (a) Three layered polyurethane  $F^2MC$  tube (b) Photographs of steel reinforced, braided FMC tubes along with cm scale

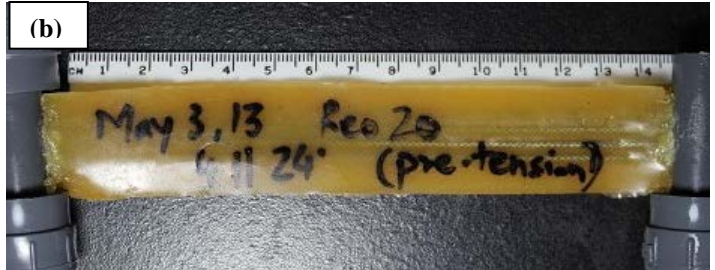
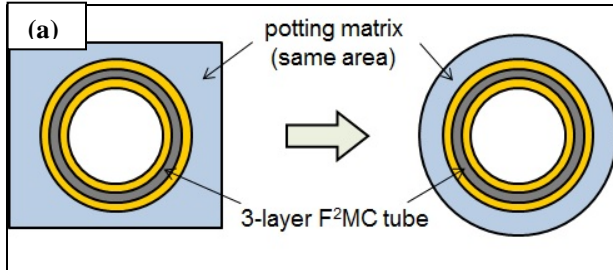


Figure2. (a) We assume that the  $F^2MC$  tubes are arranged side-by-side in a rectangular array and then potted in the resin, resulting in a cross section of a unit cell as shown in Figure a. (b) Photograph of cured laminate along with cm scale

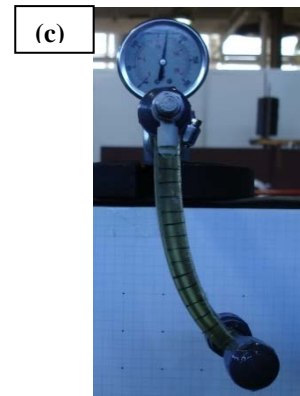
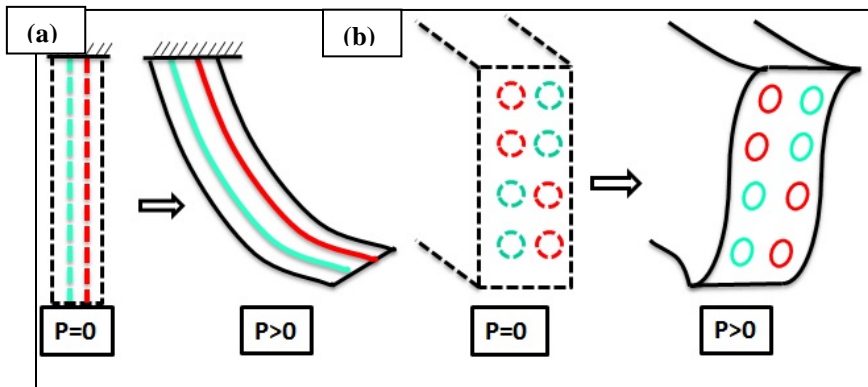


Figure3. (a) Warping and (b) twisting actuation of multi-layered laminate upon pressurization. Red and blue lines show  $F^2MC$  tubes with different fiber orientation. (c) Photograph of warping in laminate at 170 psi fluid pressure.

**Reference:**

Vashisth, A., Zhu, B., Wimmer, B. M., Bakis, C. E., and Rahn, C. D., "Evaluation of Millimeter-Size Fluidic Flexible Matrix Composite Tubes" *Proc. ASME Conf. on Smart Materials, Adaptive Structures and Intelligent Systems, SMASIS2013*, Snowbird, Utah.

# VALIDATION AND VERIFICATION OF AN OVERSET FLUID-STRUCTURE INTERACTION SOLVER

*C. W. Elsworth, J. S. Pitt, S. T. Miller*

Engineering Science and Mechanics Department, Penn State, PA-16802, USA

For many years, classical mechanics sub-disciplines have been studied independently, but recent advancements in computational power and parallelism have brought about the emergence of research into coupled systems. A coupled system, in general, consists of two or more physically or computationally dissimilar domains, which are constrained to each other such that they interact dynamically [1]. These domains are often very different, requiring a solution that combines the traditionally independent mechanics sub-disciplines. One such coupled system of significant interest is Fluid-Structure Interaction (FSI), which sits at the intersection of solid mechanics and fluid mechanics [2].

Fluid-Structure Interaction consists of a solid immersed in, and/or containing a fluid, with coupling arising from the interplay between the fluid and solid domains. The deformation of the solid is a direct product of applied fluid stresses, while the deformation of the solid modifies the boundary conditions of the fluid domain. Computationally, this requires two-way coupling between the equations governing the fluid and the equations of motion describing the solid. Examples of FSI are prevalent in the natural world, therefore it is important to be able to understand the fundamental mechanisms behind these interactions as well as modeling them accurately. One of the most famous examples of FSI is the catastrophic failure of the Tacoma Narrows Bridge, where the self-induced oscillations matched the resonant frequency of the bridge, leading to its collapse [3].

While instances of FSI are prevalent, their computational modeling presents a variety of complications. Notably, concerns with the meshing of the domain and maintaining mesh quality during a simulation limit the types of problems that can be currently solved. For this reason, research into alternative methods is necessary to tackle more complex problems. Overset methods provide the ability to describe a complex computational domain through the decomposition of the domain into multiple independent meshes. The meshes are linked through interpolation between the overlapping regions of the meshes, and results in a complete representation of the domain. These methods allow for the prominent features of the domain to be meshed separately, simplifying meshing. In addition, they have also been demonstrated to be useful in the description of complex domains, and allow for the maintenance of mesh quality during dynamic simulations. These factors suggest that overset methods have the ability to address some of the complications experienced in realistic FSI simulations.

This talk will investigate a novel solver, which applies overset methods for the solution of computational FSI problems. The overset FSI solver implements Suggar++/DiRTlib overset methods into a partitioned FSI code. Partitioned FSI algorithms implement separate solvers for the coupled domains and iterate between them to ensure tight coupling. Figure 1 illustrates the process of a partitioned algorithm using fixed-point iterations and Aitkin under-relaxation. The ARL/PSU FSI solver is based on an OpenFOAM fluid solver and in-house structural solver, coupled by an interface class, providing a fully-coupled FSI solution [4]. The combination of two previously implemented solvers for overset and FSI processing provides a new approach to computational FSI modeling.

An overview of the partitioned solver's governing equations is presented, providing a foundation for the solution methods implemented in the overset FSI solver. Solver components are characterized and the overset FSI solver workflow is presented. Numerical validation data is provided through comparison to the Turek and Hron benchmark test case, as seen in Figure 2. Overset FSI solver benefits will be investigated, with respect to mesh generation and quality. These results will confirm that the overset FSI solver is able to address the mesh motion concerns of large deformation FSI simulations, while producing accurate results, and therefore add significantly to current computational FSI research, as demonstrated in Figure 3.

Rigorous code verification of this overset-grid enabled FSI algorithm is also presented and discussed. A collection of best practices for verifying partitioned FSI codes are also presented. Specifically, the method of manufactured solutions (see, e.g., [5]) is used to determine the order of accuracy of the code, including convergence rates and error magnitudes. The partitioned FSI algorithm introduces separate discretization schemes for the solid, fluid, and mesh motion components, requiring special care in the definition of a comprehensive verification exercise. Additionally, the sources of discretization error from each component of the solver must be combined into a single metric to determine global convergence rates.

Our strategy is to first verify each solver component independently, then reduce the verification exercise to one in which a global parameter is adjusted. This global parameter must be defined in order to capture the relative sources of error across the domain and motivates an optimal mesh refinement ratio between the fluid and solid domains. The error between exact and computed solutions can therefore be

calculated over the entire fluid-structure domain, as well as the individual fluid and solid components. For example, the mesh size of the fluid domain can be chosen as the primary parameter of error characterization, and the subsequent adjustment of solid mesh and time step size produces a solution that is globally of the same order of accuracy.

Special attention is given where overset grids are present, as the interpolation involved can significantly impact solution quality. Presented results include error magnitudes, convergence rates, and methodologies for a coherent approach to employing the method of manufactured solutions to partitioned FSI codes.

## REFERENCES

- [1] C. A. Felippa, K. Park, and C. Farhat. Partitioned Analysis of Coupled Mechanical Systems. *Computer Methods in Applied Mechanics and Engineering*, 190(24-25):3247–3270, 2001.
- [2] X. Wang. *Fundamentals of Fluid-Solid Interactions*, volume 8 of *Monograph Series on Nonlinear Science and Complexity*. Elsevier, 2008.
- [3] R. Loehner, J. R. Cebal, C. Yang, J. D. B. and Eric L. Mestreau, and O. Soto. Extending the Range and Applicability of the Loose Coupling Approach for FSI Simulations. In H.-J. Bungartz and M. Schafer, editors, *Fluid-Structure Interaction: Modelling, Simulation, Optimisation*. Springer-Verlag New York, LLC, 2006.
- [4] S. Miller, R.L. Campbell, C.W. Elsworth, J.S. Pitt, D.A. Boger. An Overset Grid Method for Fluid-Structure Interaction. *International Journal for Numerical Methods in Fluids*. Submitted October 28, 2013.
- [5] P. J. Roache. *Verification and Validation in Computational Science and Engineering*. Hermosa Publishers. Albuquerque, NM, 1998.

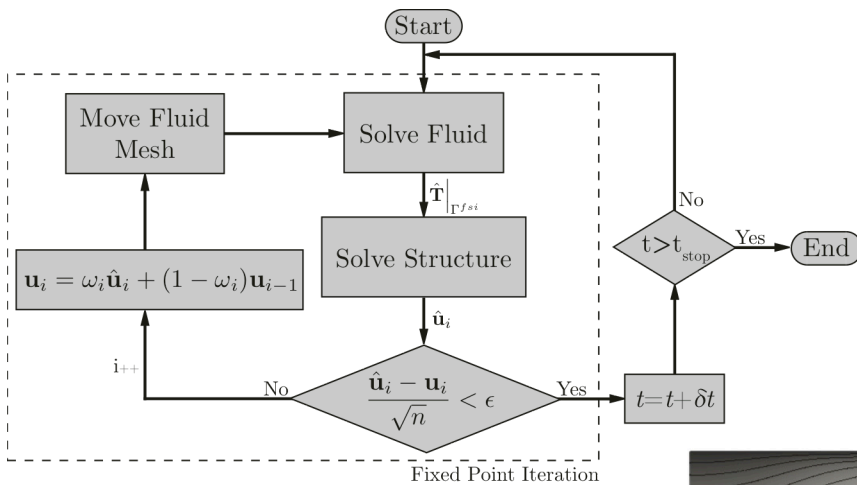


Figure 1: Detailed flowchart of partitioned FSI algorithm.

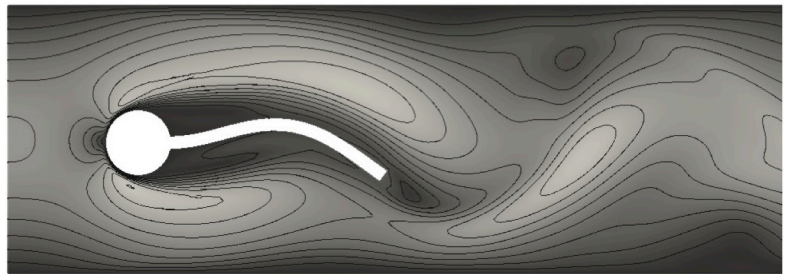


Figure 2: Simulation of the Turek-Hron benchmark case. Shaded by pressure.

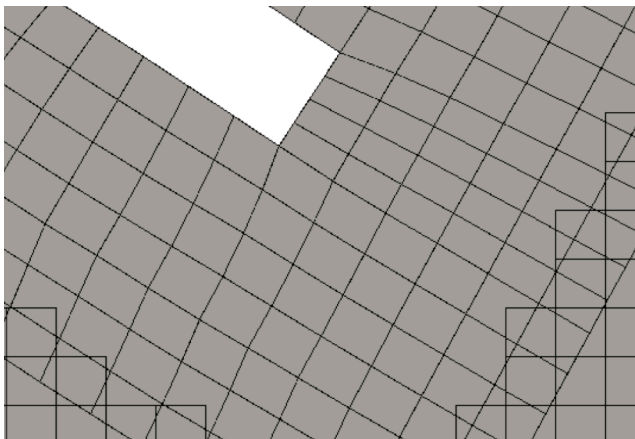


Figure 3: Detail of body-fitted mesh quality at the interface.

# SPATIAL CONTROL OF CELL INTERACTION WITH SURFACE ACOUSTIC WAVES

*F. Guo, P. Li and T. J. Huang*

Engineering Science and Mechanics Department, Penn State, PA-16802, USA

Cell-cell interaction or communication allows the coordination of cell functions, which critically regulates complicated physiological and pathological processes as embryogenesis, development of degenerative and autoimmune diseases.[1] The cells can talk with each other via directly cell-cell contact or signaling molecules in the real in vivo condition. Those complicated biological events highly rely on the spatial configuration of cells and regulation of chemical environment. The conventional cell culture approaches such as cell culture plate or petri dish suffer from the random cell distribution and uncontrollable chemical environment. [2] Better spatial and temporal control of cell assembly will facilitate the discovery of information which is often omitted in conventional in vitro studies. However, current methods of controlling cell assembly are lack of biocompatibility, flexibility, precision or throughput. Here we present a versatile tool, a tunable acoustic well, to control the spatial arrangement of cells for intercellular communication study based on surface acoustic wave technology. We demonstrated the system is able to control intercellular distance precisely, assemble cells with tunable geometry. For each critical functions of the acoustic well, we demonstrated the functional gap junction based intercellular communication by visualizing the transfer of fluorescent dyes.

In this study, we utilized the superposition of two orthogonal SSAWs, instead of previously reported inference patterns, to form dot-array configuration of pressure nodes. By depositing orthogonal digital transducers (IDTs) pairs on lithium niobate (LiNbO<sub>3</sub>) piezoelectric substrate. The generation of two overlapping orthogonal SSAWs relies on the excitation of difference resonance frequencies for different IDT pairs.[3] Figure 1 shows the schematic and actual setup of the device, respectively. Each pair of IDTs is independently connected to a radiofrequency (RF) signal to generate SAWs to apply different frequencies. Once the input signals are applied, square shape pressure nodes dot-arrays will form on substrate. Those SSAWs leak and establish a differential acoustic potential field to the adjacent fluid medium; this three dimensional field above each two dimensional square pressure node will work as “an acoustic well”.

To precise control the distance between two cells, the movement of cells must be stopped as soon as the withdrawal of the acoustic field. We applied a continuous RF signal to IDT along vertical direction and a modulated RF signal to the IDTs along horizontal direction to push cells towards each

other as 20  $\mu\text{m}$ , 10  $\mu\text{m}$ , 5  $\mu\text{m}$ , or 0  $\mu\text{m}$  (Figure. 2a). The modulated signal was set to a pulse signal with 500 ms duration and 2 s intervals. The whole process was recorded and analyzed as shown in Figure. 2b. The movement curve of step-like shape matched with the period of the modulated input signal. The movement of cells is fully controlled in suspension by regulating the input signals. We examined this method with gap junction based intercellular communication, which requires direct contact between cells or diffusion of soluble factors dependent upon the distance between the cells sending and receiving the signals. Fig. 2c showed that Calcein AM fluorescence dye can be transferred to the contacted cell after one hour, indicating the formation of functional GJIC. No fluorescence transfer can be observed after the same period of time, if two cells are separated with a very small distance (Figure. 2d, 3  $\mu\text{m}$ ).

Other than control of intercellular distance, this acoustic well approach is also suitable to trap and assemble multiple cells to form cell clusters with different geometric configurations. By employing an acoustic well with different acoustic amplitudes, the cells assemblies with linear-shape, single layer or spherical shape can be formed accordingly (Figure. 3). Those cells or cell clusters can be levitated by the acoustic radiation force and acoustic streaming induced hydrodynamic force (Figure. 4a).[4] After 30 min of initial incubation, bright field and fluorescent images of suspended cell assemblies were recorded every 5 minutes. Vivid dye coupling from donor cells (stained with Calcein AM) to receiver cells can be observed in all the linear arrays with different cell number. As expected, the larger the cell numbers, the longer it takes to observe evident dye coupling to the terminal cells (Figure. 4b-d). If the cells are patterned to a linear array, their communications are achieved linearly. If cells are patterned to a cluster, their communication format will be changed as well. We tuned the acoustic well to assemble cells into a cluster and multiple cells can receive the signal simultaneously from the donor cell (Figure. 4e).

We demonstrated the acoustic well is capable of performing multiple tasks for intercellular communication studies, including the control of intercellular distance, flexible cell assembly and communication in suspension. This acoustic well approach can be further developed for many cell-cell interaction studies including immune-cancer interaction, tissue engineering and regenerative medicine.

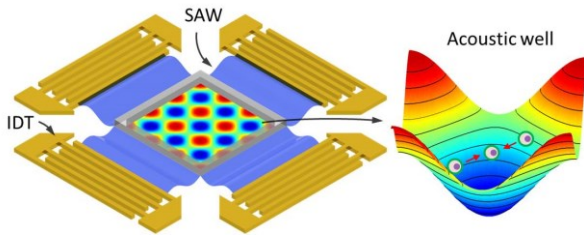


Figure 1: Schematic of “tunable acoustic well”: each pair of IDTs can generate a standing surface acoustic wave (SSAW) in one direction. The overlap of the two SSAWs can result in “well” shape configuration of pressure nodes arrays. Cells can be pushed into the middle of square pressure node.

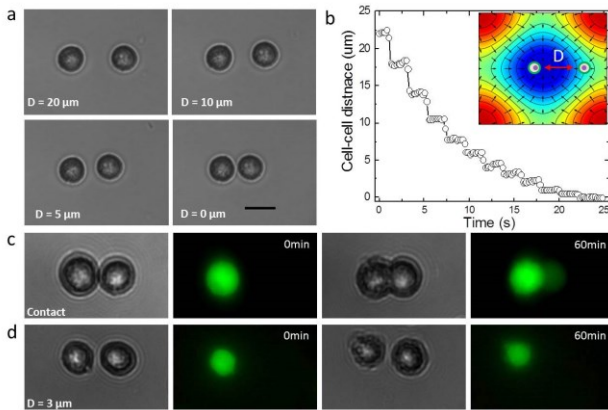


Figure 2: (a) Two HEK 293 T cells are positioned with varied intercellular distances, 20, 10, 5, 0  $\mu\text{m}$ , respectively. (b) The dependence of cell-cell distance on the input signals. (c) Two contacted HEK 293 T cells. Dye transfer can be observed after 60 min. (d) Two HEK 293 T cells were positioned with a distance of 3  $\mu\text{m}$ . Dye transfer between them cannot be observed after 60 min of culture.

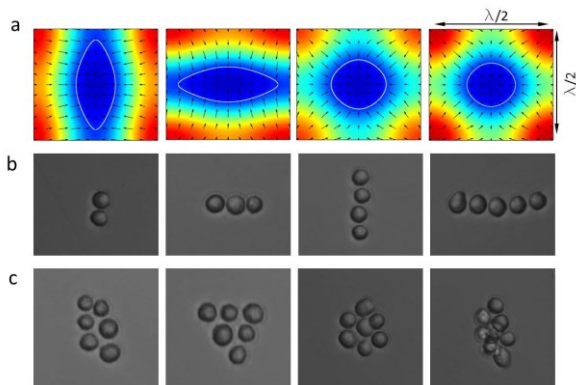


Figure 3: (a) Simulation results of acoustic potential distribution in an acoustic well with different acoustic amplitudes. (b) Linear shape of HeLa cell assemblies when applying linear shape of acoustic wells. (c) Single layer and spherical shape of cell assemblies when applying spherical shape of acoustic wells.

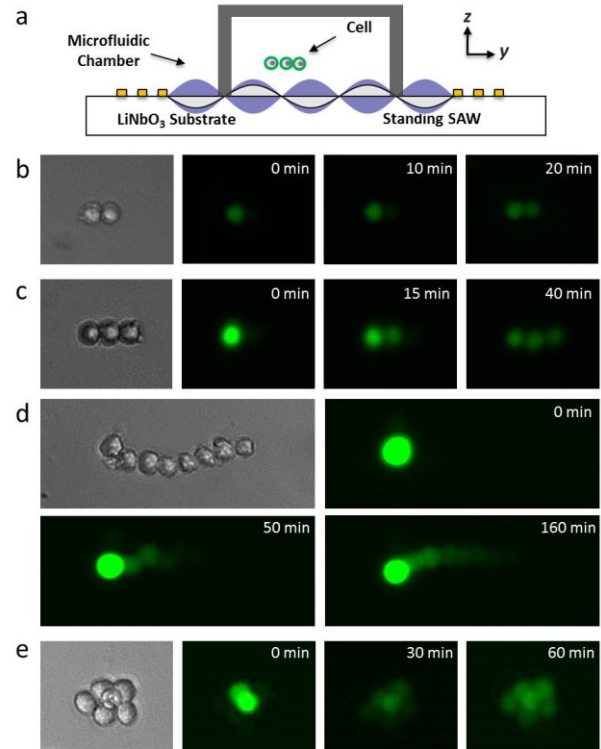


Figure 4: (a) Schematic of experimental setup. (b)-(e) Bright field image and time-lapse fluorescence images of two cells system trapped by an acoustic pressure node. Left cell was preloaded with Calcein-AM dye and dye transfer between different suspension cells assemblies can be observed over time.

## REFERENCES

- [1] C. H. Streuli, N. Bailey, and M. J. Bissell, “Control of mammary epithelial differentiation: basement membrane induces tissue-specific gene expression in the absence of cell-cell interaction and morphological polarity.,” *The Journal of cell biology*, vol. 115, pp. 1383-95, 1991.
- [2] F. Guo et al., “Probing cell-cell communication with microfluidic devices.,” *Lab on a chip*, vol. 13, pp. 3152-62, 2013.
- [3] X. Ding et al., “Surface acoustic wave microfluidics.,” *Lab on a chip*, vol. 13, pp. 3626-49, 2013.
- [4] J. Shi et al., “Three-dimensional continuous particle focusing in a microfluidic channel via standing surface acoustic waves (SSAW).,” *Lab on a chip*, vol. 11, pp. 2319-24, 2011.

# LITHIATION MECHANICS OF HIGH-CAPACITY ANODE MATERIALS

*Hui Yang and Sulin Zhang*

Department of Engineering Science and Mechanics  
The Pennsylvania State University  
University Park, PA 16802

## ABSTRACT

We present a chemo-mechanical model to investigate the lithiation-induced phase transformation, morphological evolution, stress generation and fracture in high-capacity anode materials such as silicon and germanium. The model couples lithium (Li) diffusion with elasto-plastic deformation in a three-dimensional (3D) setting. Several key features observed from recent transmission electron microscopy (TEM) studies are incorporated into the model, including the sharp interface between the lithiated shell and unlithiated core, crystallographic orientation-dependent reaction rate, and large-strain plasticity. Our simulation results demonstrate that the model faithfully predicts the anisotropic swelling of lithiated crystalline silicon nanowires (*c*-SiNWs) observed from previous experimental studies. Stress analysis reveals that lithiation anisotropy in *c*-SiNWs can lead to surface fracture at the angular sites where two adjacent {110} facets

intersect, consistent with previous experimental observations. However, as germanium and amorphous silicon nanostructures show weak lithiation anisotropy, they can remain robust without any visible cracking during the lithiation process. Moreover, large volume change due to the insertion of lithium can generate large compressive stress at the reaction front, leading to the considerable lithiation retardation. The mechanistic understanding of the morphological evolution and stress generation sheds light on the design of failure-resistant nanostructured electrodes. Our model also offers a framework for the study of the chemo-mechanical degradation in high-capacity electrode materials.

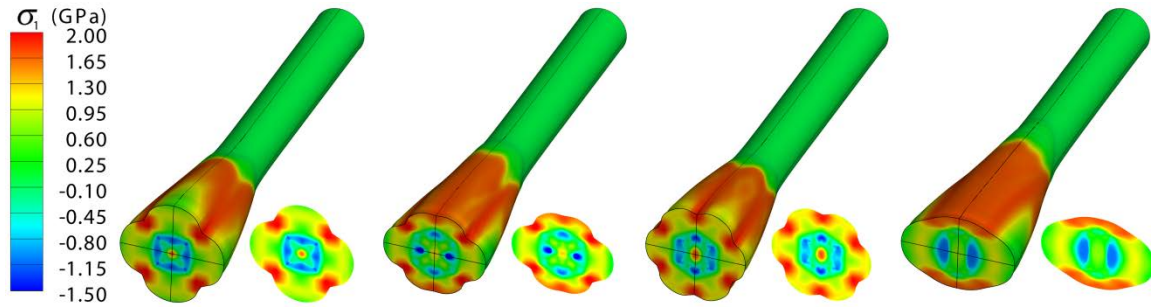


Figure 1: Chemomechanical modeling of the morphological evolutions and stress distributions in crystalline silicon nanowires upon lithiation. From left to right, the axial orientations of the SiNWs are  $\langle 100 \rangle$ ,  $\langle 110 \rangle$ ,  $\langle 111 \rangle$ , and  $\langle 112 \rangle$ . Color contours in the image indicate the maximal principal stress.

## References

- [1] [H. Yang](#), F. Fan, W. Liang, T. Zhu, S. Zhang, "A Chemo-Mechanical Model of Lithiation in Silicon", *J. Mech. Phys. Solids*, 2014, Accepted.
- [2] [H. Yang](#), S. Huang, X. Huang, F. Fan, W. Liang, X. H. Liu, L.-Q. Chen, J. Y. Huang, J. Li, T. Zhu, S. Zhang, "Orientation-Dependent Interfacial Mobility Governs the Anisotropic Swelling in Lithiated Silicon Nanowires", *Nano Lett.*, vol. 12, pp. 1953-1958, 2012.
- [3] W. Liang, [H. Yang](#), F. Fan, Y. Liu, X. H. Liu, J. Y. Huang, T. Zhu, S. Zhang, "Tough Germanium Nanoparticles under Electrochemical Cycling", *ACS Nano*, vol. 7, pp. 3427-3433, 2013.
- [4] S. W. Lee, M. T. McDowell, J. W. Choi, Y. Cui, "Anomalous Shape Changes of Silicon Nanopillars by Electrochemical Lithiation", *Nano Lett.*, vol. 11, pp. 3034-3039, 2011.
- [5] X. H. Liu, J. W. Wang, S. Huang, F. Fan, X. Huang, Y. Liu, S. Krylyuk, J. Yoo, S. A. Dayeh, A. V. Davydov, S. X. Mao, S. T. Picraux, S. Zhang, J. Li, T. Zhu, J. Y. Huang, "In situ atomic-scale imaging of electrochemical lithiation in silicon", *Nat. Nanotechnol.*, vol. 7, pp. 749-756, 2012.

# A FRACTIONAL ORDER MODEL FOR LOCAL ELECTRIC FIELDS IN BIOLOGICAL TISSUES

*M. M. Hasan and C. Drapaca*

Engineering Science and Mechanics Department, Penn State University, PA 16802, USA

In recent years, electro-chemotherapy and gene electro-transfer have emerged as promising cancer therapies that use locally applied electric fields to facilitate the transport of either chemotherapeutic drugs into tumor cells or genes into target cells using the cell membrane electroporation. It is well known that the local electric field in the tissue depends on the applied voltage on the electrodes, the geometry and position of the electrodes, and on the heterogeneity and geometry of the biological tissue [1, 2]. So far, the local electric field distribution in tissues was found by solving the classic Laplace equation. However, tissues and tumors have evolving microstructures which affect the distribution of the applied electric field.

Recent experimental and theoretical results have shown that many processes in physics and engineering sciences are in fact governed more accurately by fractional order differential equations instead of traditional integer-order differential equations. Inspired by these findings, in our exploratory study we propose a fractional calculus based approach to model the electric field distribution in tissues. Our approach is based on the assumption that fractional derivatives can model the heterogeneity and multi-scale nature of dynamic materials such as living biological tissues better due to the presence of integration in the definition of the fractional derivatives. The resulting fractional differential equation of Laplace type is solved analytically. Our preliminary results on the local electric field distribution might help to find electrode configurations that will help designing cancer therapies with optimal outcome.

In this paper, we use a six needle array electrode to find the electric field distribution in tissues. The needle configuration is given in figure 1. We assume that the needles are long, with uniform thickness and fully inserted into the tissues. Therefore, the potential can be considered a two dimensional away from the tips of the needles. Assuming a constant conductivity of the tissue, the potential  $\phi(\mathbf{r})$  in the entire region outside the needle can be obtained by solving the Laplace equation:

$$\nabla^2 \phi(\mathbf{r}) = 0 \quad (1)$$

where  $\mathbf{r} = x\hat{i} + y\hat{j}$  and  $\nabla = \frac{\partial}{\partial r^2}$  is the Laplacian. Using the method of Green's functions the solution of equation (1) is:

$$\phi(\mathbf{r}) = \frac{1}{2\pi} \ln\left(\frac{a}{r}\right) \quad (2)$$

where  $\phi(\mathbf{r})$  vanishes when  $\mathbf{r} = a$ . Using now a fractional order Laplacian operator, equation (1) can be written as:

$$\nabla^{2\alpha} \phi(\vec{r}) = 0 \quad (3)$$

where  $\nabla^{2\alpha} = D_r^{2\alpha}$  is the fractional order Laplacian of Riesz derivatives and order is  $\alpha$  ( $0 < \alpha \leq 1$ ). To determine the solution of equation (3), we need to know the Green function  $G_{2\alpha}(\mathbf{r})$  that satisfies:

$$\nabla^{2\alpha} G_{2\alpha}(\mathbf{r}) = -\delta^2(\mathbf{r}) \quad (4)$$

The solution of equation (4) (and hence equation (3) as well) is [3]:

$$\phi(\mathbf{r}) = \frac{\Gamma(1-\alpha)}{2^{2\alpha}\pi\Gamma(\alpha)} \frac{1}{|r-a|^{(2-2\alpha)}} \quad (5)$$

where  $a$  is the position of the needle and  $\Gamma$  is the gamma function.

We can obtain now the solution for the six needle array electrode by keeping the applied potential  $+V_0$  on needles 3 and 4,  $-V_0$  on needles 5 and 6, and zero potential on needles 1 and 2. Therefore, the total potential is the sum of potential generated by each needle:

$$\phi(\mathbf{r}) = \sum_{n=1}^6 \phi_n(\mathbf{r}) \quad (6)$$

From the analytical results presented here, we can see that when the fractional order  $\alpha$  approaches 1, the solution (6) converges to the classical analytical solution given in [1]. The formulation developed here provides a convenient way of calculating the distribution of the electric field developed by clinically used electroporation technique.

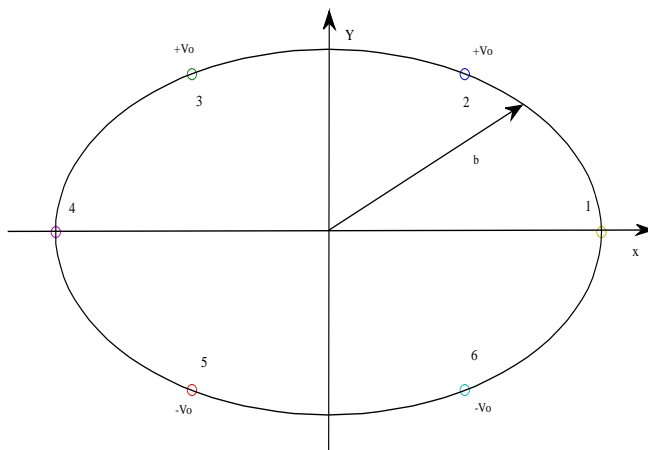


Figure 1: Electrode configuration of an array of six needles on a circle of radius  $b$ .

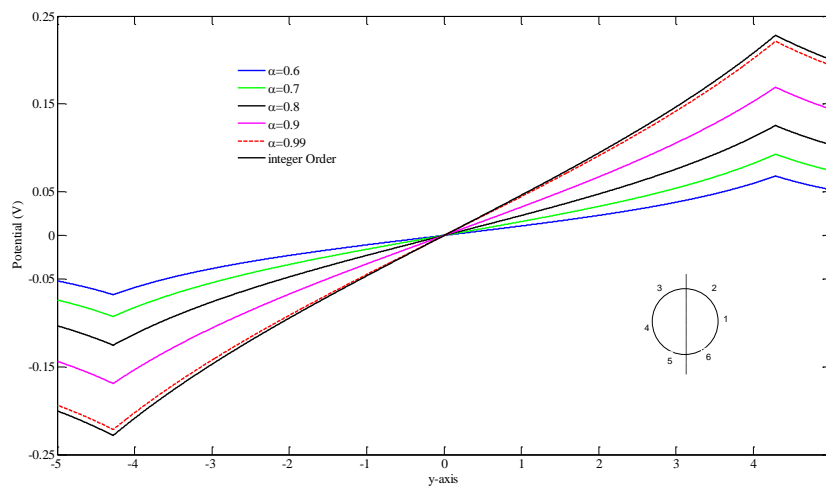


Figure 2: Potential distributions vs. position for different values of the fractional order and in the classic case.

## REFERENCES

- [1] S. B. Dev, D. Dhar, W. Krassowska, "Electric Field of a Six-Needle Array Electrode Used in Drug and DNA Delivery In Vivo: Analytical Versus Numerical Solution", IEEE Transactions on Biomedical Engineering, Vol. 50, No. 11, November 2003
- [2] S. Corovic, M. Pavlin, D. Miklavcic, "Analytical and Numerical Quantification and Comparison of the Local Electric Field in the Tissue for Different Electrode Configurations", BioMedical Engineering OnLine, Vol. 6, No. 1, pp. 37, 2007.
- [3] S. I. Mulish, O. P. Agrawal, "Riesz Fractional Derivatives and Fractional Dimensional Space", Int Theor Phys, Vol. 47, No. 2, pp. 270-275, 2010.

# ACOUSTIC STREAMING AROUND OSCILLATING SHARP EDGES

*Nitesh Nama, Po-Hsun Huang, Tony Jun Huang, Francesco Costanzo*

Department of Engineering Science and Mechanics, The Pennsylvania State University,  
University Park - 16802, PA, USA

Oscillating sharp edges have been employed to achieve rapid and homogeneous mixing in microchannels using acoustic streaming, see fig 1. These mixers utilize acoustically oscillating sharp edges to generate microvortices and perturb the flow field to achieve enhanced mixing. This work extends prior experimental studies to numerically characterize the effect of various parameters on the acoustically induced flow. We present a numerical model using a perturbation approach to study the flow around acoustically-driven, oscillating sharp edges in a microchannel. We model the fluid as compressible and linear viscous using the compressible Navier-Stokes equations. These are intrinsically nonlinear and are characterized by different behaviors over wide ranges of time and length scales. The flow on the large length- and time-scale arises from the acoustic excitation at much smaller time and length scales. Consequently, a direct solution of the compressible Navier-Stokes equation remains computationally challenging even with modern computational tools. The problem is further complicated due to the presence of singularity in the flow field at the sharp edge. To capture the singularity in the flow field, we refine the mesh near the tip of the sharp edge using an adaptive mesh refinement strategy. We employ periodic boundary

conditions to model a periodic cell representative of the full domain, thereby resulting in huge savings in computational costs and time. We investigate the effect of various parameters including the tip angle, oscillation amplitude, and channel dimensions on the flow patterns. The predicted flow profiles are found to reflect the inherent nonlinearity of the acoustic streaming phenomena as the various patterns identified are not linear scalings of one another. The flow field is found to be heavily dependent on the geometrical parameters of the device. The streaming velocity is also observed to show a quadratic dependence on the applied input displacement and a nonlinear increase with the decrease in tip angle. We also show that properties contributing to the overall mixing effectiveness of the device can be in "competition" with each other making the identification of optimal geometric and working configurations nontrivial. For this reason, we believe that our computational effort, in addition to providing better understanding of flow around sharp edges in confined microchannels, is also very useful in design optimization of sharp-edge micro-mixers which have numerous applications in many lab-on-a chip processes like biomedical diagnostics, drug delivery, chemical synthesis, enzyme reactions.

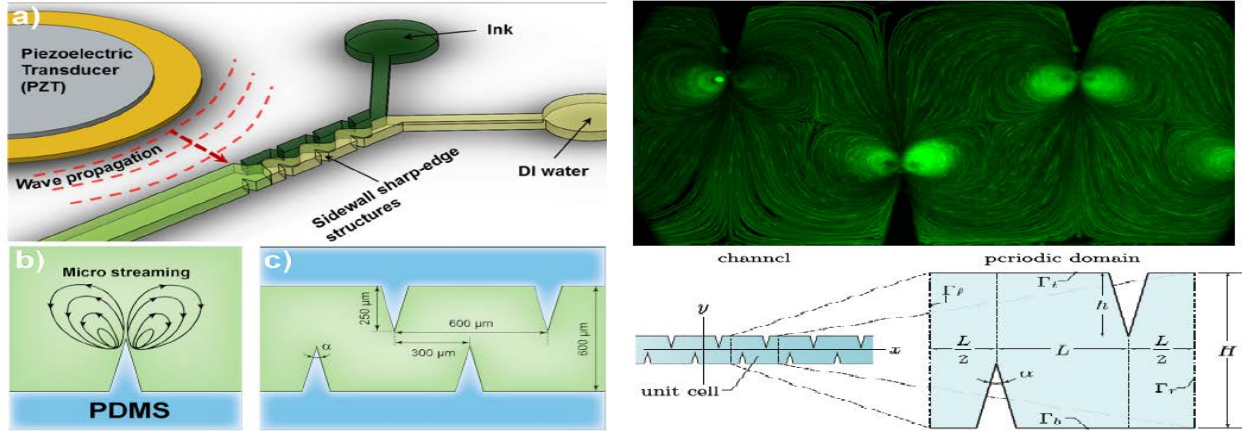


Figure 1: (a) Schematic of the device showing a micro-fluidics channel with sharp-edge structures on its side walls. (b) Typical micro streaming patterns produced in the fluid occupying the channel as a response to piezoelectric excitation. (c) Typical geometric dimensions of the corrugated channel. (d) Experimentally observed trajectories of 1.9 micron diameter fluorescent beads in our acoustically oscillated micro-mixer with sharp edges. (e) A portion of the microfluidics device and an enlarged periodic cell forming the device.

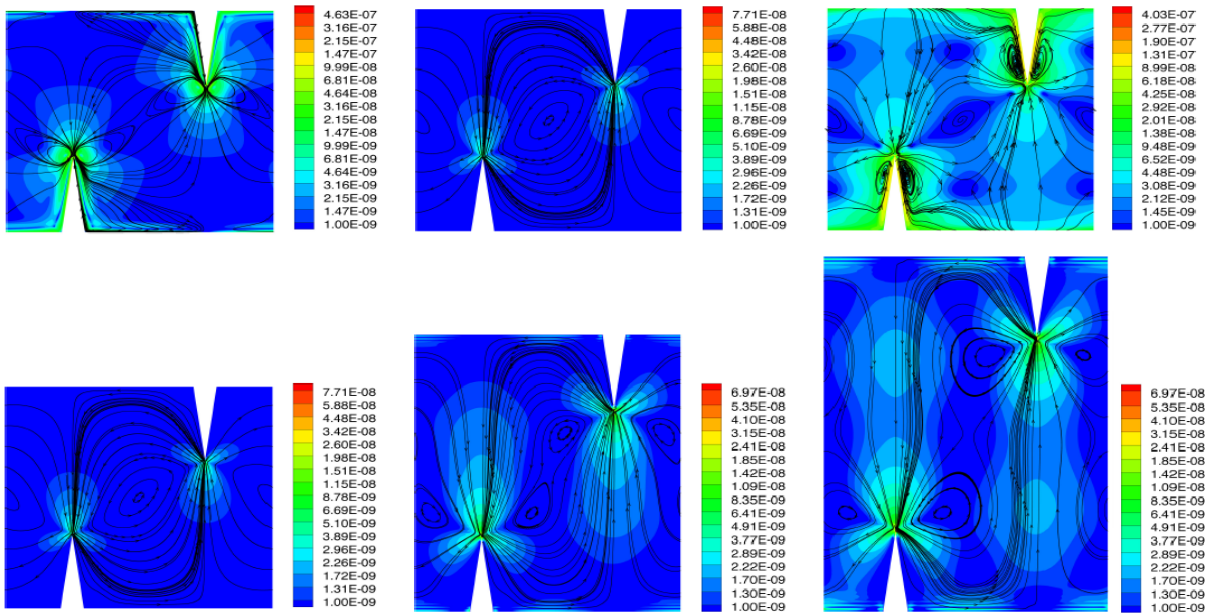


Figure 1: Plot of trajectories of (a) bead velocity (b) fluid velocity (c) mean velocity of mass flow. (d)-(f) Plot of bead trajectories for different channel heights ( $h= 300$  microns,  $400$  microns and  $500$  microns respectively).

## REFERENCES

- [1] H. Bruus, *Lab On a Chip*, 2012, 12, 1014-1021.
- [2] W. Bangerth, R. Hartmann, and G. Kanschat, *deal.II Differential Equations Analysis Library – Technical Reference*, 1998-2006.

# OPTICAL SENSING VIA SURFACE MULTIPLASMONICS

S. E. Swiontek and A. Lakhtakia

Department of Engineering Science and Mechanics, Penn State, PA-16802, USA

Several types of electromagnetic surface waves (ESWs) have been researched both theoretically and experimentally since the early 1900's. These ESWs are guided by the planar interface of two dissimilar materials. The fields of an ESW must satisfy the frequency-domain Maxwell equations in both partnering materials as well as the boundary conditions at the interface. As the material changes about the interface, so do the characteristics of the surface wave [1]. These delicate changes in surface-wave characteristics of the partnering materials makes ESWs suitable for optical detection of hundreds of biological, chemical, and bio-chemical analytes [2].

The surface plasmon-polariton (SPP) wave has dominated research in academic and industrial settings. This surface wave is guided by the interface of a metal and a dielectric material in which both partnering materials are isotropic and homogeneous. SPP waves are most commonly excited using a prism-coupled configuration. Generally, a thin metal film (tens of nanometers) is deposited by a physical vapor deposition (PVD) technique onto the hypotenuse of a 45°-90°-45° prism. That metal then partners air. When a *p*-polarized plane wave is incident onto one side of slanted face at an angle  $\theta$  above the critical angle  $\theta_c$  of the prism, most of the light is reflected toward the other slanted face of the prism. The remainder is absorbed. When the reflected light is plotted against  $\theta$ , a sharp drop in reflection indicates the excitation of an SPP wave [2].

However, since only one solution satisfies the boundary conditions for isotropic and homogeneous metal/dielectric partnering materials, only one SPP-wave mode can be excited. Thus, only *one* analyte can be detected at a given time. It has been theorized that more than one SPP-wave mode—with different spatial profile, attenuation rates, and phase speeds—can be guided by the interface of a metal and a dielectric material, provided that the dielectric material is anisotropic and periodically non-homogeneous in the thickness direction. This can lead to *multiple analyte detection* and/or more robust measurements with high sensitivity.

A chiral sculptured thin film (STF) meets those aforementioned requirements. A chiral STF is periodically non-homogeneous thin film comprising nanohelices oriented along the thickness direction. The chiral STF is grown on planar substrates through PVD techniques in a low-pressure vacuum chamber.

The morphology is acquired by tilting the substrate to an oblique angle  $\chi_v$  with respect to a collimated flux of an evaporated material. When a chosen value of  $\chi_v$  is reached, the substrate then rotates about an axis which passes normally through it. Deposition conditions such as the vapor flux angle  $\chi_v$ , pitch  $2\Omega$ , and number of structural periods of the chiral STF can be engineered to suit the needs of the application [3]. Exciting multiple-SPP-wave modes has long since been demonstrated experimentally by employing a chiral STF when implemented in the TKR configuration.

In proof-of-concept sensing experiments, SF-11 glass with a refractive index  $n = 1.778$  served as substrate on which a 30-nm-thick aluminum thin film followed by a two- or three-period-thick chiral STF composed of lanthanum fluoride of a pitch  $2\Omega = 400$  nm were sequentially deposited via resistive-heating PVD. The substrate was then placed on an SF-11 prism of the same optical density. An index-matching liquid was placed between the substrate with the opposite side of the thin-film stack and the prism. The TKR configuration was then affixed to a custom-built machine that measures changes in reflectance of a *p*-polarized beam where  $\lambda_0 = 635$  nm as a function of angle  $\theta$  [3].

A cross section of the TKR configuration is schematically shown in Fig. 1. When the pores of the chiral STF were occupied by air, three different SPP-wave modes were launched as shown in Fig 2. Platform A is a three-period-thick chiral STF where in Platform B is a four-period-thick chiral STF. When reflection dips coincide for both platforms, i.e. thickness independent, an SPP wave is launched. SPP-wave modes are indicated by '1', '2', and '3'.

When those pores are replaced by DI water ( $n_{H_2O} = 1.33$ ) the number of SPP-wave modes reduced two. The launching of these two modes is indicated by the reflectance dips labeled 1 and 2 on the solid blue line in Fig. 2. When an aqueous solution of sucrose with increasing molarity infiltrated the pores instead of water, both reflectance dips shifted to higher values of  $\theta$  as shown in Fig. 3. The sensor offers dynamic sensitivities of 90 degrees per refractive-index unit (deg/RIU) or higher, which are comparable to state-of-research values. Therefore, surface multiplasmonics can be employed for optical sensing [3].

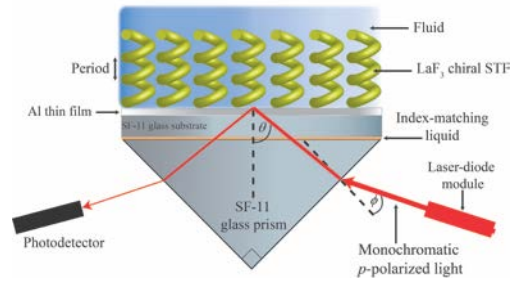


Figure 1: The schematic of the TKR configuration wherein a thin metal film, followed by a chiral STF, is deposited on a substrate. It is then placed on top of one face of a right-angle prism which is of the same optical density of that substrate. An index-matching liquid between the prism and substrate minimizes refractive-index mismatching between those two components. A monochromatic  $p$ -polarized plane wave is incident on one slanted face at angle  $\theta_i$ . The intensity of the beam incident light diminishes with each refracted step the light takes inside the prism, until it exits from one leg of the prism, as shown.

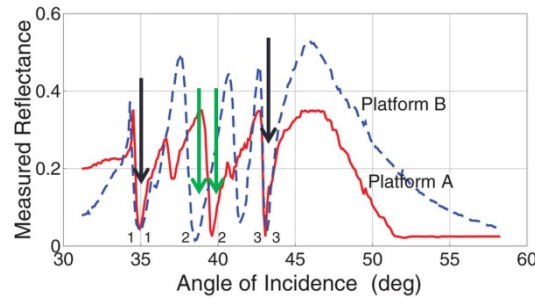


Figure 2: Measured reflectance as a function of angle of incidence  $\theta$  at  $\lambda_o = 635$  nm of a three- and four-period-thick chiral STF implemented in the TKR configuration. Arrows pointing to the three dips in the graph indicate that multiple SPP-wave modes can be launched at a single frequency and interface, thus promising multi-analyte detection.

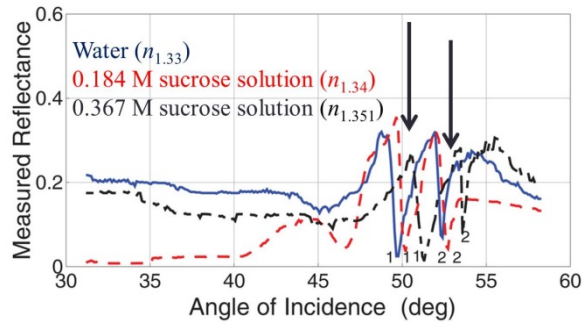


Figure 3: Measured reflectance as a function of angle of incidence  $\theta$  at  $\lambda_o = 635$  nm of a three-period-thick chiral STF implemented in the TKR configuration. Reflectance where water infiltrated the void regions of the chiral STF is shown in blue, 0.184-M solution of sucrose in red dashed, and 0.367-M sucrose solution in black dashed. This graph shows optical sensing of analytes in solution with a multiple-SPP-wave platform. Arrows point to the general locations of the SPP-wave modes.

## REFERENCES

- [1] J. A. Polo Jr., T. G. Mackay, and A. Lakhtakia, *Electromagnetic Surface Waves: A Modern Perspective*, Elsevier, NY, USA, 2013
- [2] I. Abdulhalim, M. Zourob, and A. Lakhtakia, "Surface plasmon resonance for biosensing: a minireview," *Electromagnetics.*, **28**, pp. 214-242, 2008.
- [3] S. E. Swiontek, D. P. Pulsifer, and A. Lakhtakia, "Optical sensing of analytes in aqueous solutions with a multiple surface-plasmon-polariton-wave platform," *Scientific Reports*, **3** 1409, 2013.

# COARSE-GAINED MODELING OF PLASMODIUM FALCIPARUM INFECTED ERYTHROCYTE MEMBRANE: STRUCTURAL MODIFICATIONS LEAD TO LOSS OF DEFORMABILITY

Y. Zhang, C. Huang, M. Golkaram, S. Zhang

Engineering Science and Mechanics Department, Penn State, PA-16802, USA

*Plasmodium falciparum*, the most virulent human malaria parasite, invades human erythrocytes, exports proteins to modify erythrocyte membrane, endows erythrocyte with high stiffness and cytoadherence and then enables erythrocyte to block blood vessels and cause dysfunction of organs[1, 2]. The dramatic loss of erythrocyte deformability plays a critical role in the pathogenesis of *P. falciparum* malaria[3]. Despite progress in experimental studies on erythrocyte remodeling triggered by *P. falciparum* infection, the underlying mechanism of how the structural modifications of erythrocyte membrane lead to the impressive loss of deformability remains elusive. Using a coarse-grained composite erythrocyte membrane model[4, 5], capable in incorporating structural modifications caused by *P. falciparum*, we systematically investigated shear elasticity of the erythrocyte membrane. Our simulation results show that though spectrin network accounts for the shear modulus of healthy erythrocyte, pure alteration of spectrin network would not induce remarkable increase in the shear modulus. It is the knob formation that significantly influences erythrocyte membrane via tightening association between spectrin network and lipid bilayer, strengthening spectrin network and hardening local lipid bilayer. Locally hardened lipid bilayer would not behave like a fluid in healthy erythrocyte but more like a solid to promote the shear modulus. Evolution of knob density and size also plays an important role in enhancing the shear modulus. Shear moduli of *P. falciparum*-infected erythrocyte at different asexual stages yielded from our model are in good agreement with experimental results. Our findings offer insight into the stiffening mechanism of *P. falciparum* infected erythrocyte.

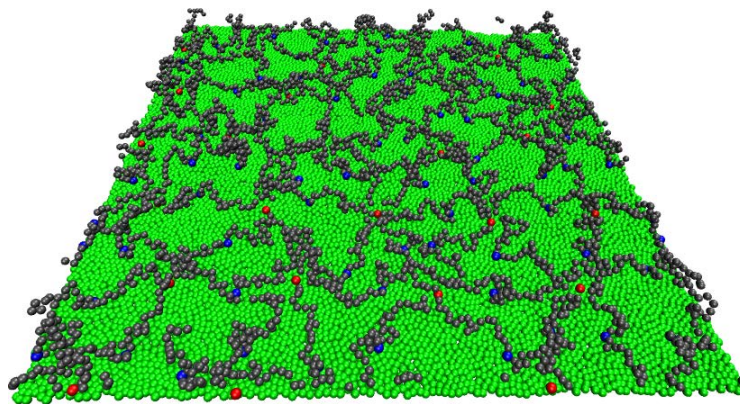


Figure 1. Coarse-grained molecular dynamics model of healthy RBC membrane including lipid bilayer and spectrin network. Green, red, blue and gray particles denote lipid particles, actin oligomers, ankyrins and spectrin beads, respectively.

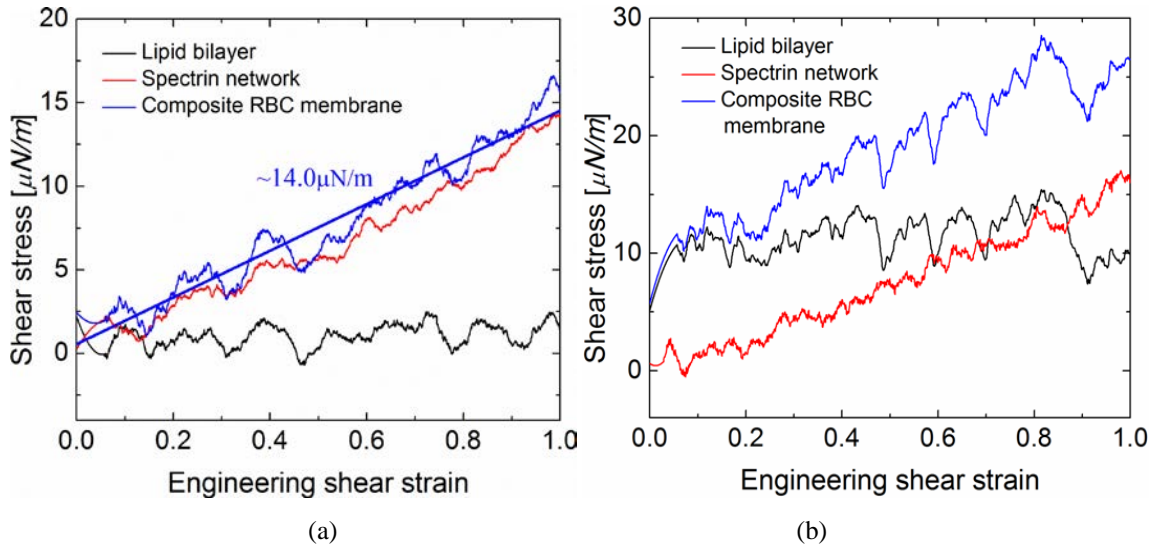


Figure 2. Shear responses of healthy RBC membrane. Shear stress-strain responses of the composite RBC membrane, the lipid bilayer and spectrin network at a low shear rate  $\dot{\gamma} = 5.71 \times 10^{-4} \tau^{-1} s^{-1}$  (a) and at a high shear rate  $\dot{\gamma} = 5.71 \times 10^{-3} \tau^{-1} s^{-1}$  (b).

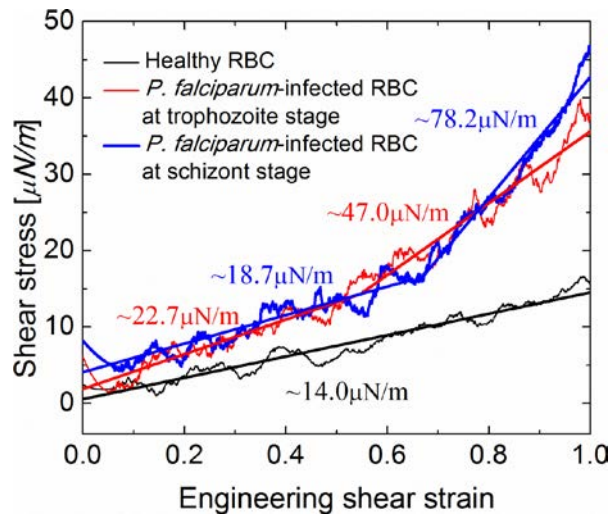


Figure 3. Shear stress-strain responses of healthy RBC membrane and *P. falciparum*-infected RBC membrane at different asexual stages. The strain rate is  $\dot{\gamma} = 5.71 \times 10^{-4} \tau^{-1} s^{-1}$ .

## REFERENCES

- [1]. Maier, A.G., et al., *Malaria parasite proteins that remodel the host erythrocyte*. Nat Rev Micro, 2009. **7**(5): p. 341-354.
- [2]. Waller, K.L., et al., *Interactions of Plasmodium falciparum erythrocyte membrane protein 3 with the red blood cell membrane skeleton*. Biochimica et Biophysica Acta (BBA) - Biomembranes, 2007. **1768**(9): p. 2145-2156.
- [3]. Glenister, F.K., et al., *Contribution of parasite proteins to altered mechanical properties of malaria-infected red blood cells*. 2002. p. 1060-1063.
- [4]. Yuan, H., et al., *One-particle-thick, solvent-free, coarse-grained model for biological and biomimetic fluid membranes*. Physical Review E. **82**(1): p. 011905.
- [5]. Li, J., et al., *Cytoskeletal dynamics of human erythrocyte*, in PNAS. 2007. p. 4937-4942.